

Chapter 4

Test Cases and Results

In this chapter we present the test case scenarios simulated in this work as well as the results of the various simulations performed. First, a description of the scenarios is given to detail the geometry and cross section configurations used. Next, a comparison of deterministic results for the test scenarios is given, with discussion and emphasis placed on the difference in the results between different types of quadrature sets. Then, we present results and analysis of the performance of the quadrature sets' associated Monte Carlo variance reduction parameters in the context of both CADIS and FW-CADIS simulations. Finally, a summary of the results is given to conclude the chapter.

4.1 Test Case Scenarios

4.1.1 Steel Plate in Water

The first test case we describe is an idealized geometry of a steel plate embedded in water; it is modeled after the scenario presented in Reference [1]. A diagram of the problem geometry is shown in Figure 4.1 and a list of material properties used in the problem is given in Table 4.1. In Figure 4.1, the orange region contains the source material, the black region is composed of steel, the blue regions indicate water, and the white region is composed of air.

The problem measurements are $53 \times 50 \times 140$ cm. The scenario is uniform in the y -direction and materials vary mainly in the z -direction. The source region extends from 0 to 15 cm, the steel shield extends between 15 and 30 cm, the water and steel plate extend from 30 to 130 cm, and the air extends from 130 to 140 cm. The steel plate is 3 cm wide and is centered at $x = 26.5$ cm. Vacuum boundary conditions were used at the problem boundaries.

A non-uniform Cartesian mesh was used for the spatial discretization in the deterministic calculations. In the x -direction, voxel width is 5 cm between $x = 0$ cm and $x = 25$ cm, 0.5 cm between $x = 25$ cm and $x = 28$ cm, and 5 cm between $x = 28$ cm and $x = 53$ cm. A uniform spacing of voxel width 1 cm was used in the y -direction. In the z -direction, the

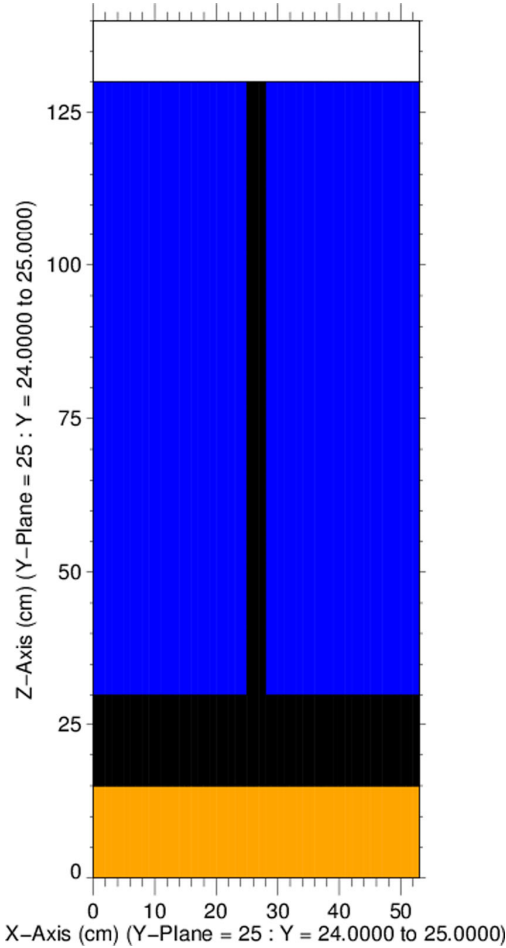


Figure 4.1: Steel plate in water geometry ($x - z$ slice through $y = 25$ cm) [1].

spatial cell width is 3 cm between $z = 0$ cm and $z = 30$ cm and 2 cm between $z = 30$ cm and $z = 140$ cm.

The composition of the neutron source block is a homogenization of water, zirconium, and uranium and was calculated based on the geometry and composition of the Rowlands UO₂ pin cell benchmark specification [2]. The source is a U-235 fission spectrum that is uniformly distributed throughout the homogenized material. The compositions of air, carbon steel, and water were taken from the Compendium of Material Composition Data for Radiation Transport Modeling [3]. For this scenario, we are interested in the forward flux solutions at the end of the steel plate.

Table 4.1: Materials and compositions in the steel plate in water scenario.

Material	Isotopes (Atomic %)	
Source	U-235	(0.000247)
	U-238	(0.009287)
	Zr-nat.	(0.004009)
	H-1	(0.037394)
	O-16	(0.034927)
Air	N-14	(0.784431)
	O-16	(0.210748)
	Ar-nat.	(0.004671)
	C-nat.	(0.000150)
Carbon Steel	C-nat.	(0.022831)
	Fe-nat.	(0.977169)
Water	H-1	(2)
	O-16	(1)

4.1.2 Dog-Legged Void Neutron (DLVN)

The next problem modeled is the dog-legged void neutron (DLVN) experimental benchmark, which was designed to measure neutron streaming in iron with air voids. The model used in the following calculations was constructed from References [4, 5, 6]. The two materials used in the problem are elemental iron and polyethylene. The polyethylene composition used was C₂H₄. This is listed as “polyethylene, non-borated” and is material 248 in Reference [3].

The problem measurements are 40 × 54 × 48 inches. A uniform spatial mesh was imposed over the entire problem, with voxels measuring 1 inch per side. The neutron source in this problem is a Cf-252 point source located at the center of the x - and y -directions and at $z = 9$ inches. For reasons noted in Section 3.4.3, this point source was approximated as a small volumetric source in the tests in this work. We are interested in the forward flux solutions at the various detector locations shown in Figure 4.2.

The experimental configuration is symmetric about the $y - z$ plane at $x = 0$ and so is usually simulated with a reflecting boundary at $x = 0$ and vacuum boundaries on all other sides of the configuration. For the tests in this work, the use of reflecting boundary conditions was not available (see Section 3.4.1), so the model used was constructed to represent the entire experimental geometry configuration. Vacuum boundary conditions were applied to the outside of the entire problem.

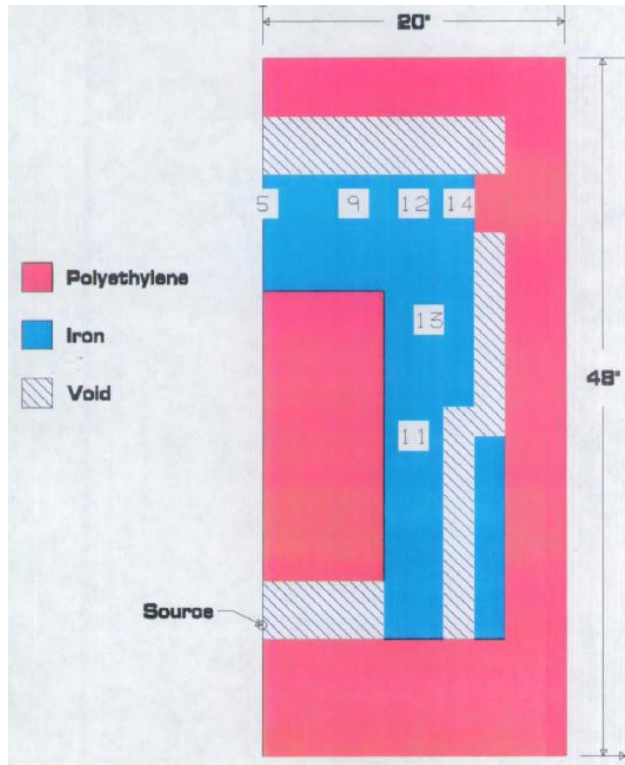


Figure 4.2: Centerline cutaway of DLVN setup [4].

4.1.3 Ispra Sodium Benchmark

The Ispra sodium benchmark experiment was constructed as part of experiments to study neutron deep penetration in homogeneous materials commonly used in advanced nuclear reactors. It is included in the Shielding Integral Benchmark Archive and Database (SINBAD) data library [7]. We will give a brief overview of the material and geometry configuration here and refer the reader to Reference [7] for a complete description of the experiment.

The neutron source consists of fission neutrons originating from an enriched U disc that was subjected to a neutron flux leaving the thermal column of a TRIGA MARK II reactor. An irradiation tunnel assembly composed of steel containers filled with Na was constructed in front of the neutron source converter. The total length of the irradiation tunnel was 400 cm. A diagram of the experimental geometry is shown in Figure 4.3; we are interested in the forward flux solutions in the detector array located along the midline of the assembly.

In the simulation of this benchmark configuration, the boundaries are -300 cm and 500 cm in the x -direction and -400 and 400 cm in both the y - and z -directions. The spatial mesh in this problem is uniform in the y - and z -directions with a voxel width of 5 cm per side in these dimensions. The x -direction mesh was created such that voxels are 10 cm wide between $x = -300$ and -100 cm, 5 cm wide between $x = -100$ and 400 cm, and 10 cm wide between $x = 400$ and 500 cm. The problem has vacuum boundary conditions.

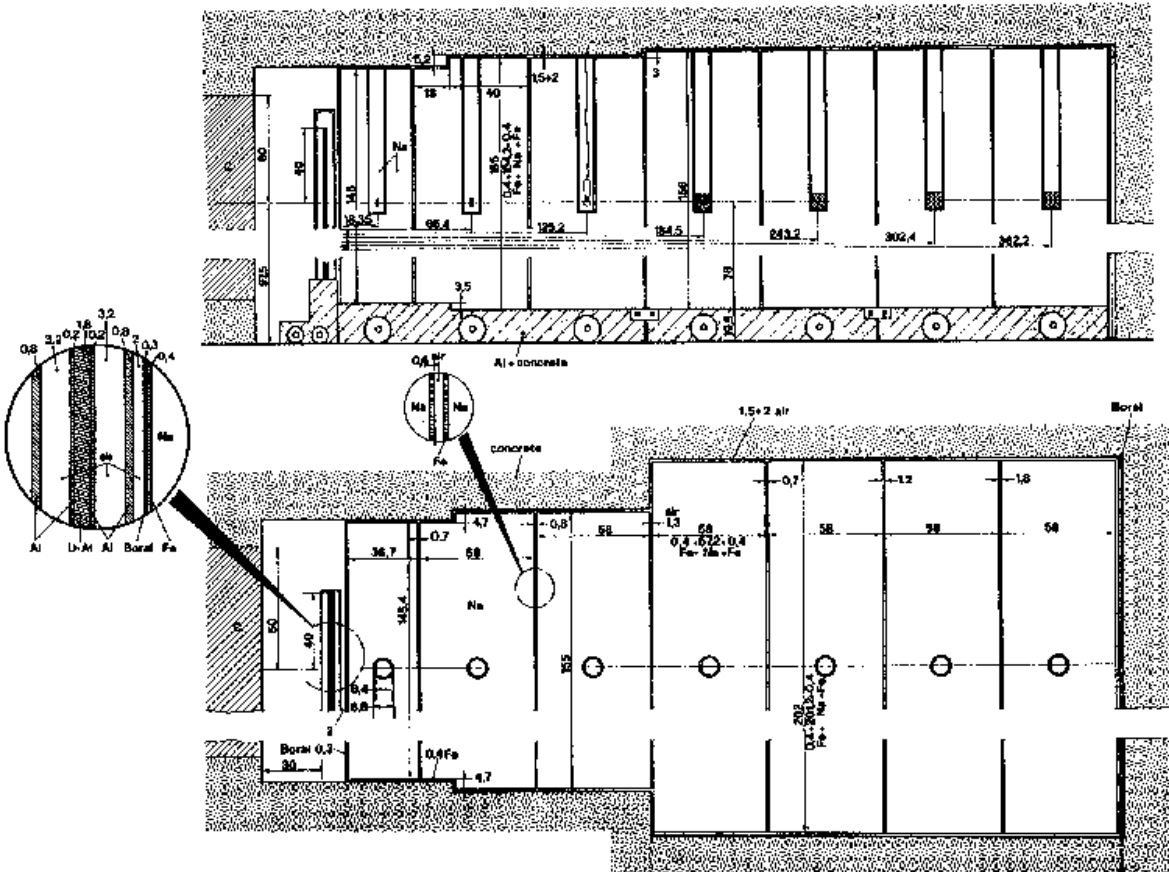


Fig. 2: **Vertical and horizontal cross section of sodium assembly at Euracos II facility**

Figure 4.3: Cross sectional views of the sodium benchmark assembly.

4.1.4 Simplified Portal Monitor

The final problem described here is a simplified portal monitor scenario. Portal monitors are large detector panels used to screen cargo for illicit radioactive materials. The problem models a cargo container holding a Ba-133 photon point source and large blocks of homogenized iron and polyethylene. The geometry and material configuration used in this test is the same as the example problem listed in Section 7.2 of the ADVANTG technical report [8]; slight modifications were made to the given MCNP input deck such that the problem could be studied with both CADIS and FW-CADIS calculations. Diagrams of the simplified portal monitor problem are shown in Figure 4.4.

In Figure 4.4, the different colors represent different materials. The NaI detectors are red and the gray material is concrete. The two types of material blocks are iron, shown in green, and polyethylene, shown in white. The steel cargo container surrounds the particle source

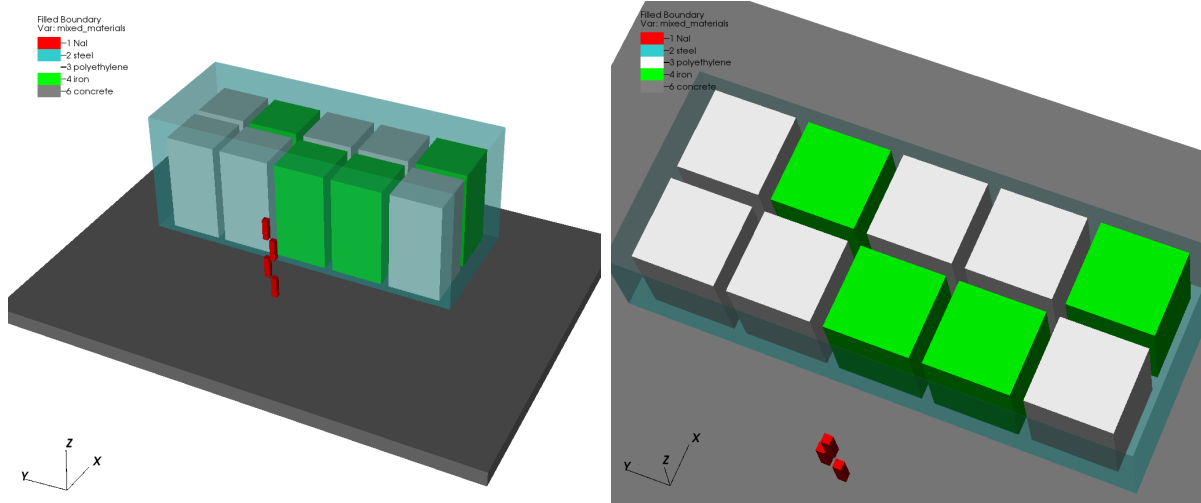


Figure 4.4: Top and side views of simplified portal problem [8].

and material blocks and is a semitransparent blue. Here we are interested in the forward flux solutions at the four detector locations.

A non-uniform Cartesian mesh that captures all of the problem's material boundaries was constructed for this simulation. The voxels are nominally 10 cm thick within the cargo container. Additional mesh planes parallel to the x -axis were added to the gaps between the homogenized iron and polyethylene blocks [8]. Vacuum boundary conditions are present at all problem edges.

4.1.5 Calculation Parameters

4.1.5.1 Deterministic

All of the deterministic calculations used 32 processes on a 2.8GHz AMD OpteronTM 6320 Processor [9], two for each logical CPU unit. With this in mind, all deterministic calculations were set to use the same Denovo computational block structure of 8 blocks in the x -dimension, 4 blocks in the y -dimension, and 1 block in the z -dimension; thus the total number of computational blocks equals the number of processes. Denovo uses the Koch-Baker-Alcouffe (KBA) parallel sweep algorithm for high parallel efficiency in calculating transport sweeps [10]; the aforementioned block structure was chosen to achieve the same parallel decomposition among all test case deterministic simulations.

All but one of the test cases use the same coarse energy group structure specified in the “27n19g” library; the groups in this library are listed in Table A-1 of Appendix A of the ADVANTG technical report [8]. The exception to this is the simplified portal problem. The highest energy emission line of Ba-133 is 383.8 keV, so weight window bounds above this energy would not be used in the Monte Carlo simulation. Thus, the highest energy group of the deterministic calculations was set to group number 41, which has an upper energy of

400 keV [8]. Because energy discretization is treated the same way between the traditional discrete ordinates formulation and the LDO equations, it was assumed that energy group structure would not greatly impact the comparative results.

The step characteristics (SC) spatial discretization was used in all of the deterministic calculations based on the recommendation listed in Section 9.1.3 of the Exnihilo user manual [11]. In the DLVN and portal monitor scenarios, the point sources are approximated as small spherical volumetric sources (see Section 3.4.3 for detail).

Except for the Galerkin quadratures, all runs used a P_5 scattering expansion. At the time of this writing, Galerkin quadrature sets are implemented in the Exnihilo framework with the restriction that the P_N order be one greater than the S_N order. That is, for the Galerkin quadrature set of S_N order 2, the corresponding P_N order is set equal to 3, and for the Galerkin quadrature set of S_N order 4, the P_N order is 5.

4.1.5.2 Monte Carlo

The Monte Carlo calculations in this work were run on one Dell PowerEdge C6220 server blade node with two Intel Xeon 10-core Ivy Bridge processors (a total of 20 cores) [12]. All calculations were specified to use 21 MPI tasks; MCNP reserves one “master” process for communication and transports particles with the remaining available tasks [13]. So, for the purpose of parallel efficiency, one transport process per hardware core was used here.

All of the Monte Carlo calculations were run with a fixed number of particle histories to simulate. For the steel plate in water, Ispra sodium benchmark, and simplified portal monitor cases, all calculations used 1×10^9 particle histories in both the CADIS and FW-CADIS contexts. The DLVN experimental benchmark case was simulated with 1×10^{10} neutron histories as it was modeled after calculations in Reference [4]. All Monte Carlo tally results and following calculations are reported with the one standard deviation confidence interval $\bar{x}(1 \pm R)$ where the relative error $R \equiv S_{\bar{x}}/\bar{x}$ [13].

4.2 Deterministic Forward Flux Calculations

Before investigating deterministic flux solutions resultant from solving the LDO equations as input for Monte Carlo variance parameter generation, it behooves us to compare the LDO deterministic results against those of standard quadrature set types. We start here by presenting results and analysis for forward scalar flux solutions using different quadrature types for the four test cases. We assume extensibility of these results to adjoint scalar flux solutions since the changes to the Exnihilo code suite made in this work did not impact the transport solvers in the Denovo package.

For all of the quadrature set types and sizes discussed above, a forward simulation of each test case was run via the Exnihilo framework. The following results show a representative quadrature set chosen for each type. With the exception of the Galerkin quadrature set featured, the angular refinement of the representative quadrature sets was chosen such that

the quadrature sets have approximately the same total number of angles. The QR quadrature set is of order 4 and has 128 angles, the LDFE set is order 1 with 128 angles, and the LDO set is of order 11 with 144 angles. The Galerkin quadrature set chosen as the representative example here is of order 4 and has 24 angles. This set was chosen because its corresponding P_N order is 5 and so the scattering data used matches that of the other quadrature types.

Because more results were generated than are presented here, a fuller set of figures is hosted at <http://dx.doi.org/10.6084/m9.figshare.6063053>.

4.2.1 Quadrature Sets

In these preliminary deterministic calculations, forward solutions for the test cases were generated using quadruple range (QR), Galerkin, linear-discontinuous finite element (LDFE), and LDO quadrature sets. All test cases were run with the same quadrature sets; increasing sizes of quadrature sets were used to ascertain the angular mesh refinement necessary for a given quadrature type to converge to a solution.

QR quadrature sets were chosen to generate the reference results against which the LDO results are compared. QR was selected because they are commonly used in hybrid methods for Monte Carlo variance reduction parameter generation and therefore provide a relevant baseline. The Exnihilo framework allows the user to select the number of polar and azimuthal angles in each octant when using a QR quadrature set; for these studies, the number of polar and azimuthal angles per octant were each set to the same value, with the values ranging from one per octant (for a total of eight angles) to nine per octant (for a total of 648 angles).

LDFE and Galerkin quadrature sets were also chosen because of their interesting mathematical properties. Compared to QR quadrature sets, LDFE quadrature sets have been shown to exhibit more accurate solutions for the scalar flux in both simple and more complex geometry and material configurations [14]; they approximate the angular flux using direction cosines and are determined by requiring that the integration of the related interpolation basis functions is equal to the surface area of a unit sphere. For LDFE quadrature sets, if N is the order of the quadrature, there are $4^{(N+1)}$ angles per octant [11]. In this work, the LDFE quadrature orders used were one (128 total angles) and two (8192 total angles).

Galerkin quadrature sets offer several advantages relative to the standard S_N method for problems with highly anisotropic scattering [15]. Similar to the LDO equations, the “hybrid collocation-Galerkin- S_N ” method developed by Morel has the same algebraic structure as the traditional discrete ordinates equations but employs a nonstandard scattering treatment. For reasons discussed below in Section 4.1.5.1, the Galerkin quadrature orders used were 2 and 4. For an S_N order N , a given Galerkin quadrature set (as implemented in Exnihilo) has a total of $N(N + 2)$ angles; the Galerkin quadrature sets used in this work have 8 and 24 total angles, respectively.

The degrees and sizes of the LDO quadrature sets used are listed in Table 4.2.

Table 4.2: Properties of LDO quadrature sets used in preliminary scaling studies.

Quadrature Order (N)	Number of Points
3	16
5	36
8	81
9	100
11	144
12	169
13	196
14	225

4.2.2 Steel Plate in Water

Figure 4.5 shows a representative forward scalar flux slice plot for each quadrature type. Each of the flux slices is at the midplane of the y -dimension such that $y = 25$ cm. The geometry/material borders are outlined on each plot as well. All plots show the same expected result – the scalar flux is highest in the source region and drops off by orders of magnitude along the z -axis.

To more thoroughly evaluate the LDO quadrature set in this test case, we will look more closely at the differences between the representative LDO flux and the three other quadrature types. Figure 4.6 shows three plots of relative flux differences; each plot compares the representative LDO quadrature set against one of the standard quadrature set types. The relative flux difference is calculated as

$$\phi_{\text{diff}} = \frac{|\phi_{\text{LDO}} - \phi_{\text{ref}}|}{\phi_{\text{ref}}} \quad (4.1)$$

where ϕ_{ref} is the scalar flux calculated using the standard quadrature set and is taken to be the reference value. For all three of the standard quadrature sets, the area of greatest agreement with the LDO scalar flux is towards the bottom of the problem geometry, with discrepancies growing along the z -axis. The greatest difference can be seen between the LDO and Galerkin quadrature sets, while the LDO and QR quadrature sets agree best. The area of greatest discrepancy between the QR and LDO flux solutions is in the region of air just beyond the steel beam. We will look more in depth as to why this is in Section 4.3.1 and briefly note here that this particular deviation is most likely due to issues in processing iron cross section data inherent to deterministic calculations.

Table 4.3 lists the minimum, maximum, and average differences between various quadrature types for the flux slices plotted in Figure 4.6. We compare the representative LDO flux solution to the solutions from the three standard representative quadrature types and also compare the Galerkin and LDDE results against the QR result. On average, the LDO forward flux solution matches the QR flux solution more closely than it matches either the

Galerkin or LDFE flux solutions. Additionally, the LDO flux solution matches the QR flux solution more closely than do either of the Galerkin and LDFE flux solutions.

Table 4.3: Steel plate forward scalar flux extremal and average relative differences.

Comparison	Min. Diff.	Max. Diff.	Avg. Diff.
LDO/QR	6×10^{-6}	1.09×10^{-1}	2.21×10^{-2}
LDO/Galerkin	2×10^{-5}	4.51×10^0	9.30×10^{-1}
LDO/LDFE	5×10^{-7}	2.79×10^{-1}	9.42×10^{-2}
Galerkin/QR	3×10^{-5}	8.24×10^{-1}	2.90×10^{-1}
LDFE/QR	2×10^{-7}	2.48×10^{-1}	9.63×10^{-2}

Looking at Figures 4.5 and 4.6 we note that the forward scalar flux solutions from the LDO equations capture the same physical trends as the standard quadrature type solutions and also that the LDO flux solution most closely matches that using the QR quadrature set. Additionally, Table 4.3 shows an average difference of 2.2% between the plotted flux solutions from the representative LDO and QR quadrature sets, which is the lowest average difference seen in the comparisons here. As QR quadratures are commonly used for Monte Carlo variance reduction parameter generation, the relative agreement of the LDO scalar flux with the QR scalar flux motivates the exploration of the use of LDO scalar flux solutions for Monte Carlo variance reduction parameter generation.

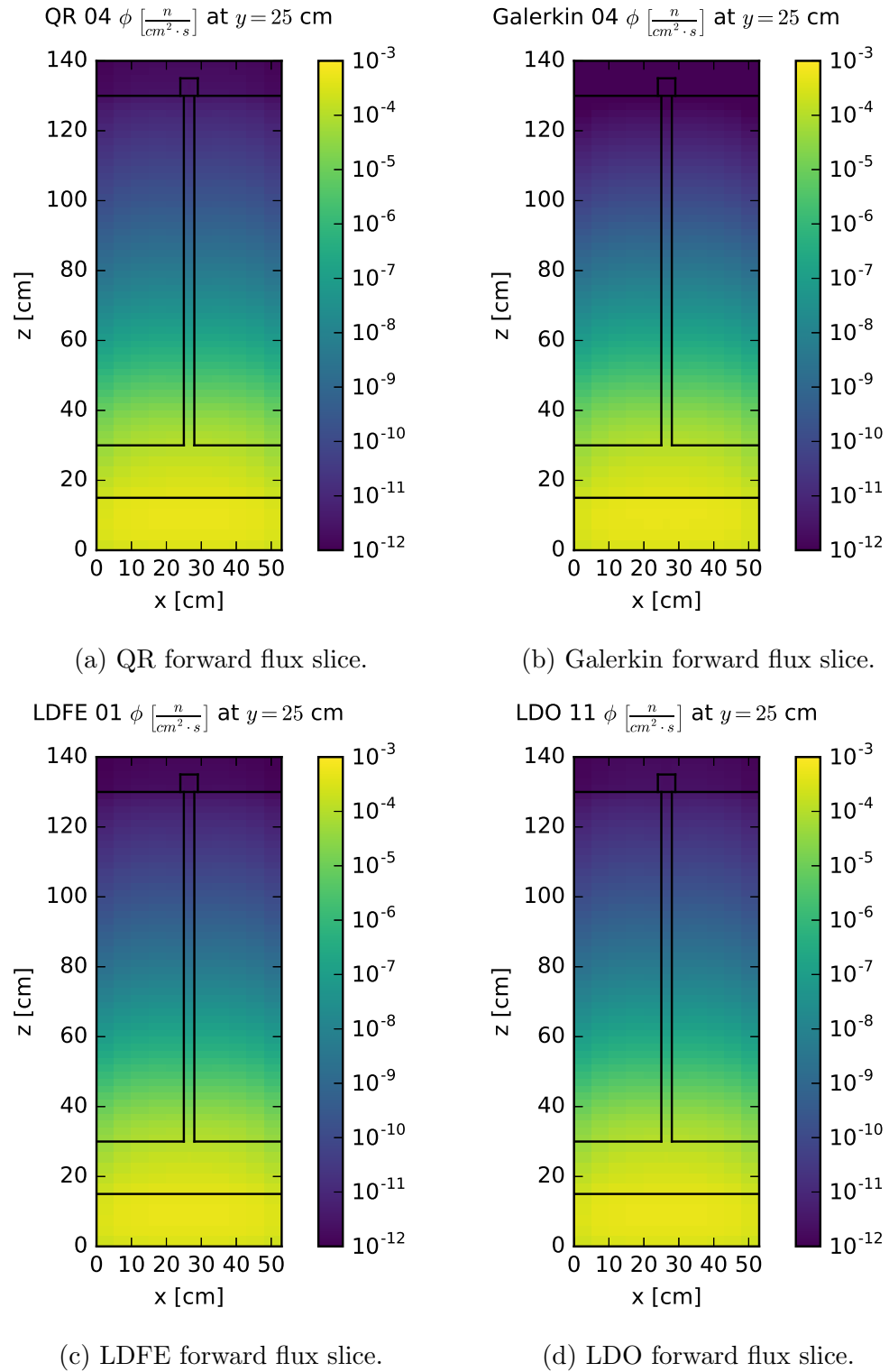


Figure 4.5: Steel plate forward scalar flux slices.

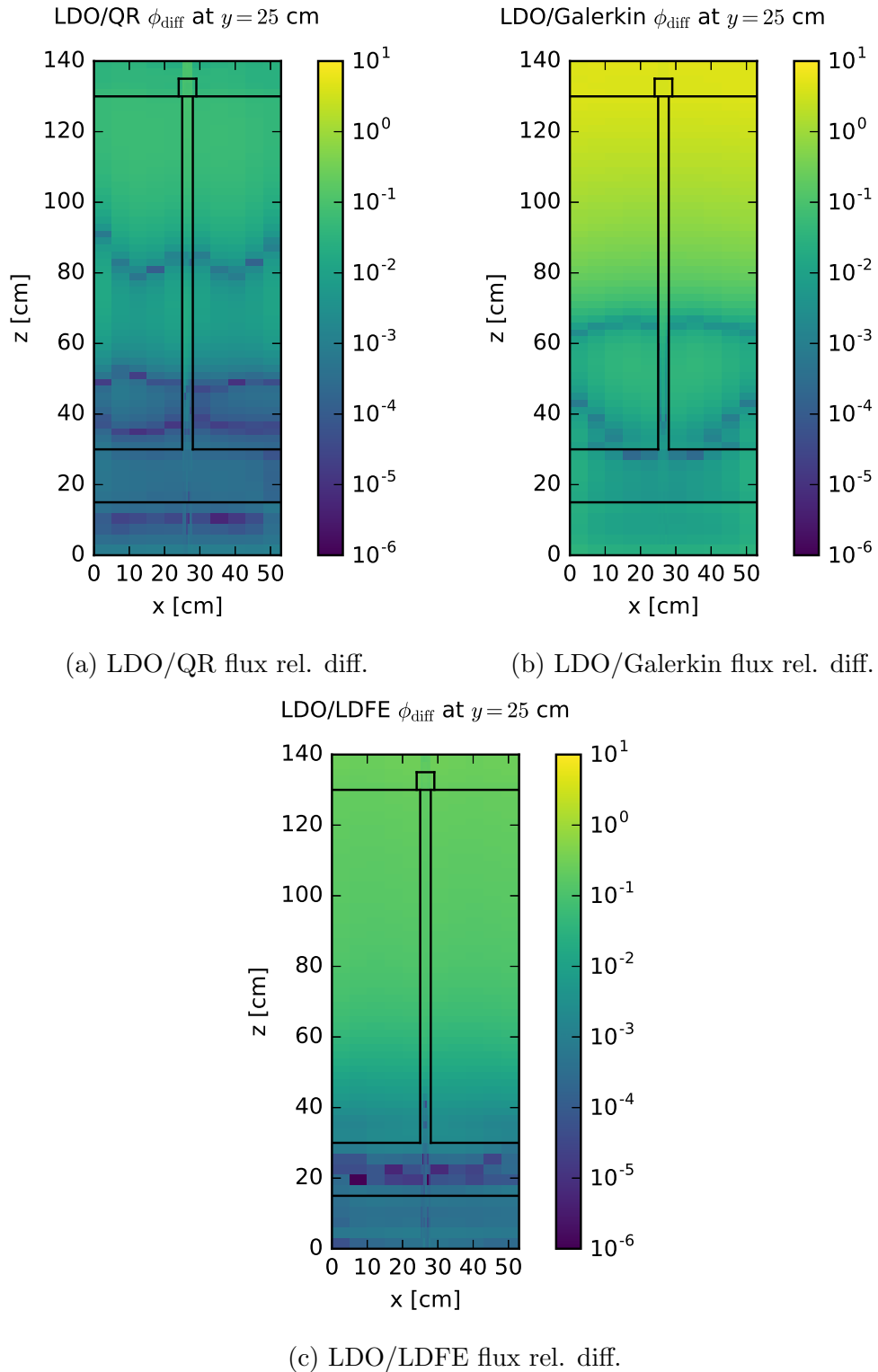


Figure 4.6: Steel plate forward scalar flux relative difference slices.

4.2.3 DLVN

For the DLVN test case, we present flux slice plots for the same representative quadrature sets listed in Section 4.2.2. Although the entire DLVN experimental geometry was simulated, here we plot only half of the configuration; this is the typical view of the benchmark seen in the literature.

Figure 4.7 shows the forward scalar flux for each of the representative quadrature sets at the midplane of $y = 27$ inches (68.58 cm). Each of the plots has outlines of the material boundaries with the detector locations delineated as well. As expected, the flux is highest at the neutron source and decreases as particles move through the experimental configuration. With this, we again look at the differences between the representative LDO flux and the three other quadrature types.

As with the previous test case, the flux differences are calculated with Equation 4.1. In the DLVN scenario, the differences stem from the source location. This is not surprising; the particle source here is approximately a point source and so these differences are appearing in the form of ray effects, where the discrete angles in the LDO quadrature set do not overlap with the angles in a given standard quadrature set. Similar to the steel plate in water test case, the LDO scalar flux best matches the QR scalar flux and the largest differences are seen between the LDO and Galerkin scalar flux plots. Looking at Figure 4.8b, the areas of greatest discrepancy appear as ray effects; the relative coarseness of the representative Galerkin quadrature set angular mesh is likely the cause of this. This is visibly pronounced in the DLVN case because of the geometrically small particle source; it is also likely the source of the LDO/Galerkin discrepancy seen above for the steel plate embedded in water, but ray effects are lessened in that scenario by the larger volumetric source.

Lastly, it is instructive to compare the results of the forward deterministic scalar flux solutions with the experimentally measured flux values at the detector locations. Table 4.4 lists the experimentally measured [6] and deterministically calculated scalar flux values at the detector locations noted in Figure 4.2. Table 4.5 lists the percent differences between the deterministically calculated flux values and experimentally determined flux values with the lowest difference for each detector location emphasized.

Table 4.4: DLVN benchmark experimental and simulated scalar flux values [$\text{n}/\text{cm}^2/\text{s}$].

	Det. #5	Det. #9	Det. #11	Det. #12	Det. #13	Det. #14
Exp. Flux	6.97×10^{-8}	1.57×10^{-7}	8.81×10^{-6}	2.60×10^{-7}	1.42×10^{-6}	2.74×10^{-7}
QR	4.98×10^{-8}	1.68×10^{-7}	8.65×10^{-5}	4.92×10^{-7}	2.71×10^{-6}	1.45×10^{-6}
Galerkin	3.24×10^{-8}	1.47×10^{-7}	8.19×10^{-5}	4.43×10^{-7}	2.95×10^{-6}	9.55×10^{-7}
LDFE	5.12×10^{-8}	1.76×10^{-7}	9.17×10^{-5}	5.14×10^{-7}	2.93×10^{-6}	1.47×10^{-6}
LDO	4.56×10^{-8}	1.39×10^{-7}	7.88×10^{-5}	4.28×10^{-7}	2.37×10^{-6}	1.28×10^{-6}

Looking at Table 4.5 we see that all of the calculated values fall outside of the experimental uncertainty of five percent [6]. The results from the LDO quadrature set most closely

Table 4.5: Percent differences between DLVN experimental and simulated scalar flux values.

	Det. #5	Det. #9	Det. #11	Det. #12	Det. #13	Det. #14
QR	25.58	6.89	881.94	89.09	90.63	428.81
Galerkin	53.48	6.37	829.72	70.56	107.7	248.42
LDFE	26.61	12.3	940.41	97.75	106.4	435.01
LDO	34.61	11.2	794.75	64.46	66.77	368.24

match the experimental results for half of the detector locations. This begs the question of how the LDO equations would perform in the context of the FW-CADIS method for the DLVN problem since the adjoint source can be set to multiple detector locations. Table 4.6 lists the extreme and average values of the forward flux relative difference slices shown in Figure 4.8 with Galerkin/QR and LDFE/QR comparisons included for reference. We see that, on average, the LDO forward flux solution matches the QR forward flux solution better than it matches those of the other quadrature types. However, in this case, the LDFE flux solution matches the QR flux solution on average better than any other quadrature type, including the LDO flux solution (5% difference versus 8.4% difference).

Table 4.6: DLVN benchmark forward scalar flux extremal and average relative differences.

Comparison	Min. Diff.	Max. Diff.	Avg. Diff.
LDO/QR	2×10^{-4}	8.40×10^{-1}	8.44×10^{-2}
LDO/Galerkin	1×10^{-6}	2.14×10^0	2.42×10^{-1}
LDO/LDFE	3×10^{-5}	8.71×10^{-1}	1.17×10^{-1}
Galerkin/QR	3×10^{-4}	6.37×10^{-1}	1.92×10^{-1}
LDFE/QR	3×10^{-5}	2.67×10^{-1}	5.05×10^{-2}

Noting the potential performance of the LDO quadrature sets in the FW-CADIS context and having observed fairly good agreement between the LDO forward flux result and the QR forward flux result, we will further pursue solutions of the LDO equations as input for Monte Carlo variance reduction parameter generation for the DLVN problem.

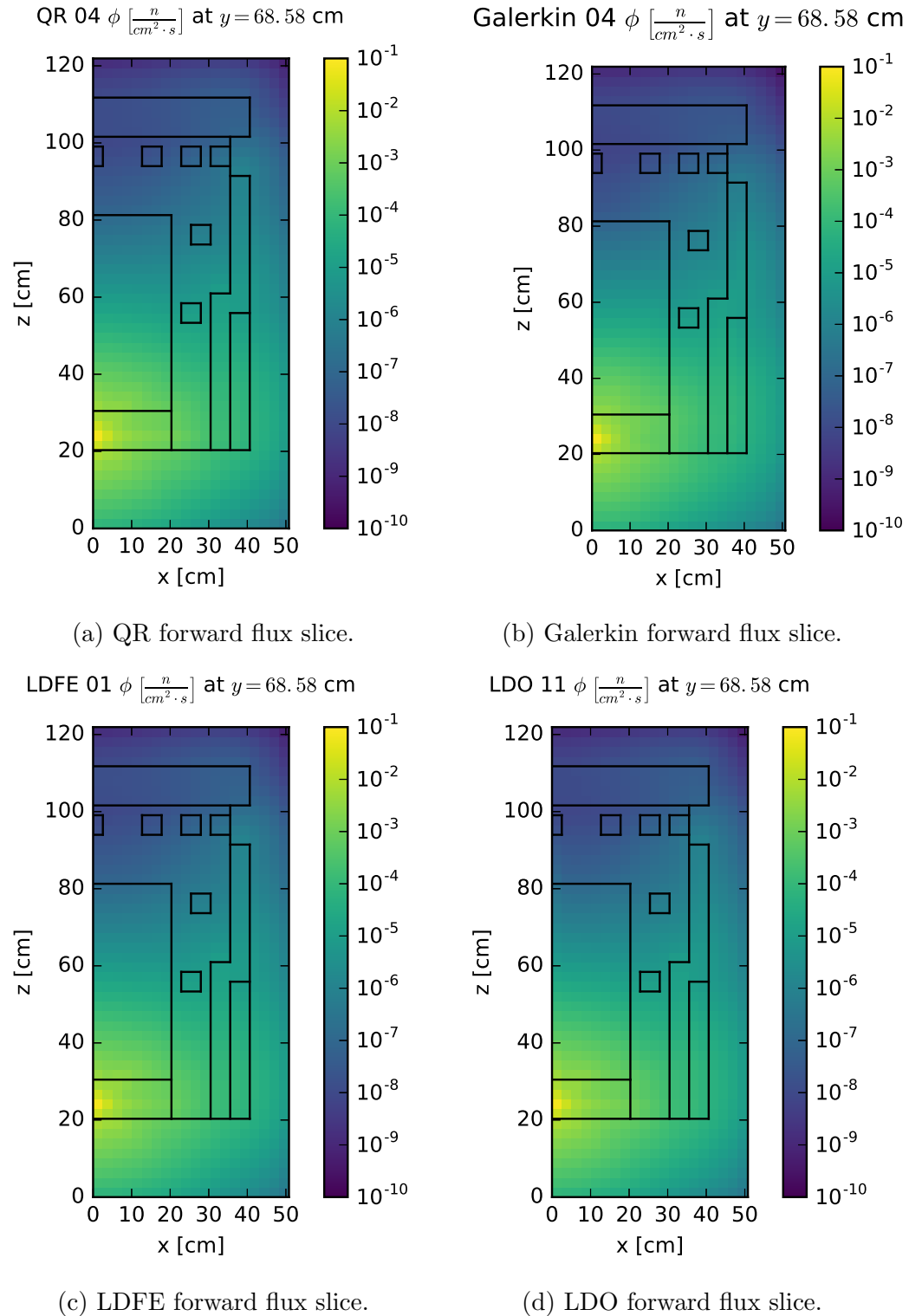


Figure 4.7: DLVN benchmark forward scalar flux slices.

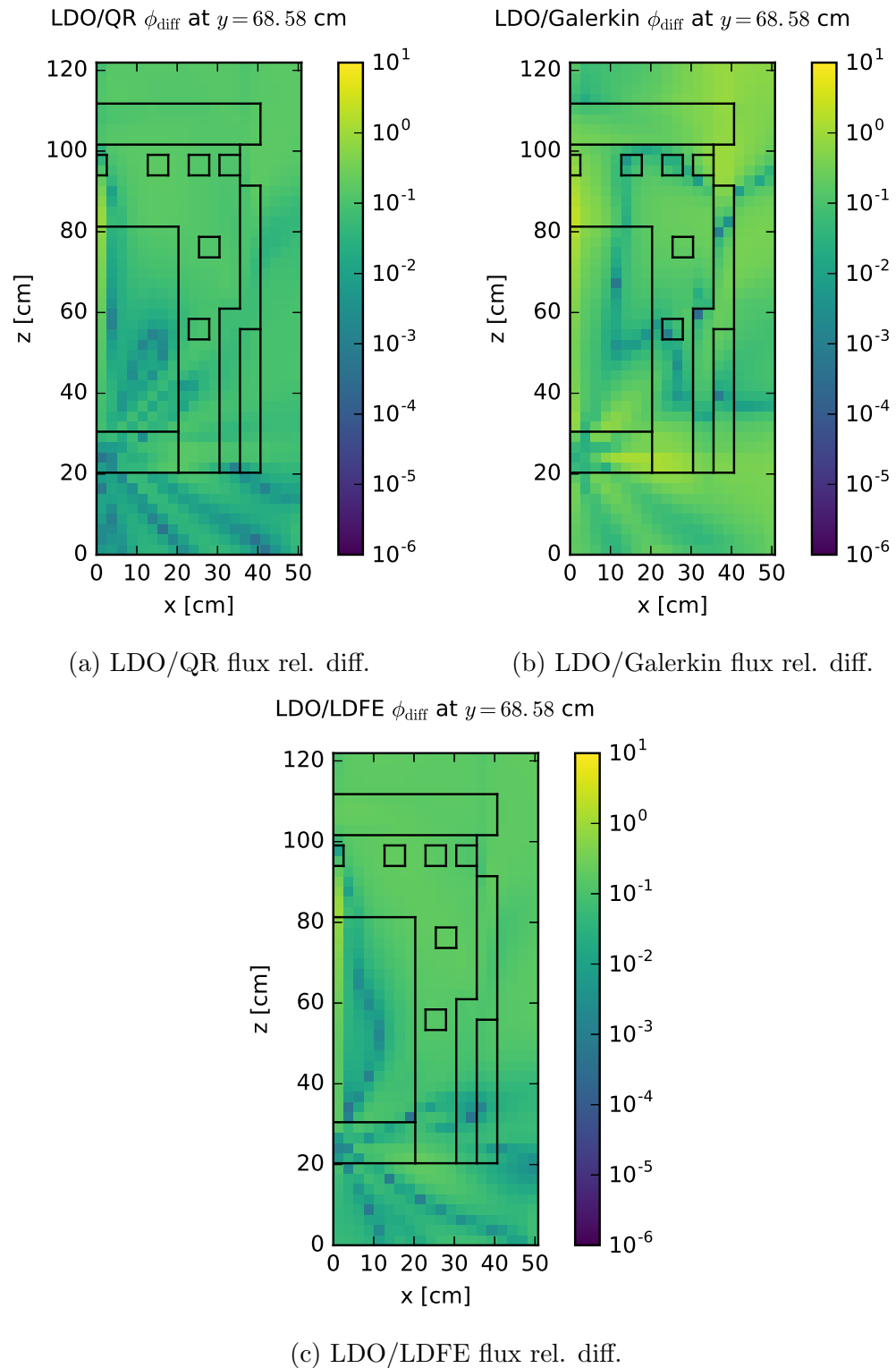


Figure 4.8: DLVN benchmark forward scalar flux relative difference slices.

4.2.4 Ispra Sodium Benchmark

For this test case, the representative LDO quadrature set is of order 9 and has 100 total angles (as opposed to the LDO set of order 11 used for the other cases). Of the LDO quadrature orders listed in Table 4.2, only the smallest four quadrature sets (orders 3, 5, 8, and 9) were available for use with the given test case and computational hardware configuration. Recalling the discussion in Chapter 3, we will point out that, when solving the LDO equations, the angular flux coefficient solution vector scales as the number of discrete angles used in the simulation. This solution vector exists for every energy group in every spatial cell and this particular test case used over 3 million spatial cells. So, the use of the larger LDO quadrature sets was not possible given the parameters listed above in Section 4.1.5.1 because the memory requirement exceeded what was available.

Figure 4.9 shows flux slice plots for each representative quadrature set with outlines of the neutron source, the sodium apparatus boundaries, and the detector locations in the experimental configuration. All plots are at the problem midplane of $y = 0$ cm. Ray effects are particularly apparent in all of the flux slices. Although the particle source is a volume rather than a point, the geometry of the source volume creates the anisotropies observed in the solutions. Additionally, the volume of the source is comparatively small relative to the overall scenario geometry, so we see ray effects on this larger scale.

Let us again look at the differences between the representative LDO flux and the three other quadrature types. As with the previous test cases, the flux difference is calculated using Equation 4.1. Like the DLVN test case, Figure 4.10 shows numerous ray effects. The ray effects are likely exacerbated by the use of a coarser LDO quadrature set, but the primary cause is most likely the anisotropic disk source. Like the preceding two test cases, the worst match is between the LDO and Galerkin results. Here, the comparisons of the LDO flux solution with the QR and LDFE flux solutions look fairly similar, with the areas of best agreement located in the sodium container and the regions of greatest discrepancy located along rays far from the neutron source disk.

As this test case scenario is an actual experimental benchmark, it is pertinent to compare the results of the simulations performed in this work against the experimental data listed in the benchmark. Keeping in mind that this work aims to compare the calculations using LDO quadrature sets with calculations using standard quadrature sets, we present a simplified analysis and comparison here to gauge the representative LDO quadrature set among the representative standard quadrature sets. For each detector location in the sodium block, the absolute saturation activity of the $^{32}\text{S}(\text{n},\text{p})^{32}\text{P}$ reaction was measured experimentally using sulfur detectors. The listed activity values are normalized for varying detector mass such that the activities are listed in becquerels per gram [16].

To compare the scalar flux output resultant from the Exnihilo calculations with the absolute saturation activity values listed in the experimental benchmark, we use the flux values to calculate a reaction rate density [17] comparable with the listed activity values:

$$A = N\sigma\phi, \quad (4.2)$$

where A is the specific activity in becquerels per gram, N is the number density of the sulfur detectors in atoms per gram, σ is the cross section of the $^{32}\text{S}(\text{n},\text{p})^{32}\text{P}$ reaction in cm^2 , and ϕ is the scalar flux at the detector location in neutrons per cm^2 per second. For these calculations, we have used the values of $N = 0.0188 \times 10^{24}$ atoms per gram of sulfur [7] and an average cross section value of $\sigma = 6.5 \times 10^{-26} \text{ cm}^2$ [18]. Additionally, since the neutron source strength is normalized to unity in Exnihilo, the flux values were multiplied by a factor of 1.948×10^{11} , the calculated number of source neutrons per second exiting the source disk in the direction of the detectors [7]. The $^{32}\text{S}(\text{n},\text{p})^{32}\text{P}$ reaction has a threshold of 2.7 MeV [16], so the scalar flux values used in these calculations are those corresponding to the two highest energy groups in the 27n19g library. Results are listed in Table 4.7 with detector #1 located closest to the neutron source and detector #7 located farthest from the source.

Table 4.7: Ispra sodium benchmark experimental and simulated detector activities [Bq/g].

	Det. #1	Det. #2	Det. #3	Det. #4	Det. #5	Det. #6	Det. #7
Exp. Act.	3.237×10^4	1.971×10^3	1.036×10^2	6.270×10^0	4.200×10^{-1}	3.030×10^{-2}	1.990×10^{-3}
Exp. Err.	5.7%	5.7%	5.7%	6.0%	6.0%	6.0%	15.0%
QR	2.472×10^4	7.474×10^2	6.507×10^1	3.142×10^0	8.114×10^{-2}	4.152×10^{-3}	2.446×10^{-4}
Galerkin	2.435×10^4	6.702×10^2	4.460×10^1	1.870×10^0	3.969×10^{-2}	1.665×10^{-3}	7.228×10^{-5}
LDFE	2.463×10^4	7.071×10^2	6.031×10^1	2.787×10^0	6.862×10^{-2}	3.395×10^{-3}	1.953×10^{-4}
LDO	2.471×10^4	7.446×10^2	6.512×10^1	3.087×10^0	7.796×10^{-2}	3.926×10^{-3}	2.255×10^{-4}

It is apparent that the activities calculated using the scalar flux values from Exnihilo do not match those determined experimentally; this is likely due to the simplifications made in the activity calculations using the simulations' scalar flux output. That is, using a finer energy group structure and more sophisticated cross section values would produce detector activities closer to those determined experimentally. However, the values arrived at here are still instructive in analyzing overall physical trends and useful for comparing the LDO quadrature set against the standard quadrature sets.

Table 4.8 lists the ratios of the deterministic activity calculations to the experimental values to explore the behavior of the different quadrature types. For each detector location, the ratio closest to unity is emphasized. It is immediately apparent that the QR scalar flux values are the most closely matching for all detector locations except Detector #3, where the LDO scalar flux value is the closest. Even so, for all detector locations, the LDO ratio value is closer to the QR ratio value than are either the LDFE or Galerkin ratios.

Table 4.8: Ispra sodium benchmark experimental and simulated detector activity ratios.

	Det. #1	Det. #2	Det. #3	Det. #4	Det. #5	Det. #6	Det. #7
QR	0.764	0.379	0.628	0.501	0.193	0.137	0.123
Galerkin	0.752	0.340	0.431	0.298	0.095	0.055	0.036
LDFE	0.761	0.359	0.582	0.445	0.163	0.112	0.098
LDO	0.763	0.378	0.629	0.492	0.186	0.130	0.113

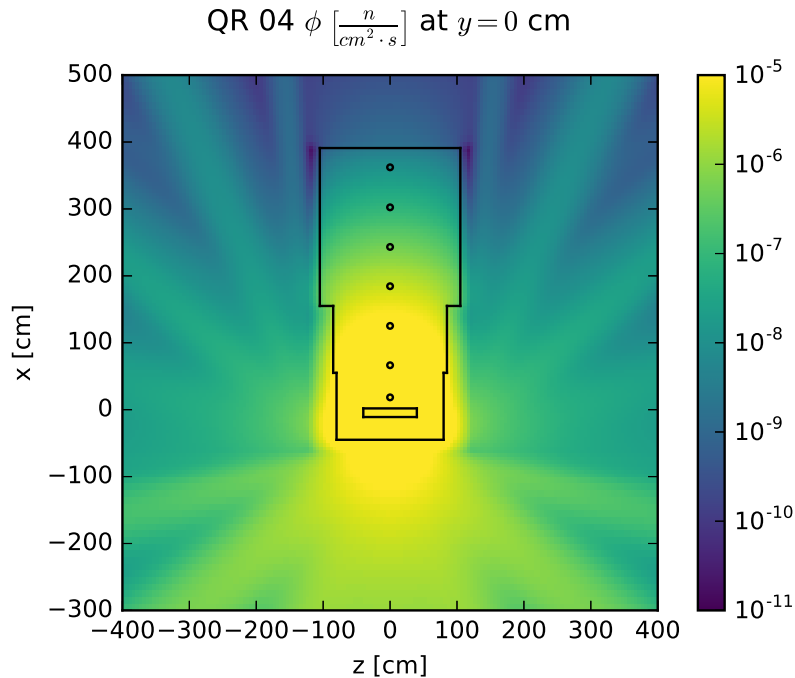
Like the experimental activities, the activities calculated with the deterministic scalar flux values decrease logarithmically as the distance from the source increases. For all of the quadrature types, the calculated activities decrease more quickly than the experimental results. Detectors 2, 3, 5, 6, and 7 all see the deterministically calculated activities at one order of magnitude lower than the respective experimental activities (except for the case of the Galerkin quadrature result at detector 7 which is two orders of magnitude below the experimental activity). One possible reason for these discrepancies is the presence of iron in the structure of the benchmark assembly. As we will discuss more in depth in Section 4.3.1, it is not unexpected that deterministically calculated results in the presence of iron are lower than those seen experimentally.

Table 4.9 lists the extreme and average values of the forward flux solution relative differences shown in Figure 4.10 as well as comparisons of the QR flux solution against those of the Galerkin and LDDE flux solutions. On average, all of the flux solutions show poor agreement, with the best match being a 26% difference between the LDO and LDDE forward flux solutions.

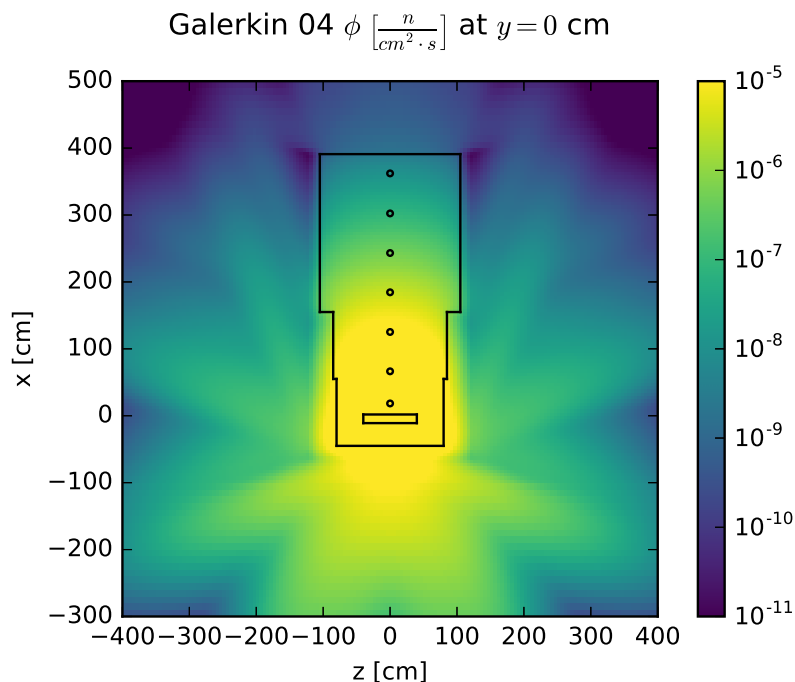
Table 4.9: Ispra sodium benchmark forward flux extremal and average relative differences.

Comparison	Min. Diff.	Max. Diff.	Avg. Diff.
LDO/QR	2×10^{-6}	2.78×10^1	5.00×10^{-1}
LDO/Galerkin	8×10^{-6}	2.38×10^4	6.57×10^1
LDO/LDDE	1×10^{-6}	7.75×10^0	2.61×10^{-1}
Galerkin/QR	3×10^{-6}	1.16×10^0	4.24×10^{-1}
LDDE/QR	7×10^{-6}	2.29×10^1	7.59×10^{-1}

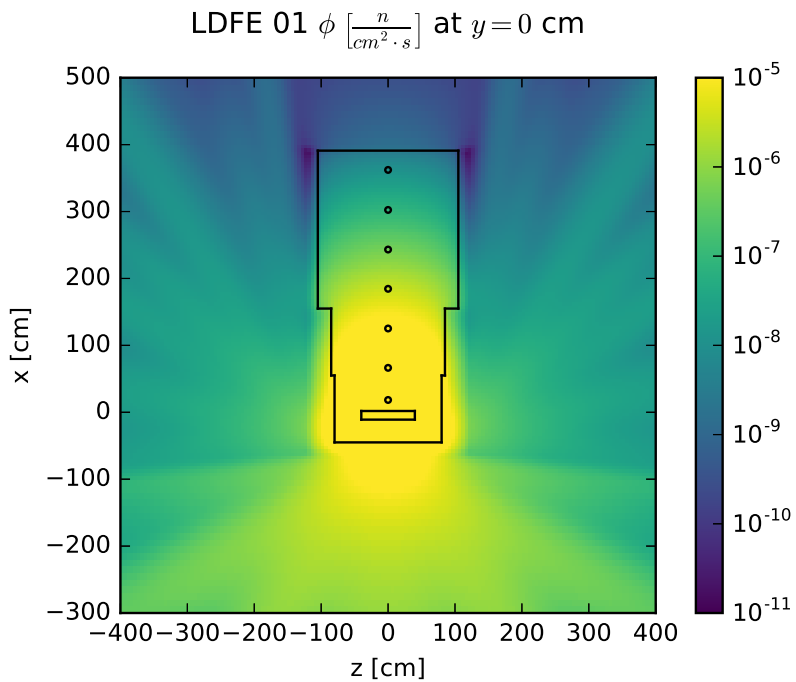
For all of the detector locations, we see in Table 4.7 that the activity calculated with the representative LDO quadrature set demonstrates good agreement with the QR quadrature set. The LDO results in this table match the QR results more closely than do the Galerkin and LDDE results and, of the standard quadrature set results, the LDO results are closest to QR results. We find the LDO results' proximity to the QR results sufficient justification to pursue the exploration of Monte Carlo variance reduction parameter generation using the LDO equations for this test case.



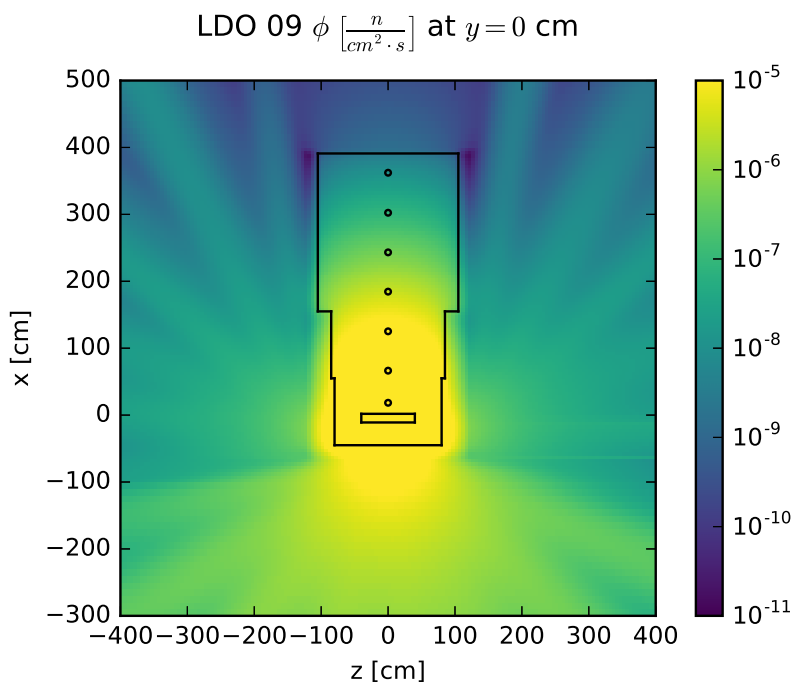
(a) QR forward flux slice.



(b) Galerkin forward flux slice.

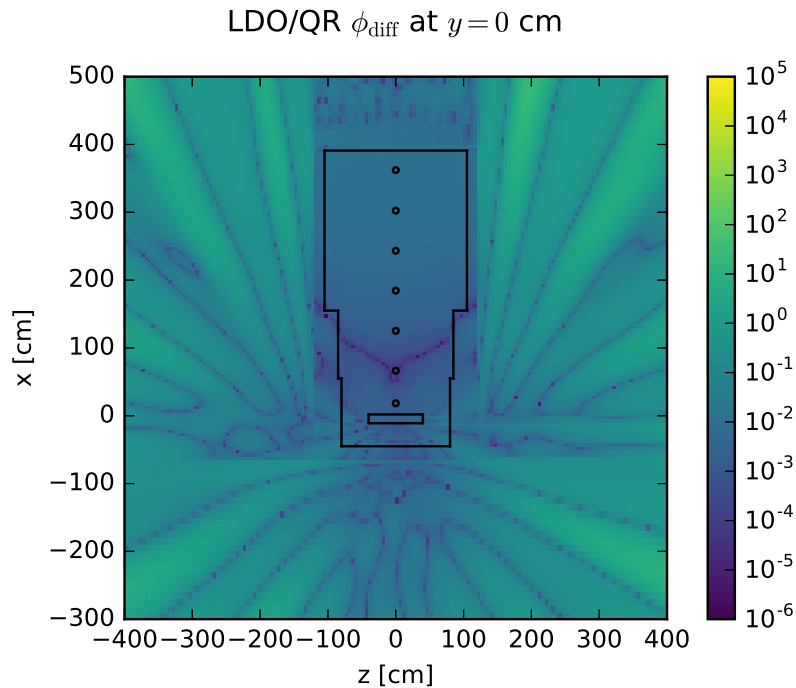


(c) LDFE forward flux slice.

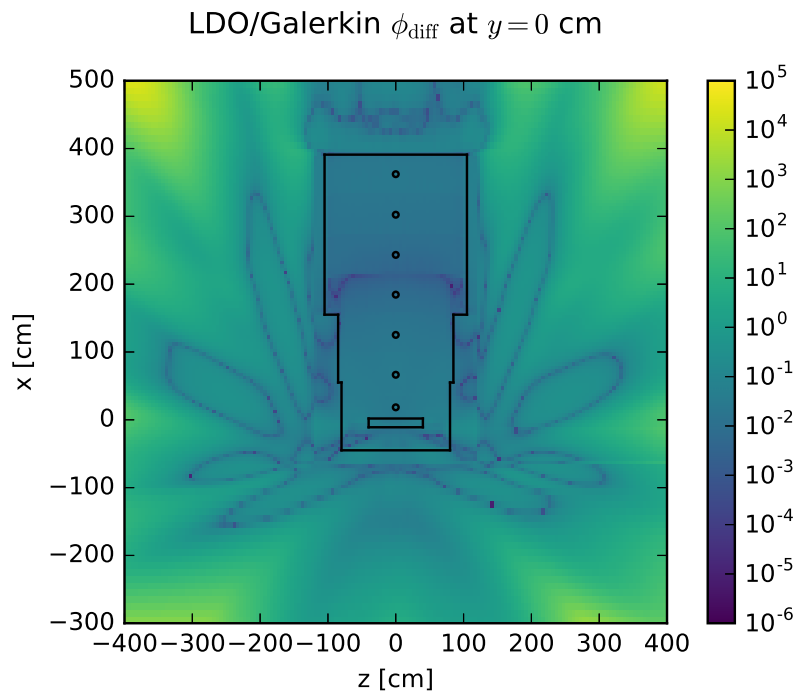


(d) LDO forward flux slice.

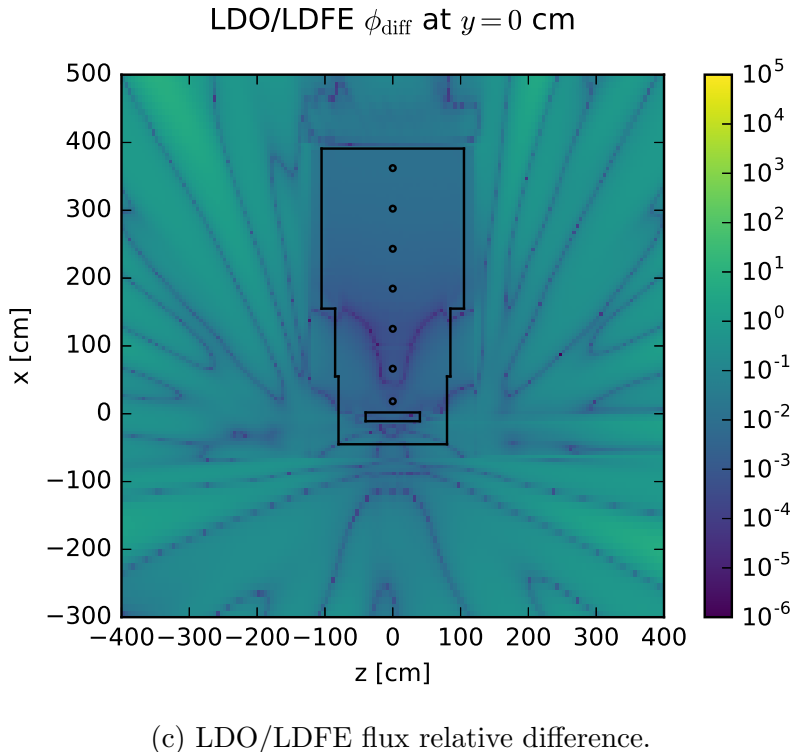
Figure 4.9: Ispra sodium benchmark forward scalar flux slices.



(a) LDO/QR flux relative difference.



(b) LDO/Galerkin flux relative difference.



(c) LDO/LDFE flux relative difference.

Figure 4.10: Ispra sodium benchmark forward scalar flux relative difference slices.

4.2.5 Simplified Portal Monitor

Lastly, we look at the simplified portal monitor problem with the small photon source. Of the test cases presented here, the forward solutions differ most greatly for this problem. Figure 4.11 shows forward scalar flux solutions for the representative quadrature sets with the material pallets, detector array, and shipping container outlines overlaid on the plots. Flux slices are plotted at the midplane of $z = 243.84$ cm (96 inches). All of the flux solutions display ray effects as a result of the streaming paths created by the material variation of the pallets inside of the shipping container.

As with the previous test cases, we look at the differences between the representative LDO flux and the three other quadrature types. Figure 4.12 shows flux differences similar to the difference plots for the Ispra sodium benchmark problem; that is, the differences largely appear as ray effects. This is unsurprising given the combination of the small volume of the photon source in the problem and the inherent difficulty of accurately simulating particle streaming in deterministic calculations. Again we see that the LDO scalar flux solution exhibits strong disagreement with the Galerkin scalar flux solution. The LDO/QR and LDO/LDFE comparison plots show discrepancies of similar orders of magnitude and all of

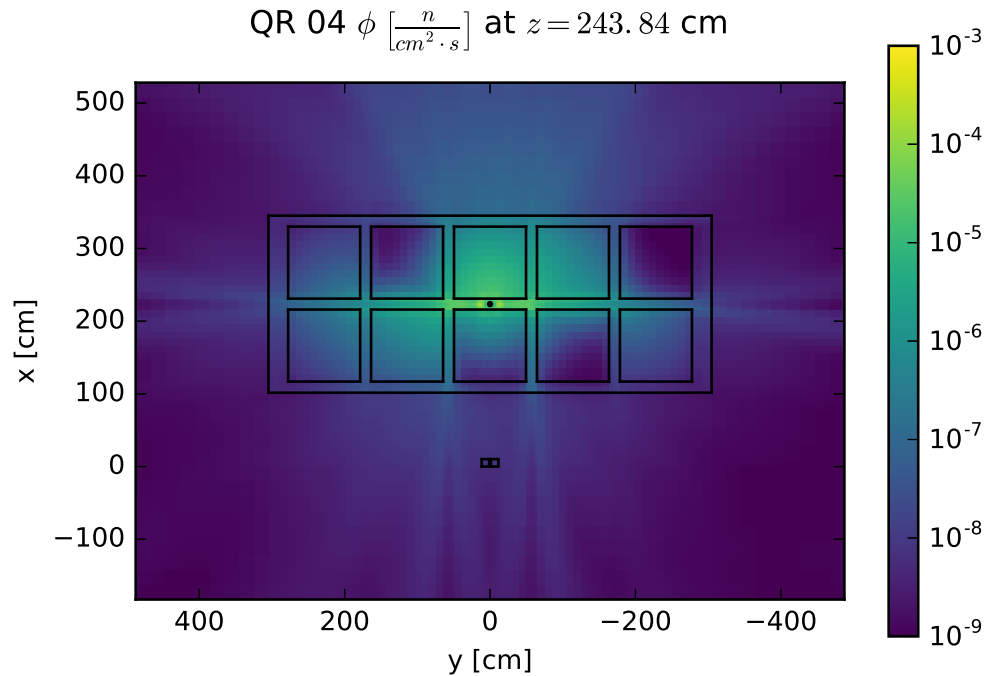
the relative difference plots exhibit the greatest difference along the $y - z$ plane streaming pathway located in the center of the shipping container.

Table 4.10 lists the minimum, maximum, and average values of the relative differences in the forward scalar flux solutions, shown in Figure 4.12. As with all of the previous cases, comparisons between the QR flux solution and the Galerkin and LDFE flux solutions are included for reference. None of the flux solutions in this case show particularly good agreement on average; the closest solutions are the LDFE and QR flux solutions which have an average difference of about 24%. Of the three standard quadrature types, the LDO forward flux solution matches the QR forward flux solution most closely.

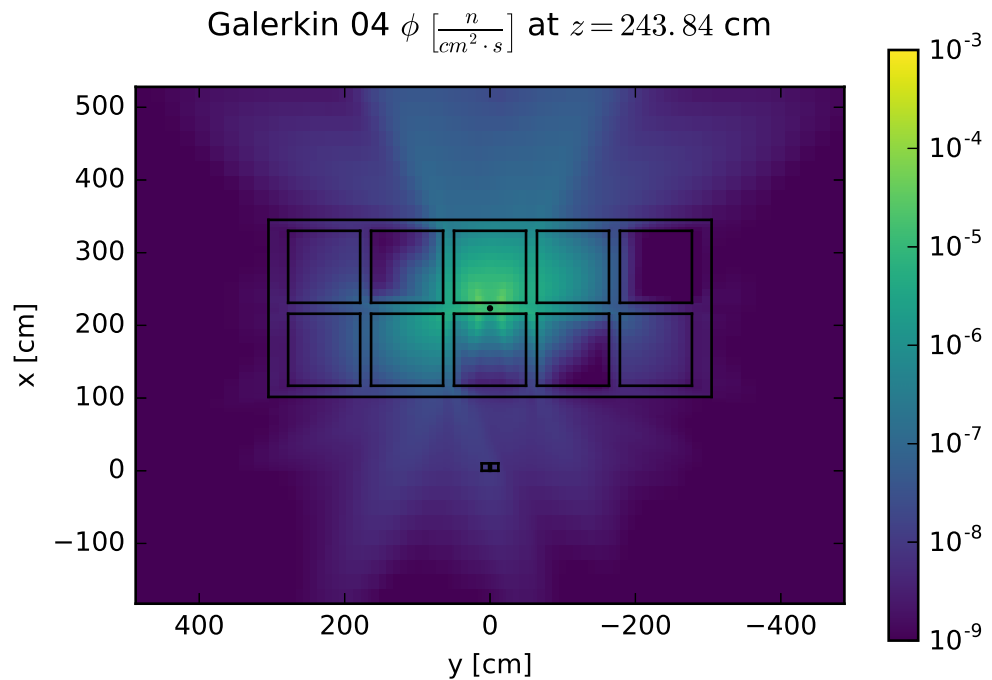
Table 4.10: Portal monitor forward scalar flux extremal and average relative differences.

Comparison	Min. Diff.	Max. Diff.	Avg. Diff.
LDO/QR	1×10^{-6}	1.43×10^2	3.07×10^{-1}
LDO/Galerkin	7×10^{-5}	1.22×10^2	1.96×10^0
LDO/LDFE	6×10^{-5}	1.53×10^2	3.33×10^{-1}
Galerkin/QR	4×10^{-5}	2.47×10^0	3.93×10^{-1}
LDFE/QR	2×10^{-5}	2.09×10^0	2.38×10^{-1}

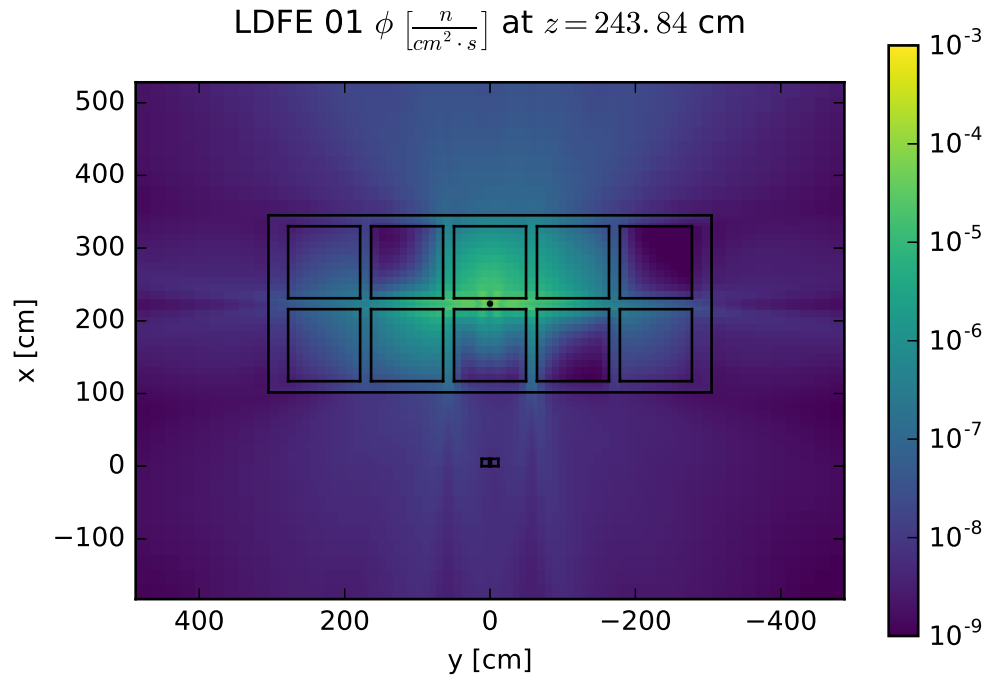
Given the localized small volumetric particle source used in the problem in combination with the streaming pathways created by the scenario's material and geometry configuration, it is unsurprising that the forward flux solutions generated with the various representative quadrature sets show only fair agreement. Still, in the interest of exploring the LDO quadratures' solutions for Monte Carlo variance reduction parameter generation for this problem transporting photons, we will compare the results of the different quadrature sets in the CADIS and FW-CADIS contexts.



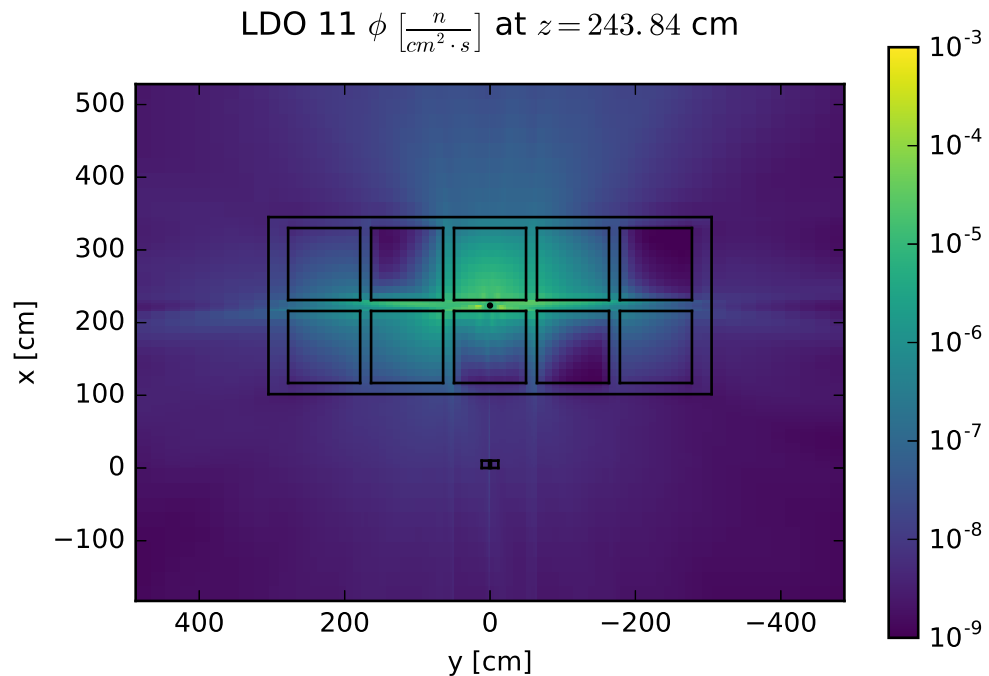
(a) QR forward flux slice.



(b) Galerkin forward flux slice.

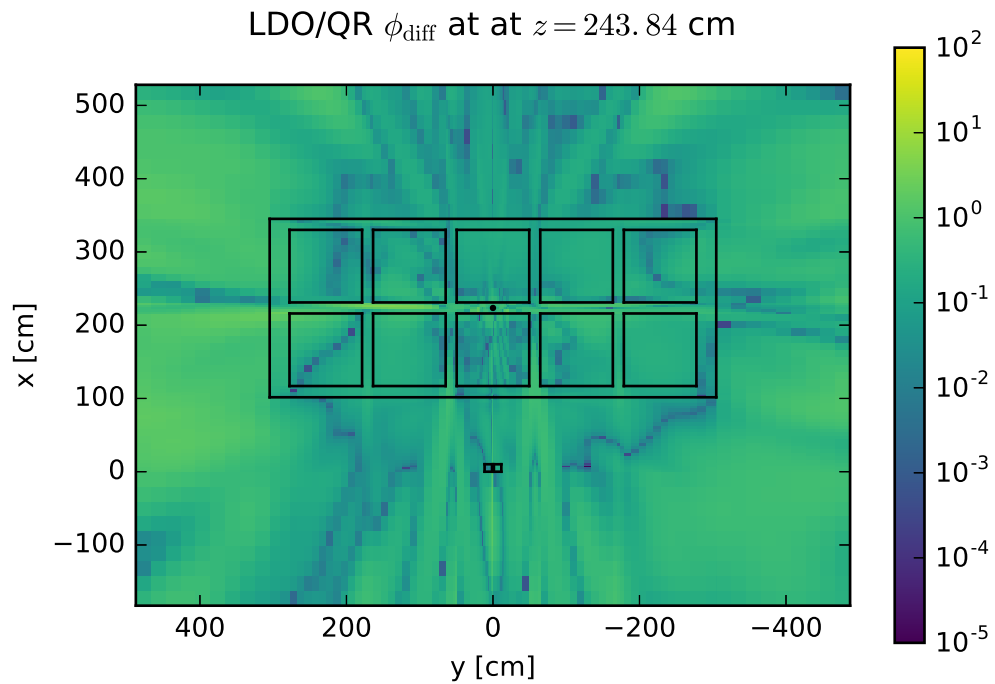


(c) LDFE forward flux slice.

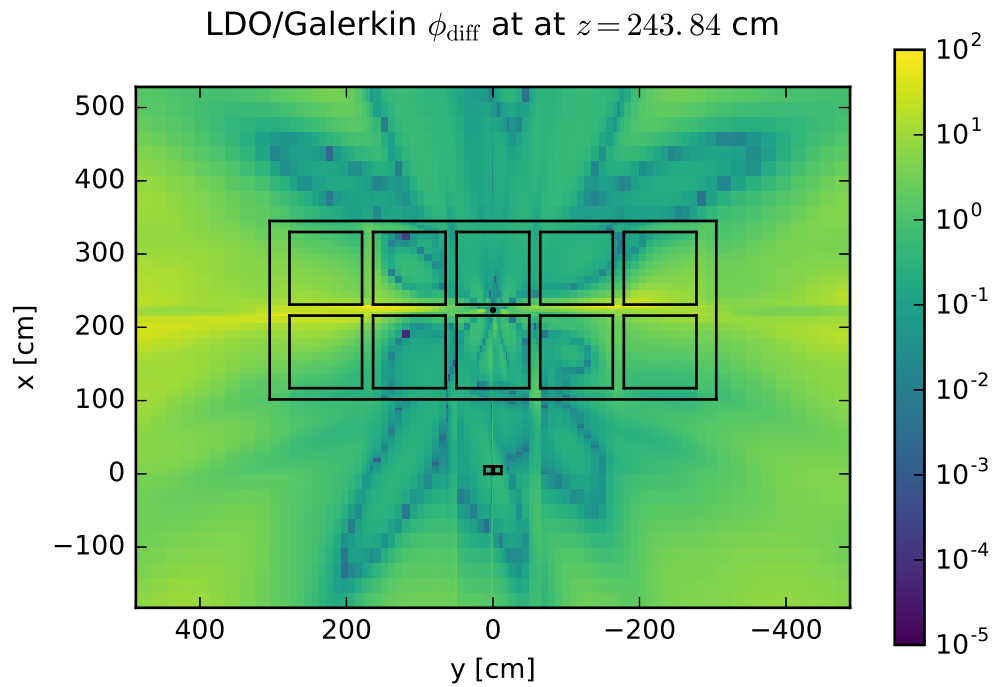


(d) LDO forward flux slice.

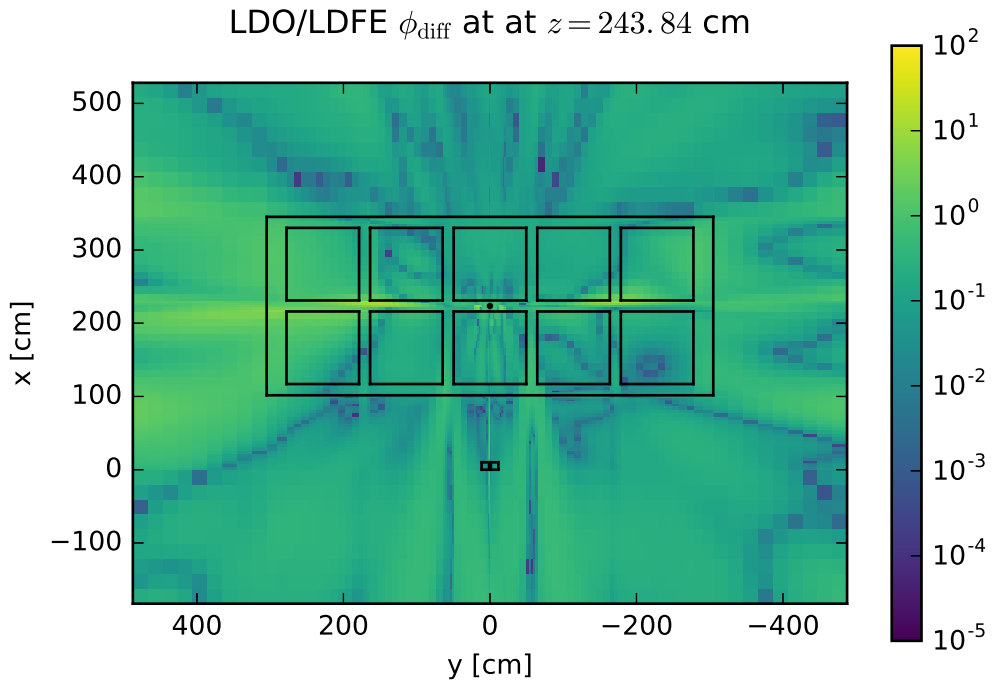
Figure 4.11: Simplified portal monitor scenario forward scalar flux slices.



(a) LDO/QR flux relative difference.



(b) LDO/Galerkin flux relative difference.



(c) LDO/LDFE flux relative difference.

Figure 4.12: Simplified portal monitor scenario forward scalar flux relative difference slices.

4.2.6 Summary

For the test cases here, we have compared the forward scalar flux solutions resultant from solving the LDO equations against those arising from solving the traditional discrete ordinates equations with a small variety of standard quadrature set types. Particular attention was paid to the comparison of the LDO results with the QR results, as QR quadrature sets are commonly used in Monte Carlo variance reduction parameter generation and the larger goal of this work is to assess the efficacy of the LDO equations' solutions in Monte Carlo variance reduction parameter generation. In each test case, the results from solving the LDO equations best matched those from using the QR quadrature set in the traditional discrete ordinates formulation. Additionally, for the two benchmark test cases, the LDO equations produced results that were commensurate to those of all standard quadrature sets when the deterministic results were compared against experimental values.

4.3 CADIS Calculations

Having found that the LDO equations' forward scalar flux solutions are comparable to those of standard quadrature sets, we move on to test the various quadrature sets' performance for

Monte Carlo variance reduction parameter generation. We begin by looking at the test case scenarios in the context of the CADIS method, described in Section 2.2.1.1. Since the CADIS method uses the deterministic adjoint scalar flux solution to generate Monte Carlo variance reduction parameters, it is pertinent to first examine the deterministic adjoint scalar flux solutions for each of the representative quadrature sets for each test case. Then, we move on to the Monte Carlo results to examine the different quadrature types' efficacy in Monte Carlo variance reduction.

4.3.1 Steel Plate in Water

For the CADIS calculations for the steel plate embedded in water, the adjoint source was set to be the detector tally. Figure 4.13 shows the deterministically calculated adjoint scalar flux solutions for the representative quadrature sets. As expected, the flux is highest at the detector location and decreases logarithmically moving backwards along the z -axis. From there, we also examine the relative differences between the LDO solution and those from the standard quadrature sets. Results are shown in Figure 4.14 with extremal and average values listed in Table 4.11. As seen previously, the LDO solution matches the QR solution better than it matches the Galerkin or LDDE solutions. In this case, the LDDE solution has a lower maximum relative difference compared to the QR solution than does the LDO solution, but we see that the LDO solution matches the QR solution more closely than does the LDDE solution on average (4.1% difference versus 12.5% difference).

Table 4.11: Steel plate CADIS adjoint scalar flux extremal and average relative differences.

Comparison	Min. Diff.	Max. Diff.	Avg. Diff.
LDO/QR	3×10^{-5}	4.54×10^{-1}	4.13×10^{-2}
LDO/Galerkin	1×10^{-3}	3.50×10^1	3.27×10^0
LDO/LDDE	5×10^{-5}	6.96×10^{-1}	1.14×10^{-1}
Galerkin/QR	4×10^{-4}	9.71×10^{-1}	4.60×10^{-1}
LDDE/QR	7×10^{-5}	4.26×10^{-1}	1.25×10^{-1}

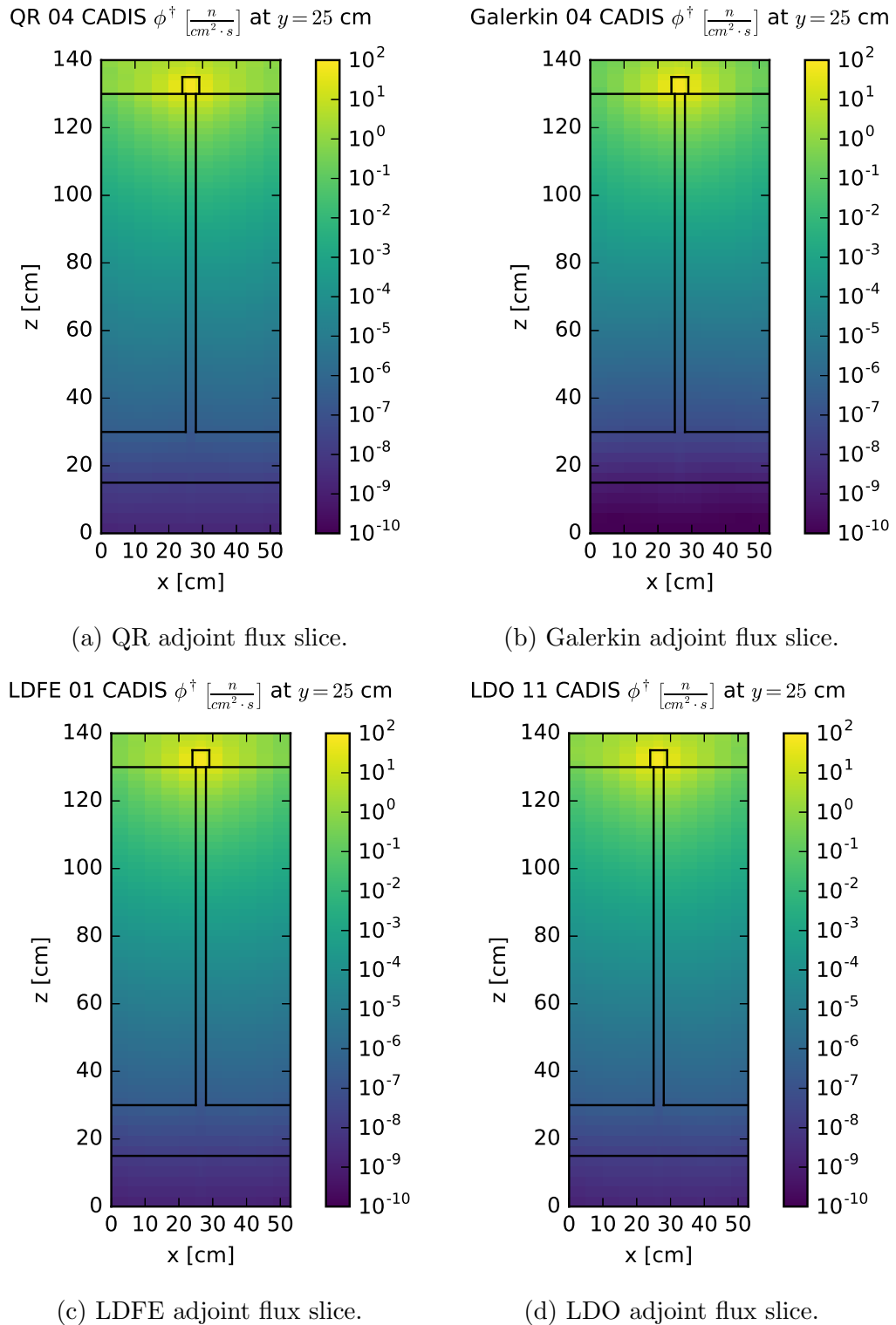


Figure 4.13: Steel plate adjoint scalar flux slices for the CADIS method.

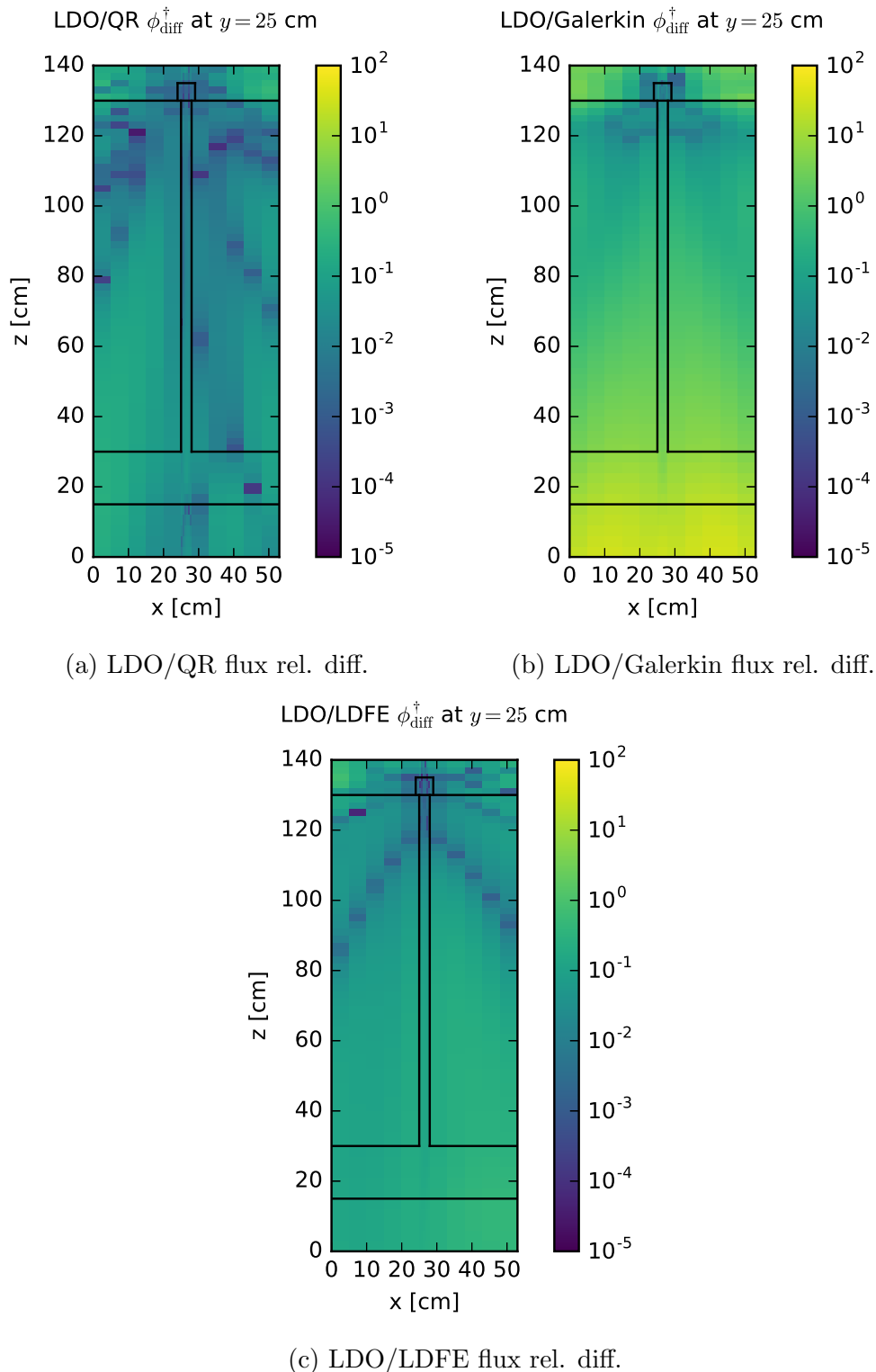


Figure 4.14: Steel plate adjoint scalar flux relative difference slices for the CADIS method.

Following this, we examine the Monte Carlo results; recall that 1×10^9 neutron histories were used in these calculations. Figure 4.15 shows the MCNP-reported flux tally for the detector at the end of the steel plate for each angular mesh refinement for each quadrature type. We note that the Monte Carlo runs with biasing parameters from the Galerkin quadrature set of order 2 and the LDO quadrature set of order 5 were not able to finish in a timely manner for the hardware configuration used in this work, so Monte Carlo results for those two data points are not included here. The flux tally results are plotted as a function of angular mesh refinement to observe the impact of angular mesh refinement on flux tally solution for the different quadrature types. Figure 4.15 also includes the flux tally value for an unbiased Monte Carlo calculation as a reference point of comparison; it is shown as a horizontal black line with dashed lines on either side indicating the one standard deviation confidence interval.

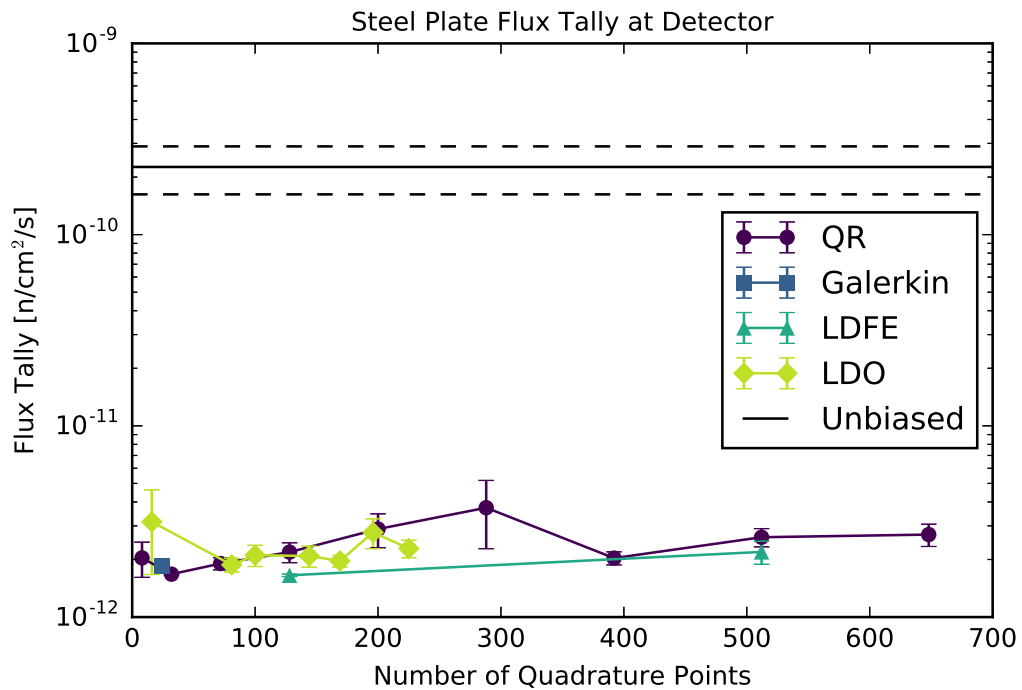


Figure 4.15: MCNP-reported flux tally values at the end of the steel plate.

All of the biased results tend towards a tally calculation on the order of 10^{-12} , while the unbiased tally calculation is on the order of 10^{-10} . We will pause here to explore one reason behind this discrepancy. Figure 4.16 shows the MCNP-reported flux tally broken down into energy bins with boundaries set to those of the 27n19g library. In this plot, only tallies corresponding to calculations using biasing parameters from the four representative quadrature sets are included. We see an extreme difference in the results from the biased calculations versus the results from the unbiased calculation between neutron energies of 1 keV and 1 MeV.

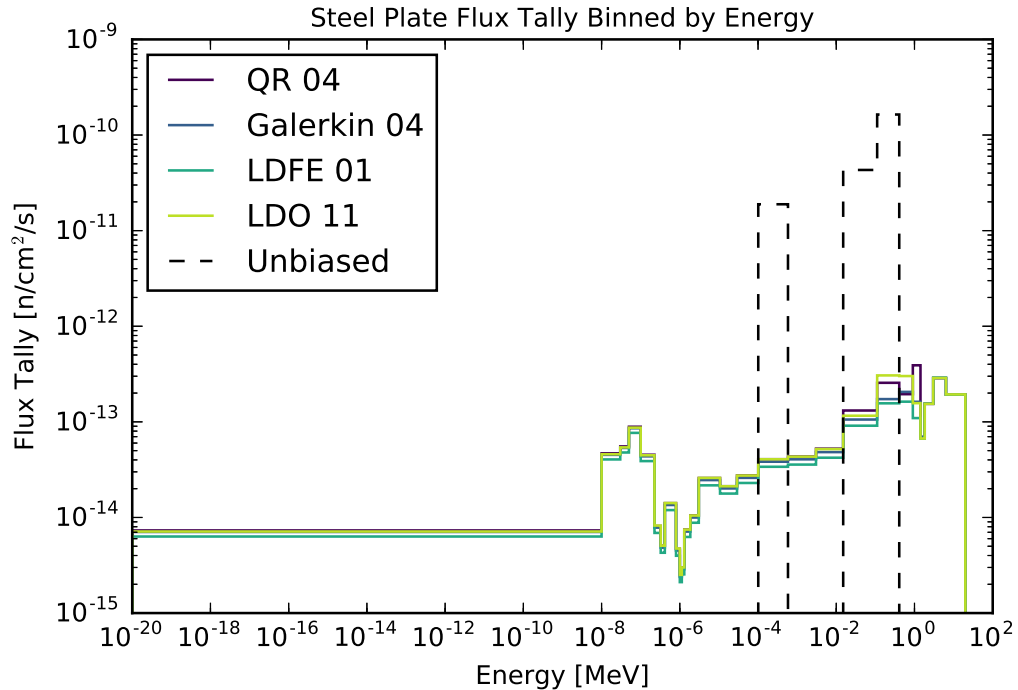


Figure 4.16: Steel plate detector tally broken down by energy bin.

This phenomenon has been previously documented [1] and can be largely attributed to the resonances in the iron cross section, shown in Figure 4.17 with the 27n19g library energy group boundaries overlaid. The unresolved resonance region in the iron cross section spans multiple energy groups, leading to inaccuracies in the discretized multigroup cross section values used in deterministic calculations. To put this directly in the context of the test case scenario at hand, Figure 4.18 shows the detector tally broken down by energy bin overlaid on the iron total cross section. Unsurprisingly, the energy regions of large discrepancy are those in which the iron cross section resonances lie.

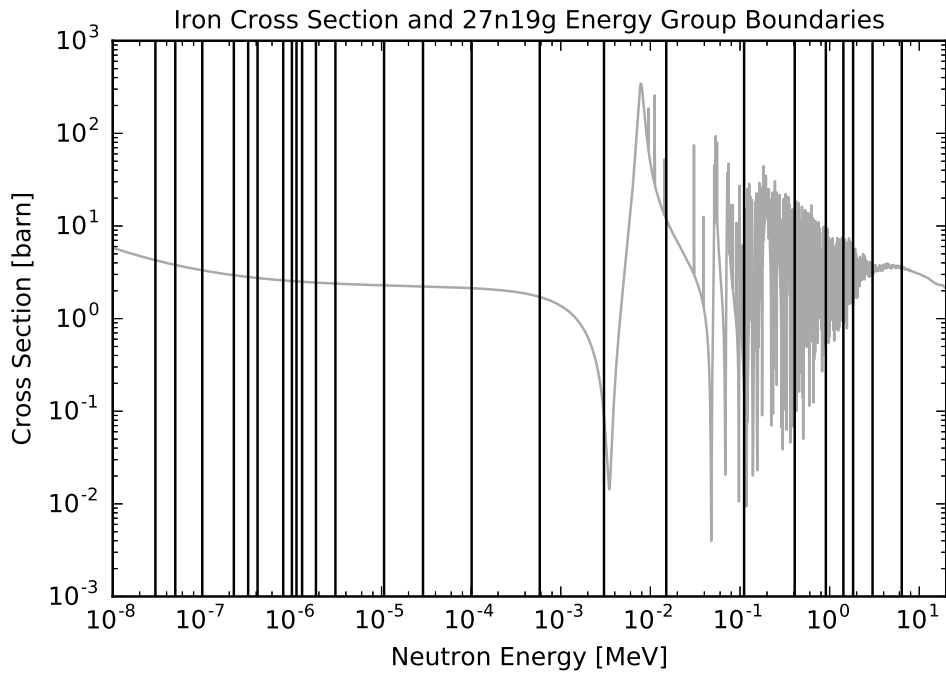


Figure 4.17: ENDF iron total reaction cross section with 27n19g energy group limits [19, 8].

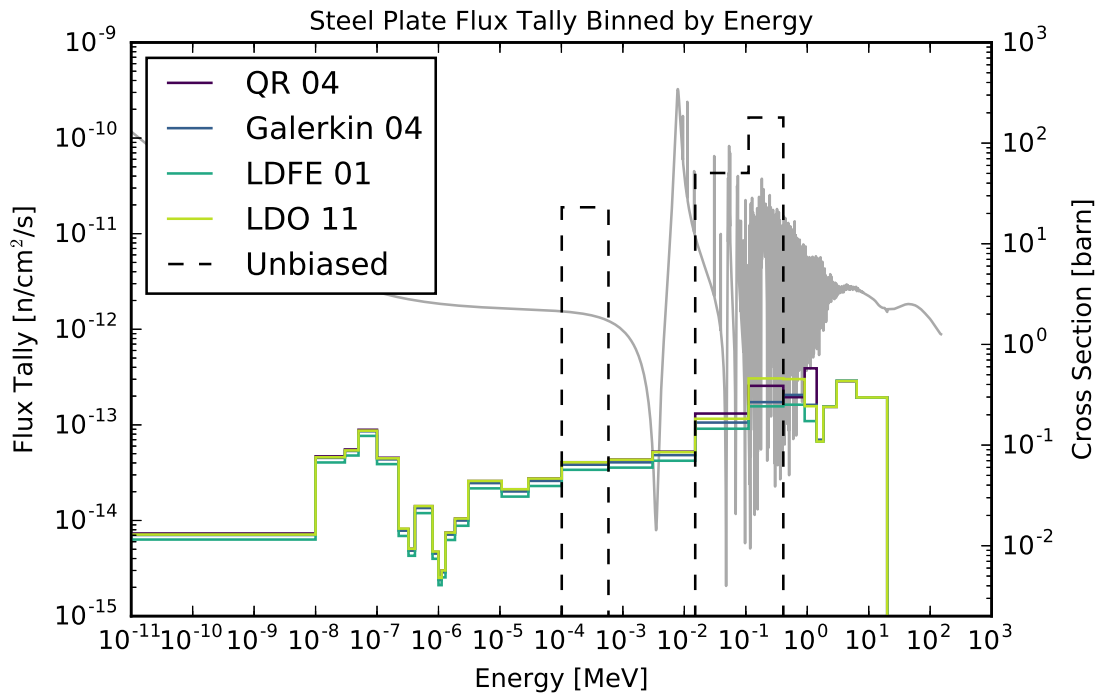


Figure 4.18: Steel plate detector tally broken down by energy bin with iron cross section.

Having explored the discrepancy between the biased and unbiased tally results, we move on to looking at the Figures of Merit for the various Monte Carlo run results. Figure 4.19 shows the reported FOM value for the detector tally for the various quadrature sets and orders. We again plot the results as a function of angular mesh refinement with a black horizontal line denoting the FOM for the unbiased Monte Carlo calculation. The biasing parameters corresponding to the LDFE quadrature set of order 1 result in the highest FOM value while those of the QR set of order 1 result in the lowest FOM value. For all LDO quadrature sets of order 8 and above, the Figures of Merit are one order of magnitude greater than that of the unbiased calculation.

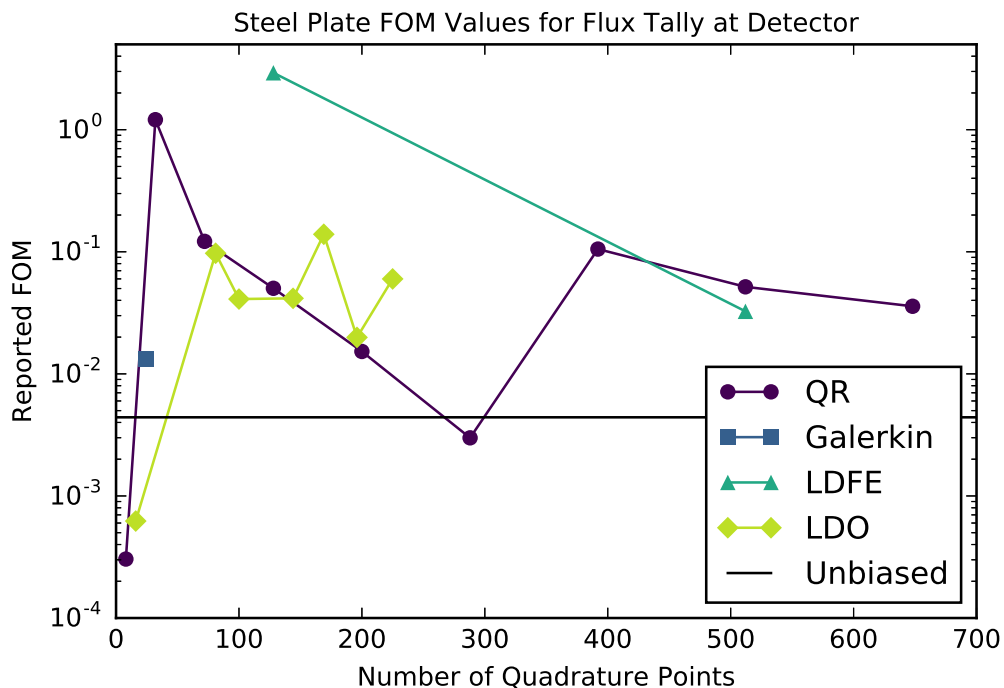


Figure 4.19: FOM values for MCNP flux tally at the end of the steel plate.

To conclude this section, we consider the overall trends in angular mesh refinement in Figures 4.15 and 4.19. It appears that the angular mesh refinement does not have a great impact on the flux tally value in this scenario, as all of the biased tally results fall within the same order of magnitude and do not exhibit any trends as a function of the number of discrete angles used. The Figures of Merit vary somewhat more greatly. Specifically, the LDO biasing parameters appear to gather around FOM values of 0.005 even as the number of discrete angles used is increased. So, for the steel plate in water detector tally in the context of the CADIS method, one could use a relatively low-order (i.e., order 8) LDO quadrature set to generate Monte Carlo biasing parameters that result in a Figure of Merit comparable to (and better than most of, as seen here) those produced by finer angular meshes.

4.3.2 DLVN

To study the DLVN problem in the context of the CADIS method, the adjoint source was set to be the tally located at detector #14 in the original experiment. All of the adjoint scalar flux solutions shown in Figure 4.20 reflect this; the adjoint flux is highest at the specified detector location. The differences in the adjoint scalar flux solutions shown in Figure 4.21 appear as ray effects from the relatively localized source at the detector location as well as in the streaming pathway in the dog-legged void section. Table 4.12 lists the extremal and average values of the relative differences between the LDO and standard quadrature results. Comparisons between the Galerkin and LDDE quadrature sets versus the QR set are also given for reference. On average, the LDO adjoint flux solution agrees best with the QR adjoint flux solution with a difference of approximately 3.8%.

Table 4.12: DLVN CADIS adjoint scalar flux extremal and average relative differences.

Comparison	Min. Diff.	Max. Diff.	Avg. Diff.
LDO/QR	1×10^{-5}	1.24×10^0	3.78×10^{-2}
LDO/Galerkin	3×10^{-4}	5.01×10^0	3.56×10^{-1}
LDO/LDDE	2×10^{-5}	9.67×10^{-1}	6.04×10^{-2}
Galerkin/QR	6×10^{-1}	7.62×10^{-1}	2.00×10^{-1}
LDDE/QR	2×10^{-5}	3.07×10^{-1}	5.31×10^{-2}

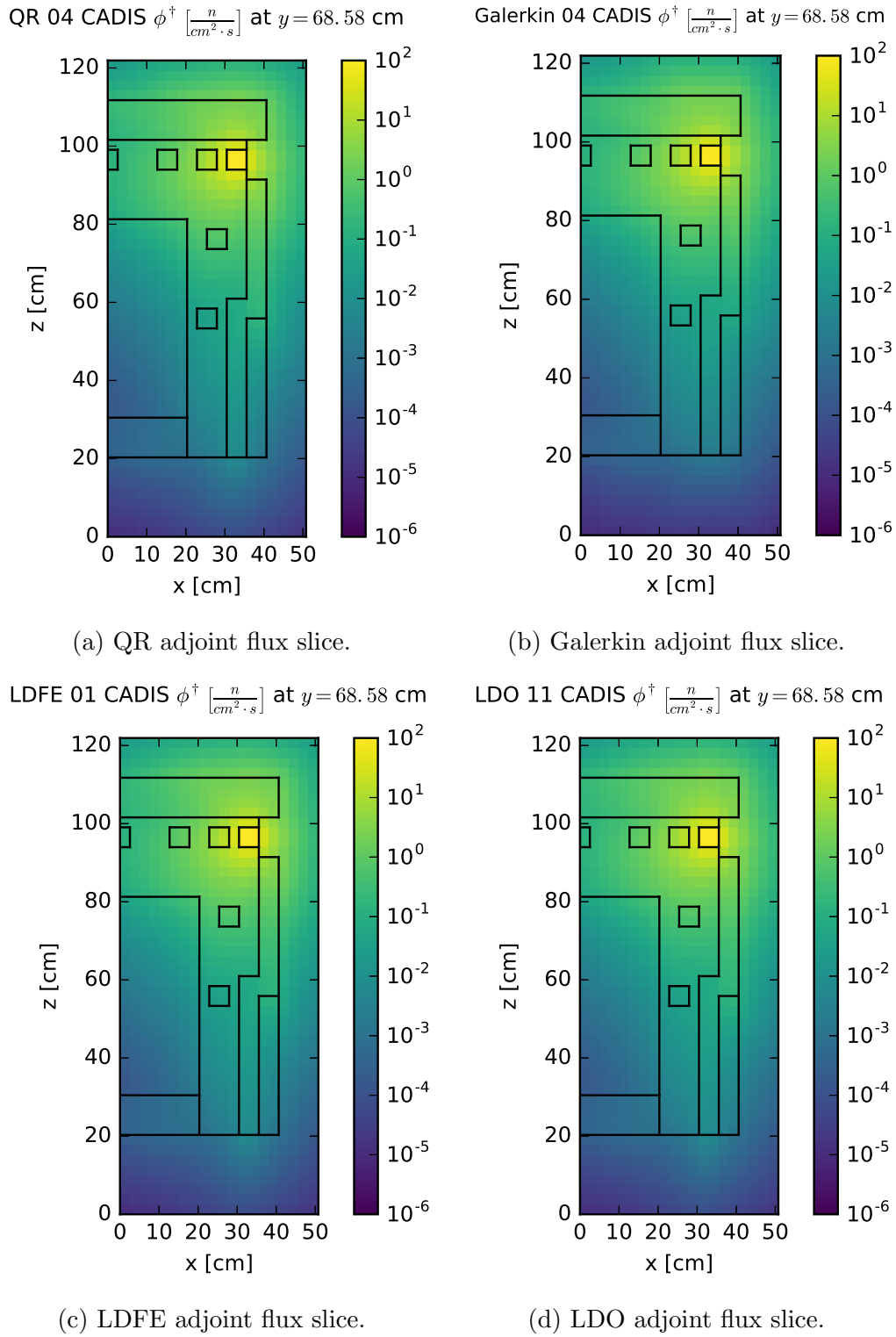


Figure 4.20: DLVN adjoint scalar flux slices for the CADIS method.

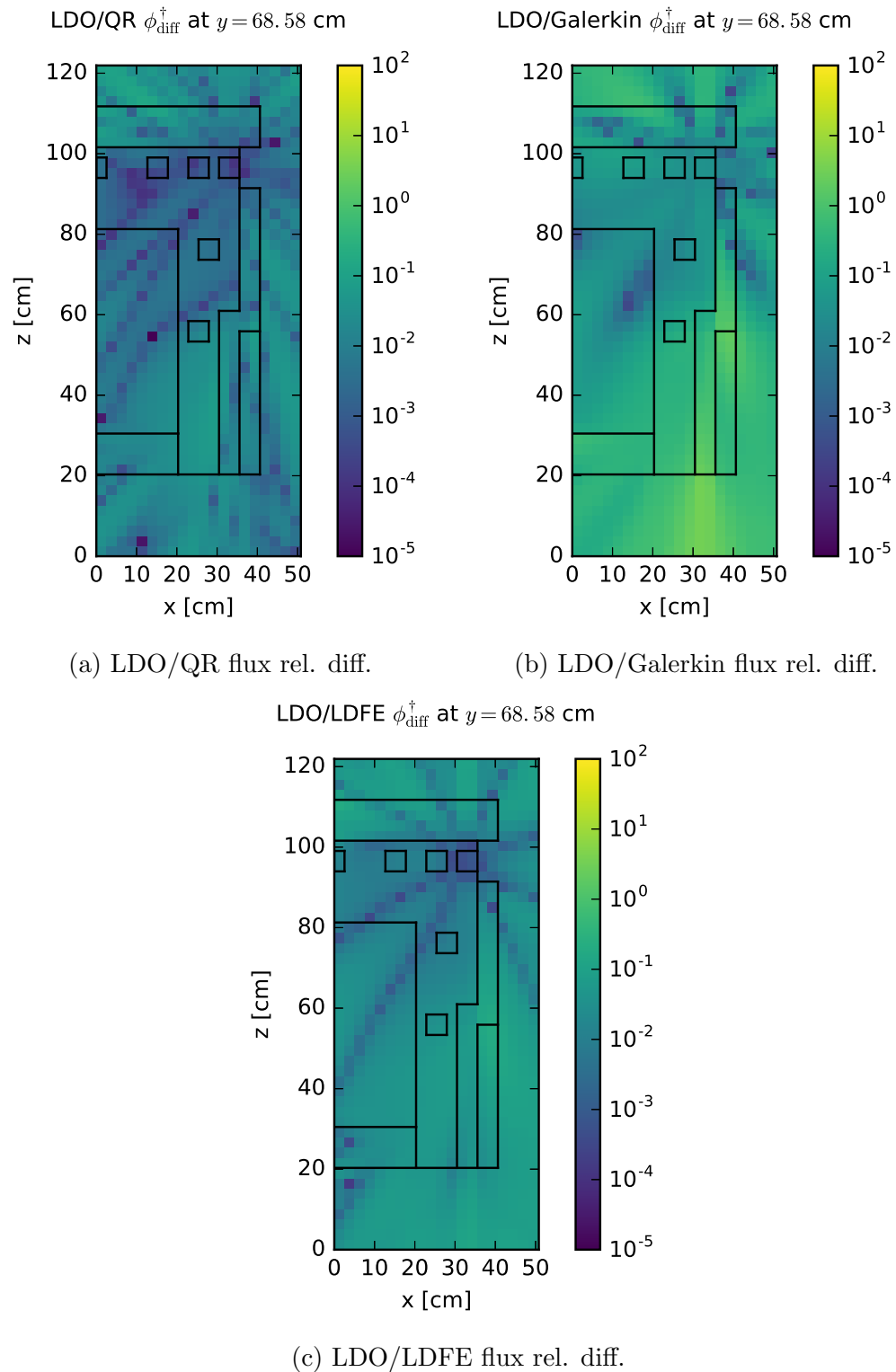


Figure 4.21: DLVN adjoint scalar flux relative difference slices for the CADIS method.

Moving forward, we look at the Monte Carlo results. For the DLVN case, 1×10^{10} neutron histories were simulated. Since the CADIS method is for one local adjoint source, which we have set to detector #14 here, the discussion in this section will focus on the results for this specific detector location. Figure 4.22 shows the MCNP-reported tally for the forward scalar flux at the location of detector #14. Here we see that all of the biased calculation values fall within the error of the unbiased result. However, all of these tally calculations (biased and unbiased) do not match the experimentally calculated flux value of $2.74 \times 10^{-7} \pm 5\%$ n/cm²/s at detector #14.

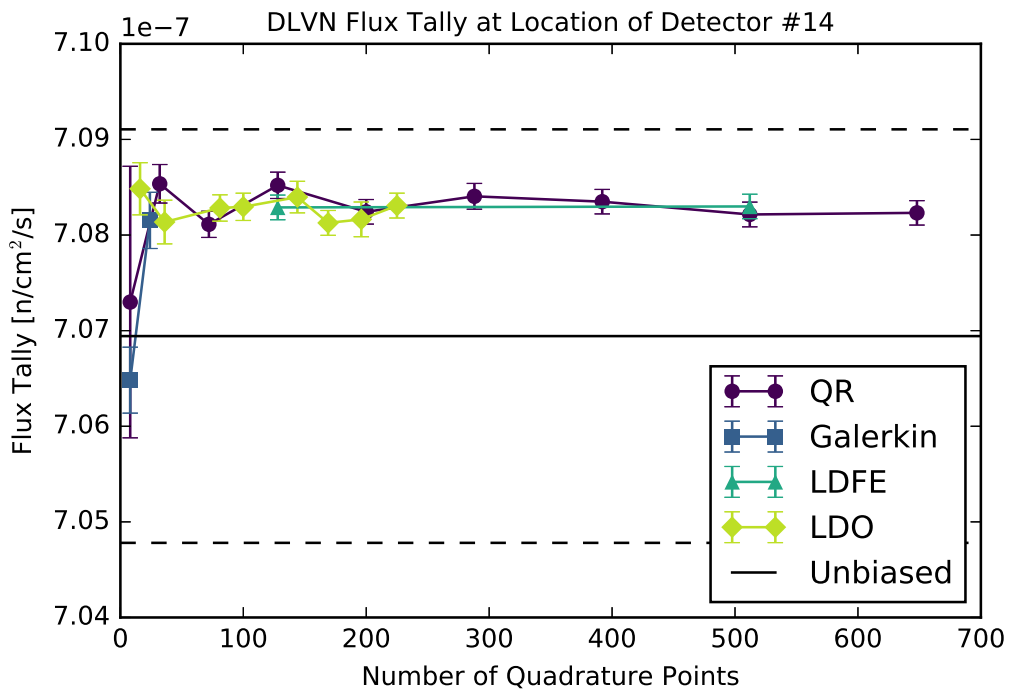


Figure 4.22: Flux tally at detector #14 in the DLVN problem with the CADIS method.

Figures 4.22 and 4.23 show similar convergence behavior with respect to angular mesh refinement for the biased tally calculations and Figure of Merit values. Beyond the lowest-order angular mesh refinement for each quadrature type studied here, the tally result for this detector location using the CADIS method is not impacted by further refining the angular mesh. The Figures of Merit for the tally calculations reach a similar upper bound, but this happens more slowly with respect to angular mesh refinement for the LDO quadrature sets. Like the tally in the steel plate case above, the LDO quadrature set of order 8 is the optimal choice with respect to flux tally result and FOM value for detector #14 in the DLVN experimental benchmark problem in the CADIS context.

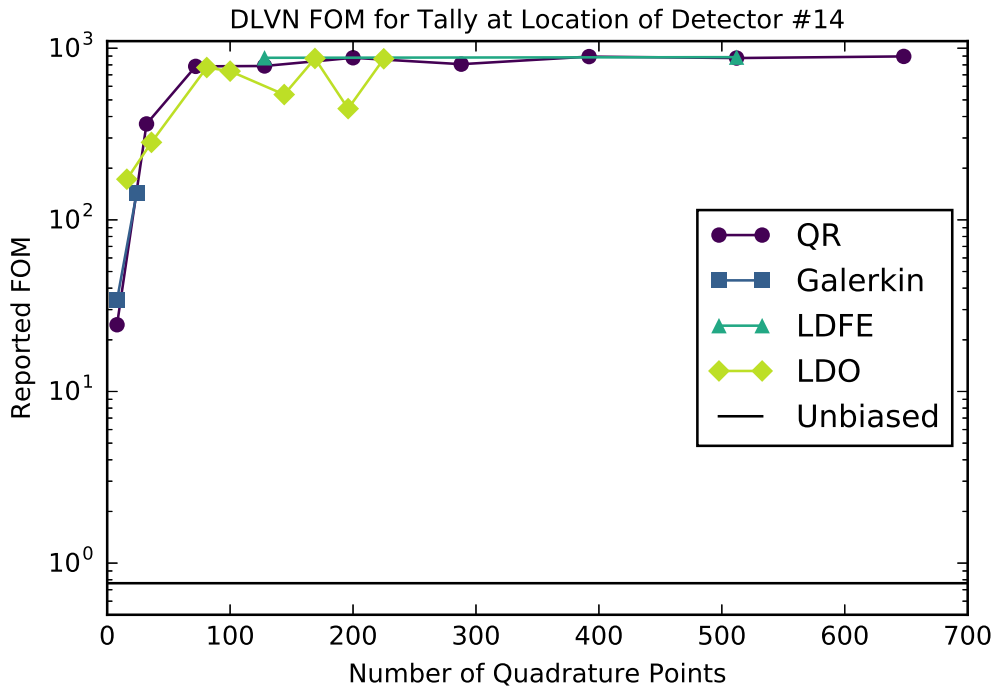


Figure 4.23: FOM values for the DLVN problem detector #14 tally with the CADIS method.

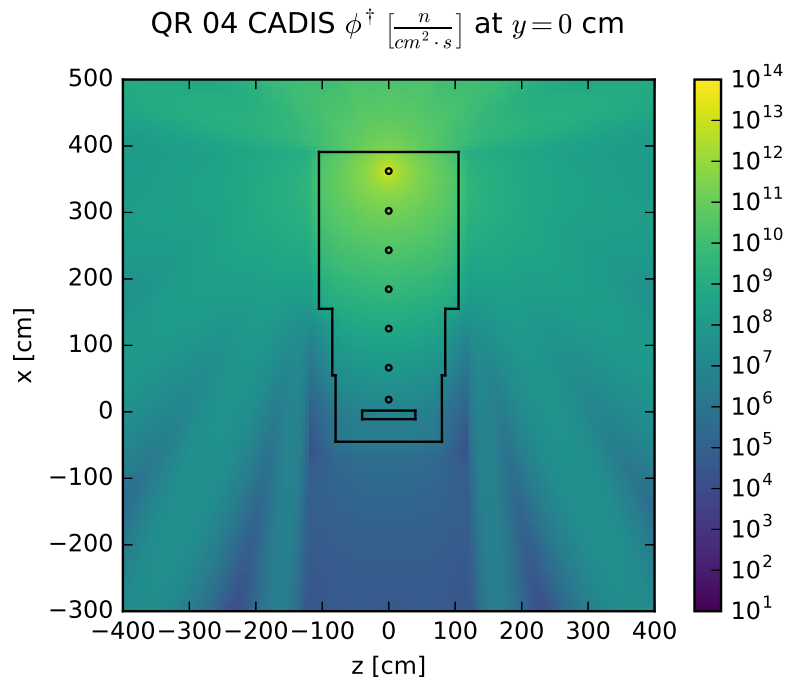
4.3.3 Ispra Sodium Benchmark

For these CADIS calculations, the adjoint source was set to be the detector location farthest from the experimental neutron source. As with the previous cases, we will first examine the adjoint scalar flux solutions and then move on to the Monte Carlo results. The representative LDO quadrature set used in the deterministic calculations here is of order 9 with only 100 total angles and is coarser than the other representative quadrature sets.

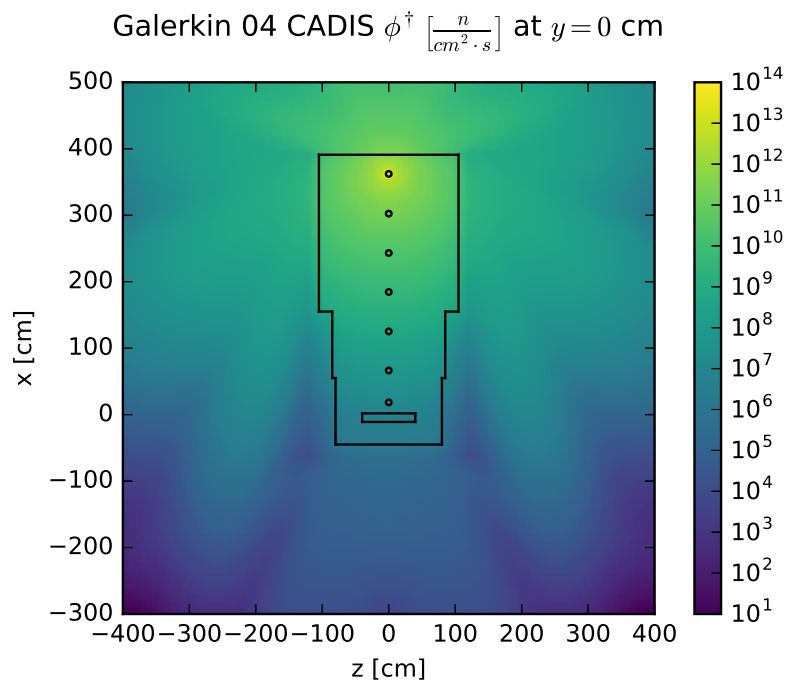
The adjoint scalar flux solutions are shown in Figure 4.24 with relative differences plotted in Figure 4.25 and listed in Table 4.13. Since this source is relatively localized in the overall problem scale, ray effects are seen in the adjoint flux solutions as well as in the relative difference plots. For this case, the Galerkin adjoint scalar flux matches most closely with the QR adjoint scalar flux; a finer LDO angular mesh would likely show better agreement.

Table 4.13: Ispra sodium test CADIS adjoint flux extremal and average relative differences.

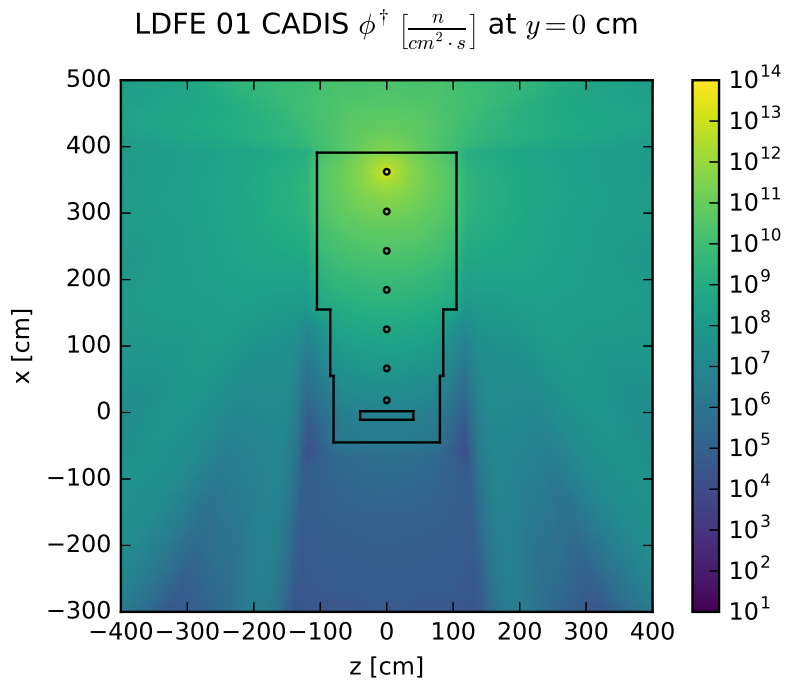
Comparison	Min. Diff.	Max. Diff.	Avg. Diff.
LDO/QR	1×10^{-8}	1.46×10^2	9.71×10^{-1}
LDO/Galerkin	2×10^{-5}	2.52×10^5	5.74×10^2
LDO/LDFE	1×10^{-6}	3.32×10^2	1.28×10^0
Galerkin/QR	5×10^{-6}	1.00×10^0	4.62×10^{-1}
LDFE/QR	6×10^{-7}	8.10×10^1	1.19×10^0



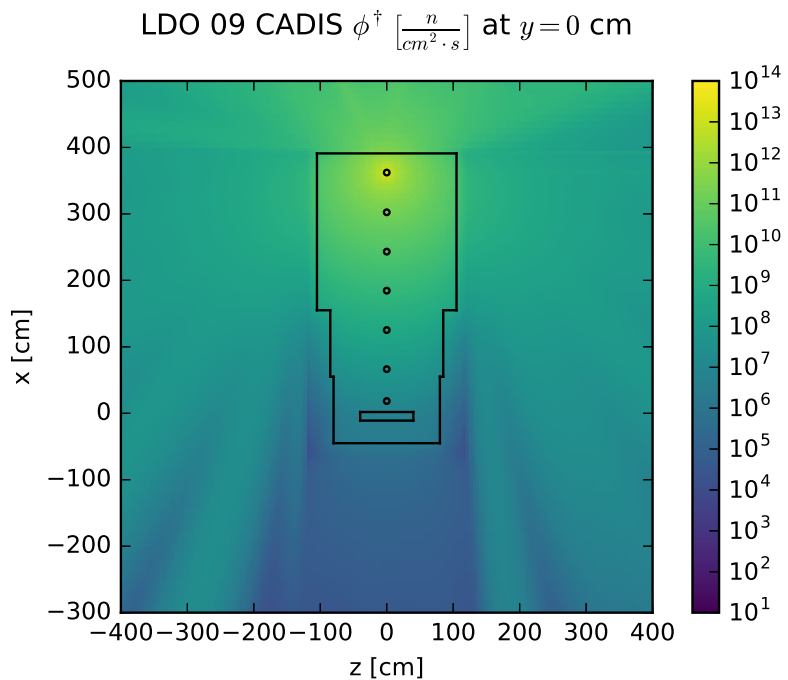
(a) QR adjoint flux slice.



(b) Galerkin adjoint flux slice.

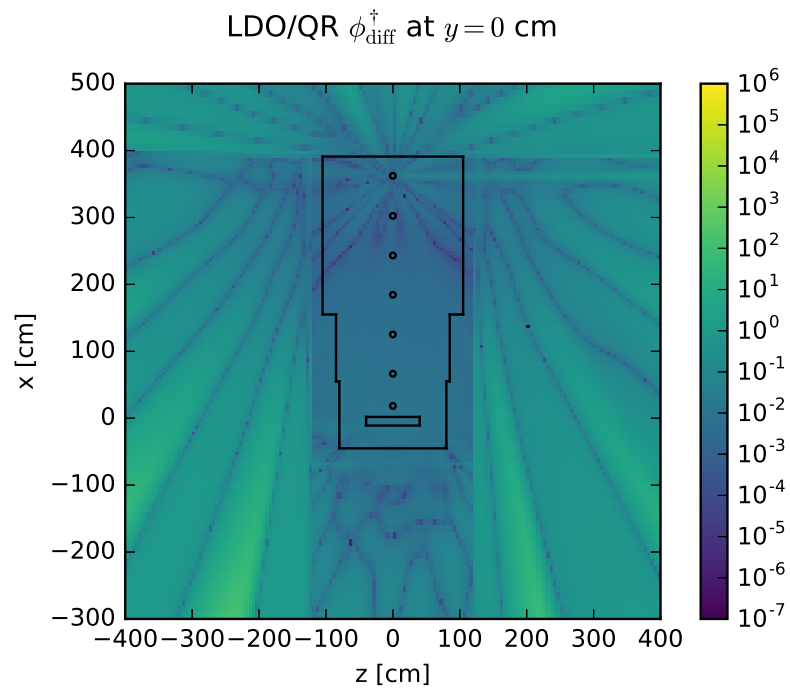


(c) LDFE adjoint flux slice.

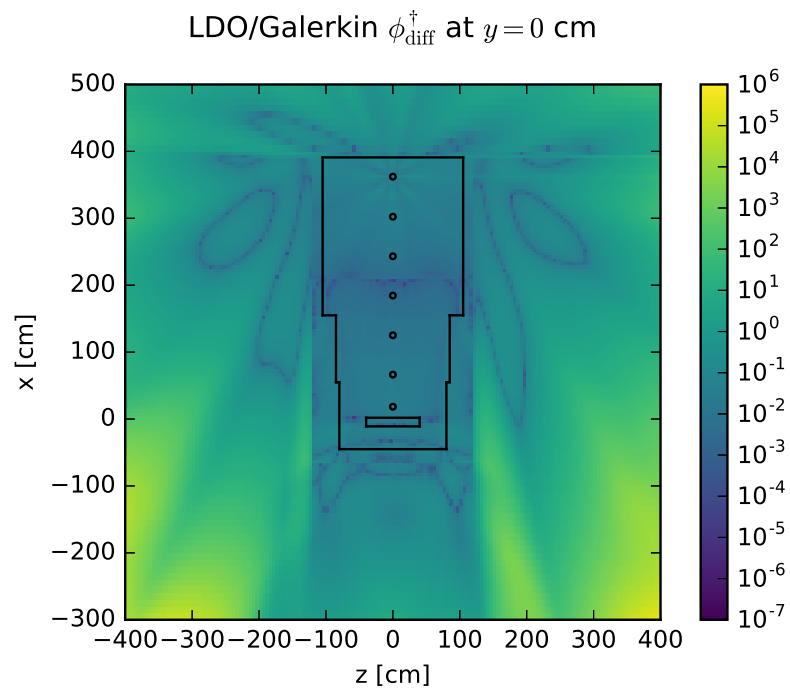


(d) LDO adjoint flux slice.

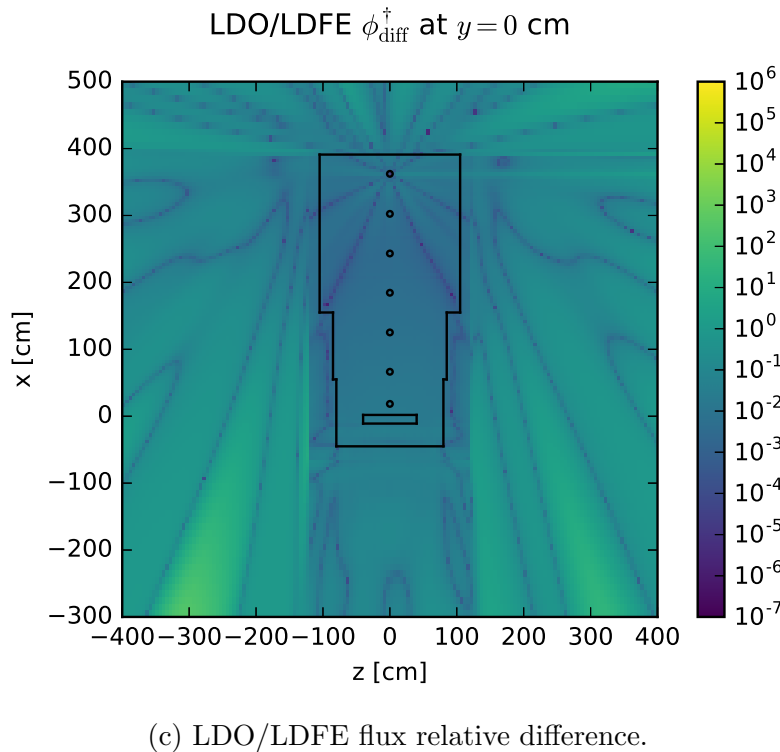
Figure 4.24: Ispra sodium adjoint scalar flux slices for the CADIS method.



(a) LDO/QR flux relative difference.



(b) LDO/Galerkin flux relative difference.



(c) LDO/LDFE flux relative difference.

Figure 4.25: Ispra sodium adjoint scalar flux relative difference slices for the CADIS method.

Again, we will focus the analysis here on the Monte Carlo results for the detector location set to be the adjoint source in the CADIS context. Here, 1×10^9 neutron histories were simulated. Figure 4.26 shows the calculated activity values for the far detector location as a function of angular mesh refinement. All activity values were calculated using the forward scalar flux reported by MCNP in combination with Equation 4.2 and the data listed in Section 4.2.4. All of the biased results fall well within the statistical error of the unbiased calculation, but the calculations are all four orders of magnitude greater than the experimentally calculated activity of 0.00199 Bq/g listed in Table 4.7. One likely reason for this is that the MCNP flux tallies used in these calculations include neutrons of all incident energies and not only those above the threshold for the $^{32}\text{S}(\text{n},\text{p})^{32}\text{P}$ reaction measured experimentally.

Figure 4.26 exhibits no trend for the calculated activity with respect to angular mesh refinement; the coarsest angular mesh of each quadrature type studied here is sufficient to achieve the same forward flux tally and calculated activity value. The FOM values plotted in Figure 4.27 show differing trends for the different quadrature types. The QR biasing parameters tend toward a Figure of Merit of approximately 1000, with the exception of those from the quadrature set of order 4. Of the LDO quadrature sets tested here, the best performance comes from the coarsest angular mesh, with the finest angular mesh not far behind. So, for the Ispra sodium benchmark case in the CADIS method context, the LDO quadrature set of order 3 would be the best one to use (of the LDO quadrature sets).

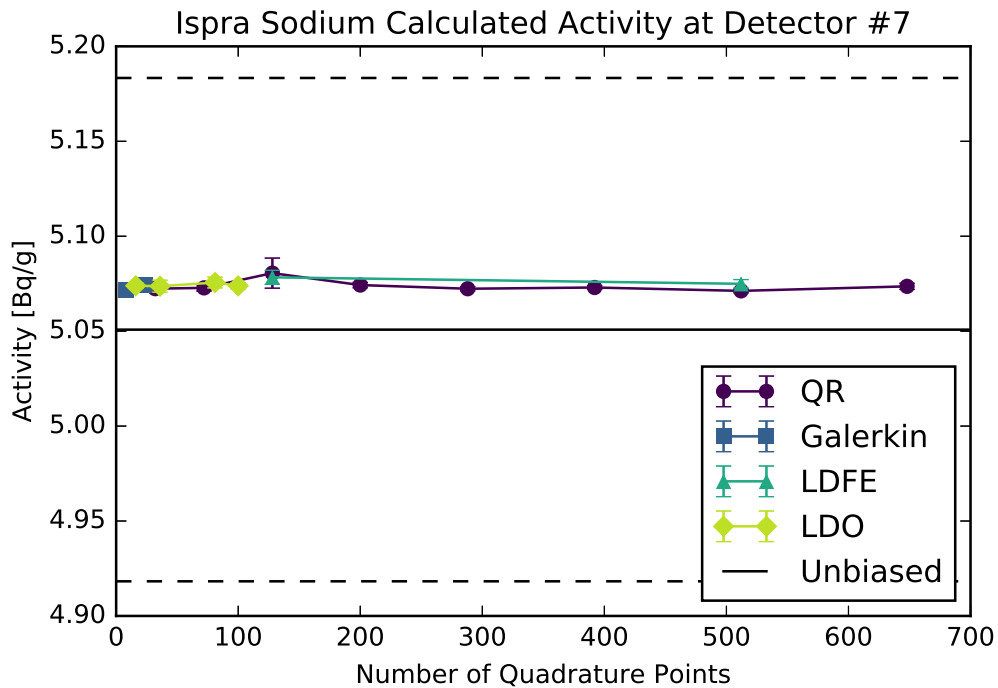


Figure 4.26: Ispra sodium calculated activity in the far detector with the CADIS method.

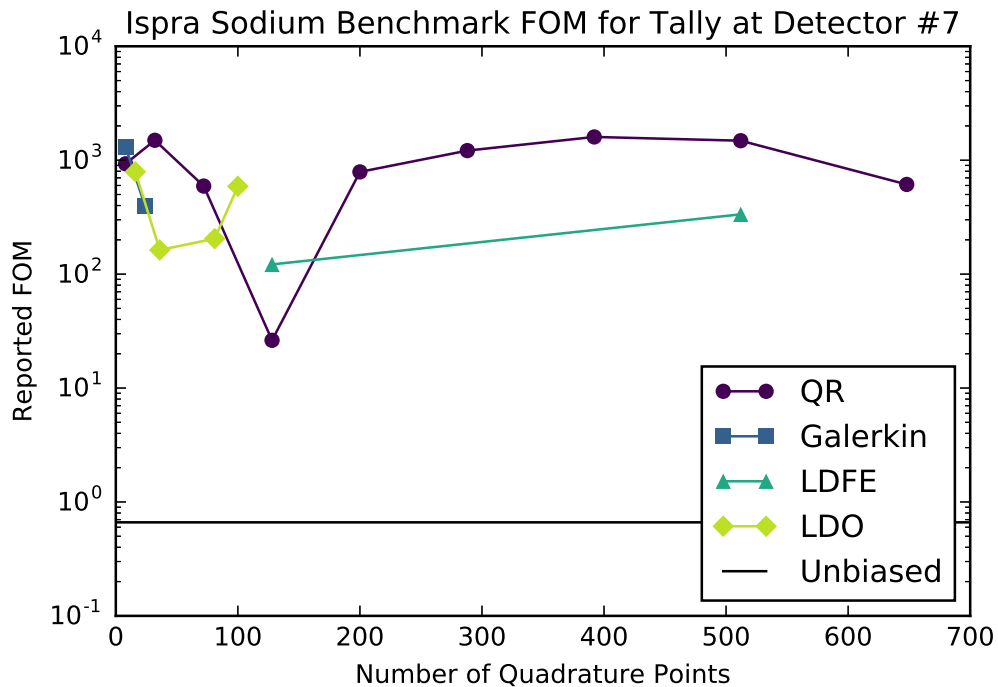


Figure 4.27: Ispra sodium far detector flux tally FOM values with the CADIS method.

4.3.4 Simplified Portal Monitor

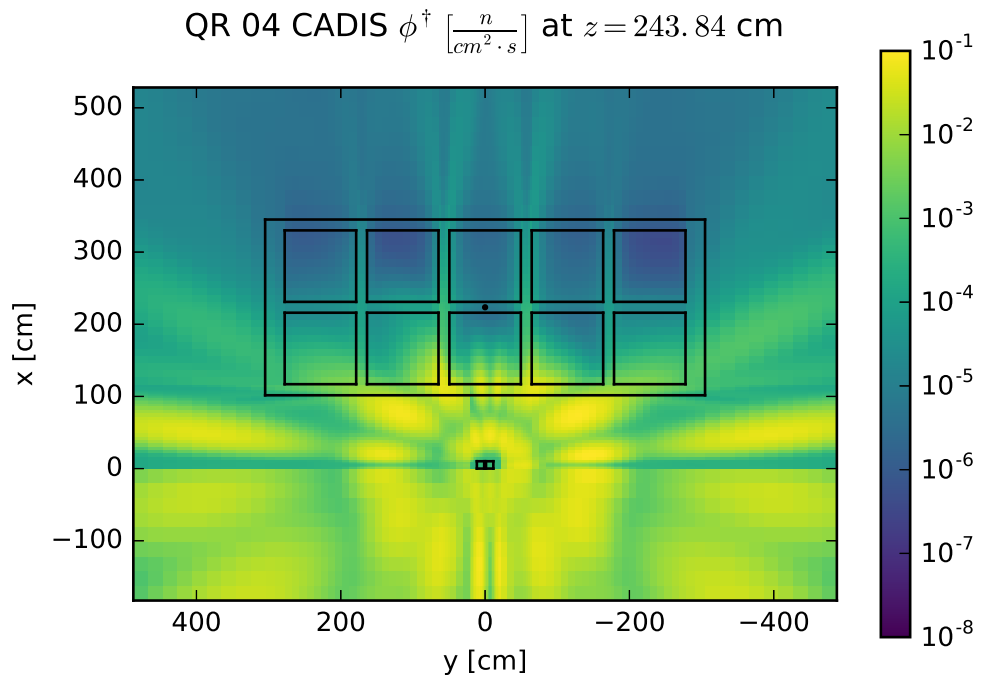
To study calculations for the simplified portal monitor scenario in the context of the CADIS method, the adjoint source was set to be the top detector in the small array. The adjoint scalar flux solutions are plotted in Figure 4.28. Ray effects appear drastically in all of the adjoint scalar flux solutions. Figure 4.28b shows regions where the adjoint scalar flux solution is negative for the representative Galerkin quadrature set; these regions are plotted in white. Because of these negative flux regions, Table 4.14 shows the extremal values of the magnitudes of the relative flux differences, calculated as

$$\phi_{\text{diff}} = \frac{|\phi_{\text{LDO}} - \phi_{\text{ref}}|}{|\phi_{\text{ref}}|}. \quad (4.3)$$

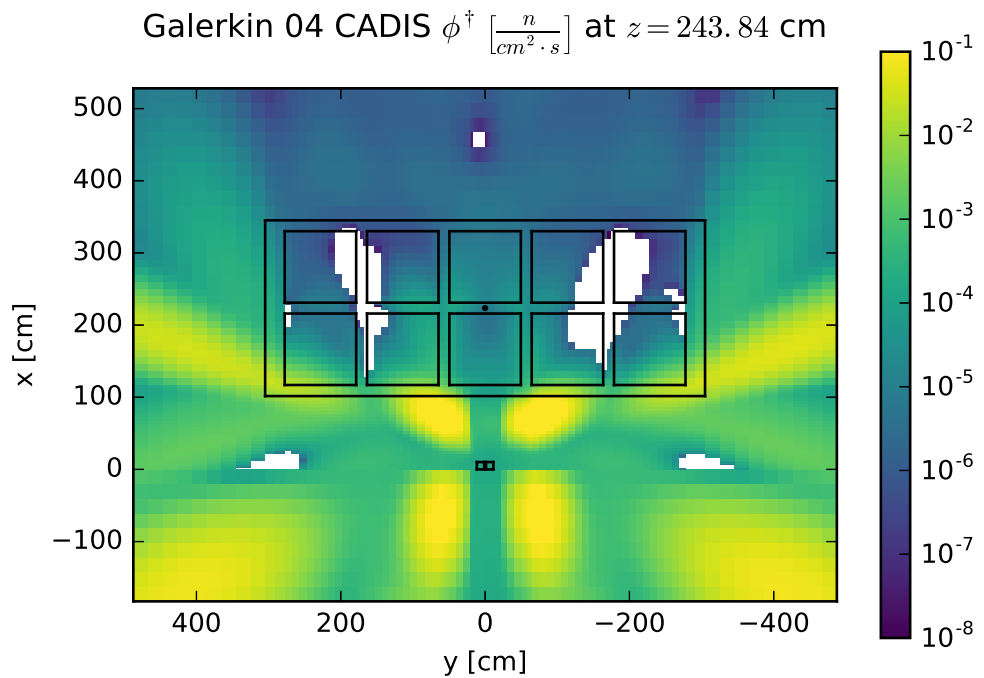
All of the flux solutions show poor agreement, likely because of the localized source and streaming paths created by this scenario's materials and geometry. Still, the LDO adjoint scalar flux solution agrees with the QR adjoint scalar flux solution better than the Galerkin or LDDE solutions, on average.

Table 4.14: Portal monitor CADIS adjoint scalar flux extremal and average relative differences.

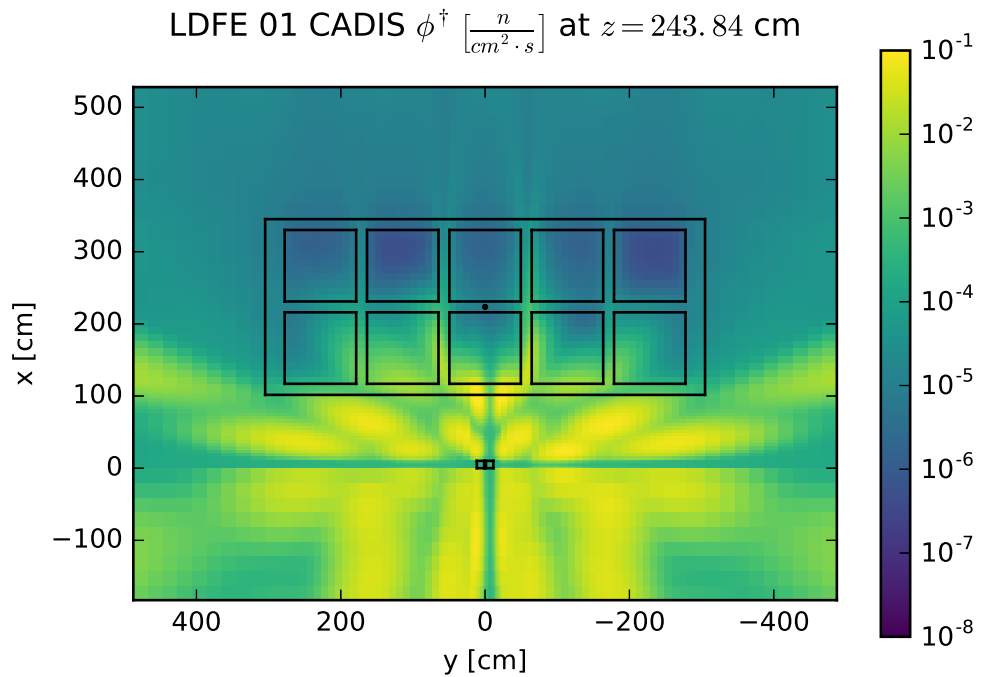
Comparison	Min. Diff.	Max. Diff.	Avg. Diff.
LDO/QR	2×10^{-4}	1.83×10^2	2.27×10^0
LDO/Galerkin	1×10^{-4}	6.20×10^4	4.29×10^1
LDO/LDDE	2×10^{-4}	2.54×10^2	3.46×10^0
Galerkin/QR	1×10^{-3}	2.59×10^2	3.81×10^0
LDDE/QR	6×10^{-5}	6.48×10^1	2.21×10^0



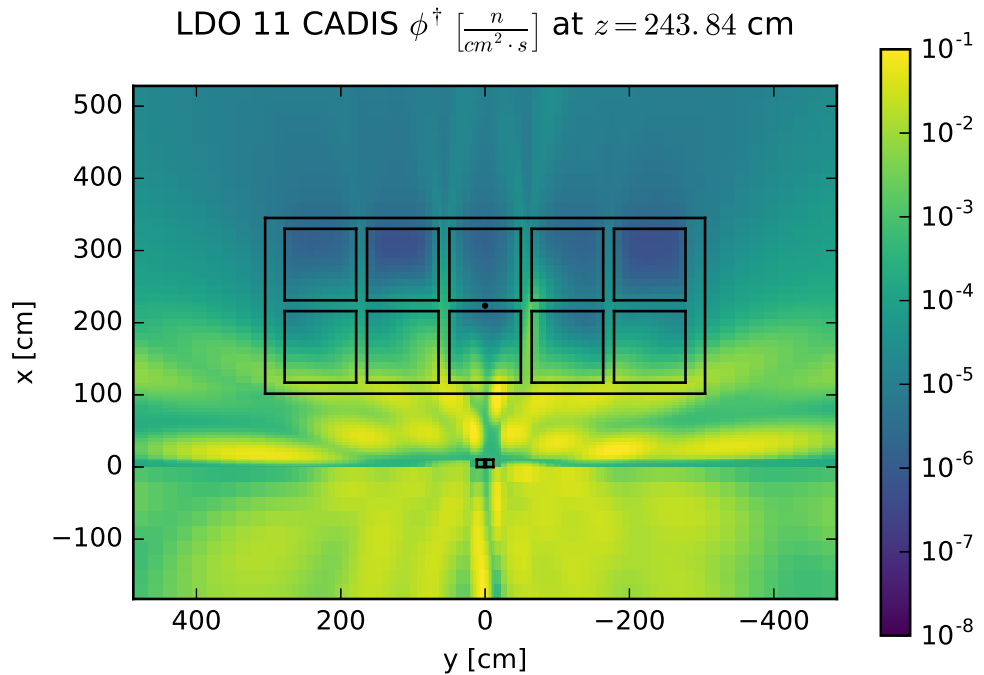
(a) QR adjoint flux slice.



(b) Galerkin adjoint flux slice.

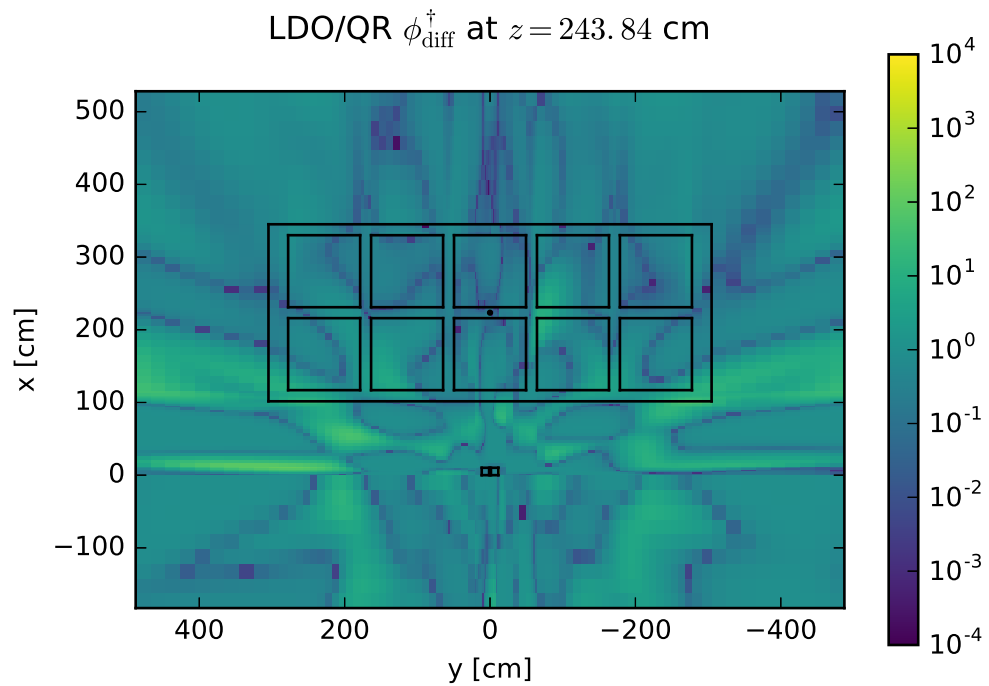


(c) LDFE adjoint flux slice.

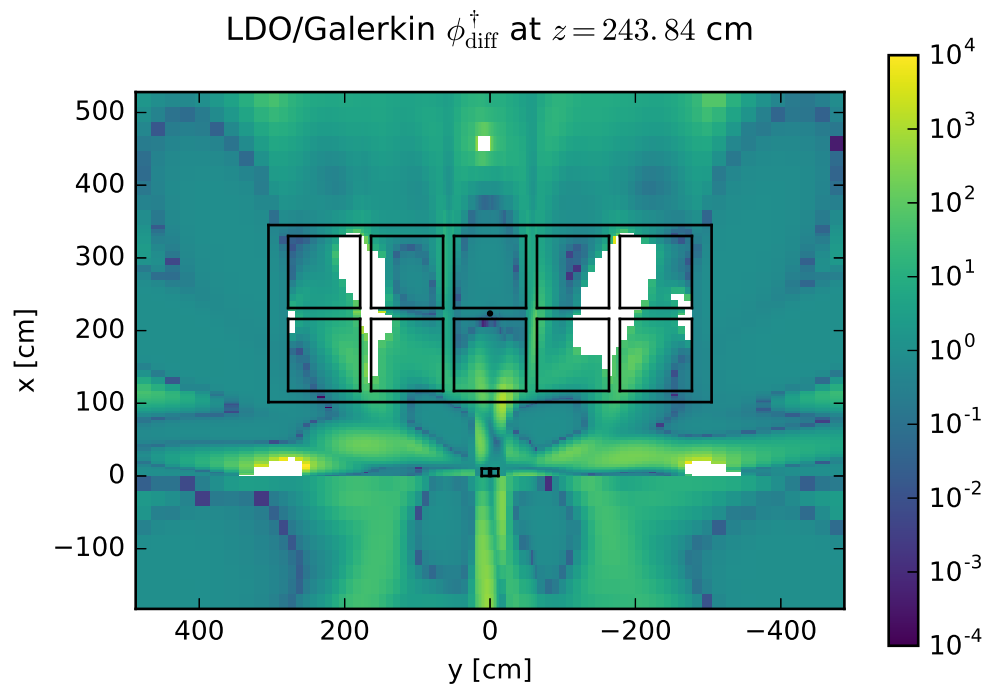


(d) LDO adjoint flux slice.

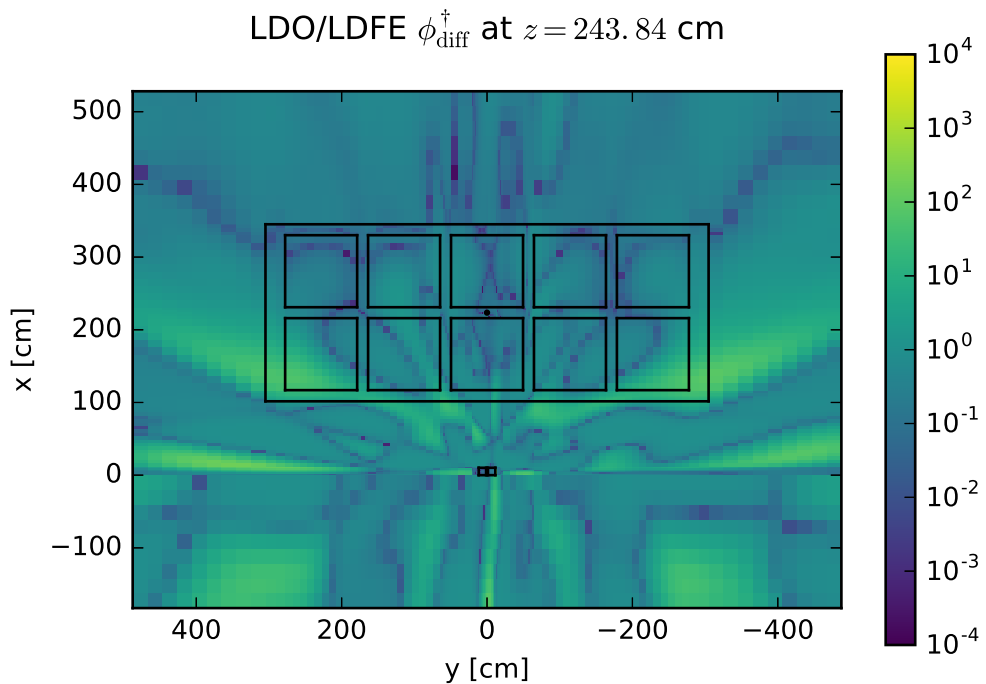
Figure 4.28: Simplified portal monitor adjoint scalar flux slices for the CADIS method.



(a) LDO/QR flux relative difference.



(b) LDO/Galerkin flux relative difference.



(c) LDO/LDFE flux relative difference.

Figure 4.29: Portal monitor adjoint scalar flux relative difference slices for the CADIS method.

Finally, we move on to the results and analysis of the Monte Carlo calculations, in which 1×10^9 particle histories were simulated. Again, since the CADIS adjoint source was set to be the top detector location, we focus the discussion in this section on the results for that specific location. Figures 4.30 and 4.31 show the MCNP-reported forward scalar flux tally values and Figures of Merit, respectively. As with the other test cases, the values are plotted as a function of the number of quadrature points used to generate the biasing parameters in order to explore the impact of angular mesh refinement on flux tally and FOM.

Similar to other test cases, the flux tally values reported in Figure 4.30 show a trend of converging to a stable value after the first few coarsest angular meshes. The flux tally values from the biased calculations all fall within the statistical error of that of the unbiased calculation but appear to require a minimum value of approximately 100 discrete angular values in order to stabilize. Figure 4.31 shows a strong correlation between the number of quadrature points and the flux tally FOM, eventually approaching an upper limit around 100. The LDO Figures of Merit increase most rapidly with the number of quadrature points used, so one would want to use a higher-order LDO quadrature set to generate Monte Carlo biasing parameters.

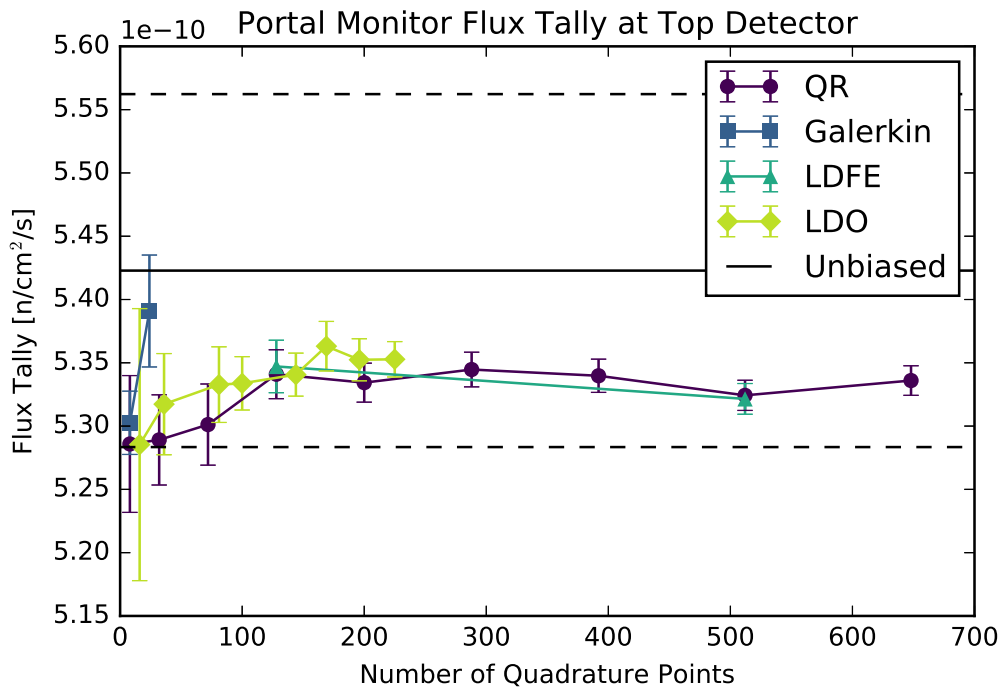


Figure 4.30: Flux tally in the portal monitor top detector using the CADIS method.

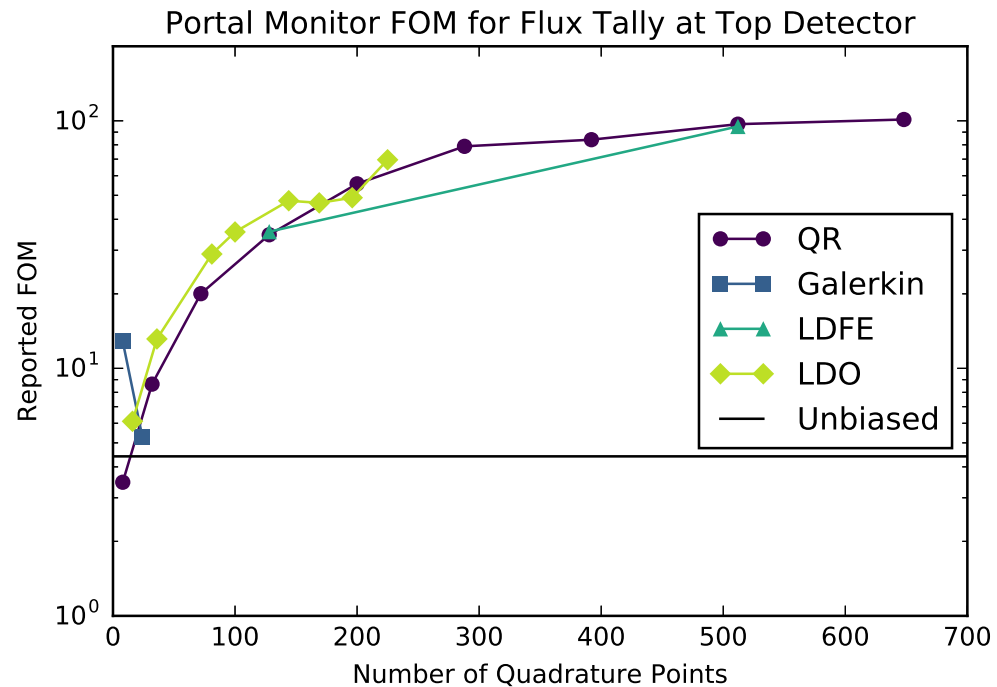


Figure 4.31: CADIS method FOM values for the portal monitor top detector flux tally.

4.3.5 Summary

In this section, we examined the deterministic and Monte Carlo results for the four test case scenarios in the context of the CADIS method. For all of the test cases, little correlation was noted between angular mesh refinement and MCNP-reported forward flux tally value beyond the suggestion to use at least 100 discrete angles for the simplified portal monitor scenario. The reported FOM values also exhibited minimal correlation with angular mesh refinement except in the case of the portal monitor scenario, where the flux tally FOM increased with angular mesh refinement while approaching an upper limit.

For the three test cases in which neutrons were transported, the LDO quadrature sets of lower orders (3 and 8) were the most effective of the LDO sets for both flux tally value and FOM achievement. That is, if one were interested in using an LDO quadrature set to generate Monte Carlo biasing parameters for a given neutron transport problem in the context of the CADIS method, we would suggest performing the deterministic calculation with an LDO quadrature set of order 8. For a photon transport problem considered in the CADIS context, we would suggest the finest available LDO quadrature set, based on the results seen here.

4.4 FW-CADIS Calculations

Finally, we examine the performance of the various quadrature types in the context of the FW-CADIS method. Similar to the analysis for the CADIS method, we will first look at the deterministic adjoint scalar flux solutions from the representative quadrature sets to compare the calculations using the LDO equations versus the standard quadrature types. Recalling Section 2.2.1.2, the FW-CADIS method incorporates both forward and adjoint scalar flux solutions. Because the adjoint source may be specified differently between the CADIS and FW-CADIS methods, it is instructive to look at the FW-CADIS deterministic adjoint scalar flux solutions. However, the deterministic forward flux solutions used in the FW-CADIS method are the same as those discussed in Section 4.2 and so we will not repeat the analysis here. Lastly, we again look at result metrics from the various Monte Carlo runs to compare the variance reduction parameter generation efficacy of the different quadrature types.

4.4.1 Steel Plate in Water

For the FW-CADIS calculations for the steel plate in water, the adjoint source was set to be a mesh tally over all of the air beyond the steel plate. The discretization for the adjoint source mesh tally is the same as that listed in Section 4.1.1. Specifically, the adjoint source mesh is identical to the overall problem mesh in the x - and y -directions but starts at $z = 130$ cm and extends to the problem boundary at $z = 140$ cm.

Figure 4.32 shows the adjoint scalar flux solutions for the representative quadrature sets for the steel plate embedded in water. As expected, in each solution, the adjoint flux is highest in the chosen adjoint source region for the problem and decreases logarithmically

in the z -direction. Table 4.15 lists the minimum, maximum, and average relative adjoint scalar flux solution differences for the comparisons plotted in Figure 4.33. As with earlier cases, the Galerkin/QR and LDFE/QR comparisons are also tabulated for reference. Like other deterministic flux comparisons for the steel plate embedded in water, the LDO flux solution best matches the QR flux solution, with an average relative difference of 4.6% for the FW-CADIS adjoint scalar flux.

Table 4.15: Steel plate FW-CADIS adjoint scalar flux extremal and average relative differences.

Comparison	Min. Diff.	Max. Diff.	Avg. Diff.
LDO/QR	2×10^{-4}	1.66×10^{-1}	4.63×10^{-2}
LDO/Galerkin	2×10^{-5}	1.85×10^0	7.16×10^{-1}
LDO/LDFE	8×10^{-2}	2.41×10^{-1}	1.92×10^{-1}
Galerkin/QR	5×10^{-4}	5.98×10^0	2.85×10^0
LDFE/QR	3×10^{-2}	3.37×10^{-1}	2.09×10^{-1}

Comparing Figure 4.33 with Figure 4.14, we see that the relative differences among the FW-CADIS adjoint scalar flux solutions are more uniform than those of the CADIS adjoint flux solutions. This is to be expected, as the CADIS adjoint source is much more localized than the FW-CADIS for the steel plate scenario studies conducted here.

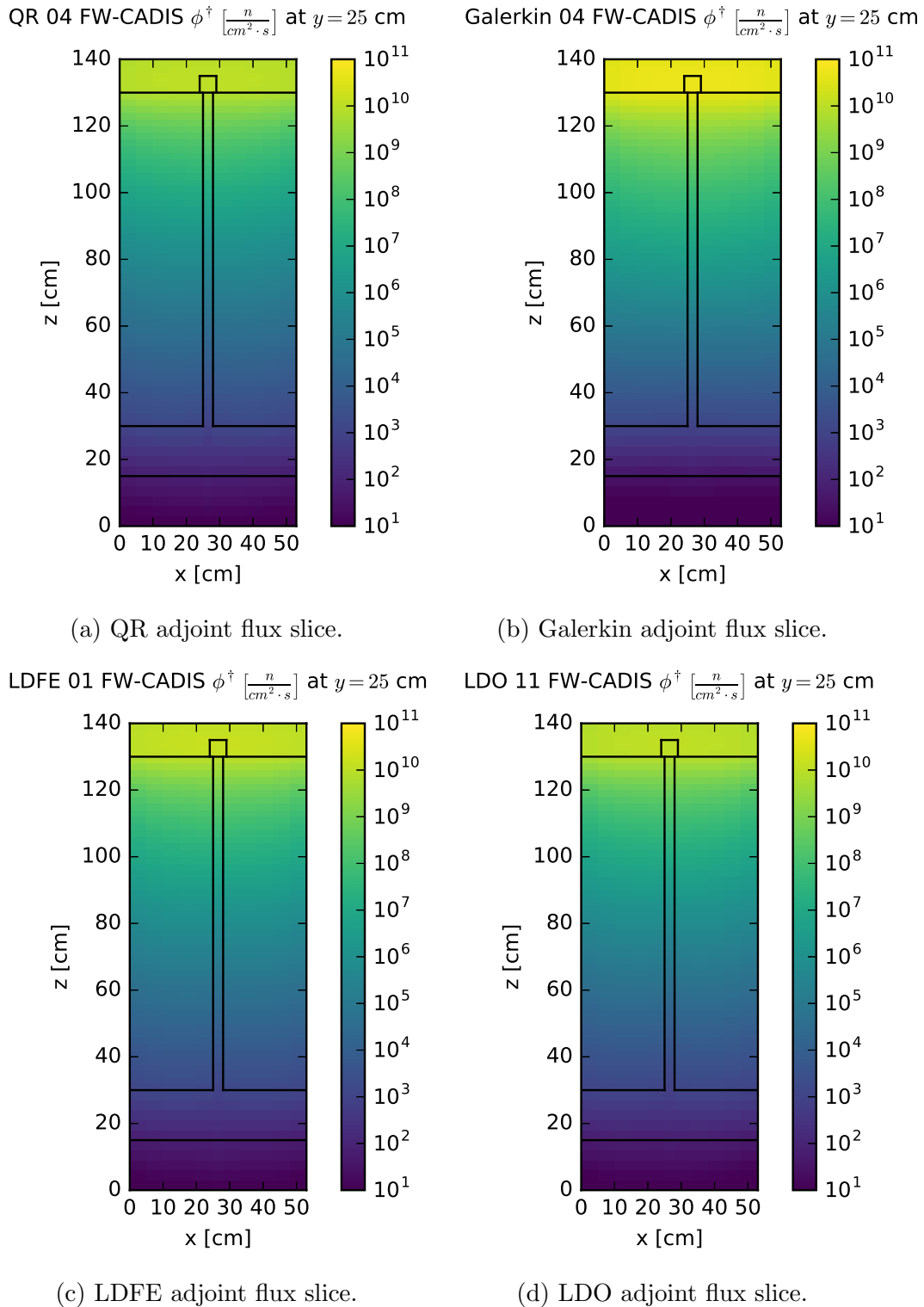


Figure 4.32: Steel plate adjoint scalar flux slices for the FW-CADIS method.

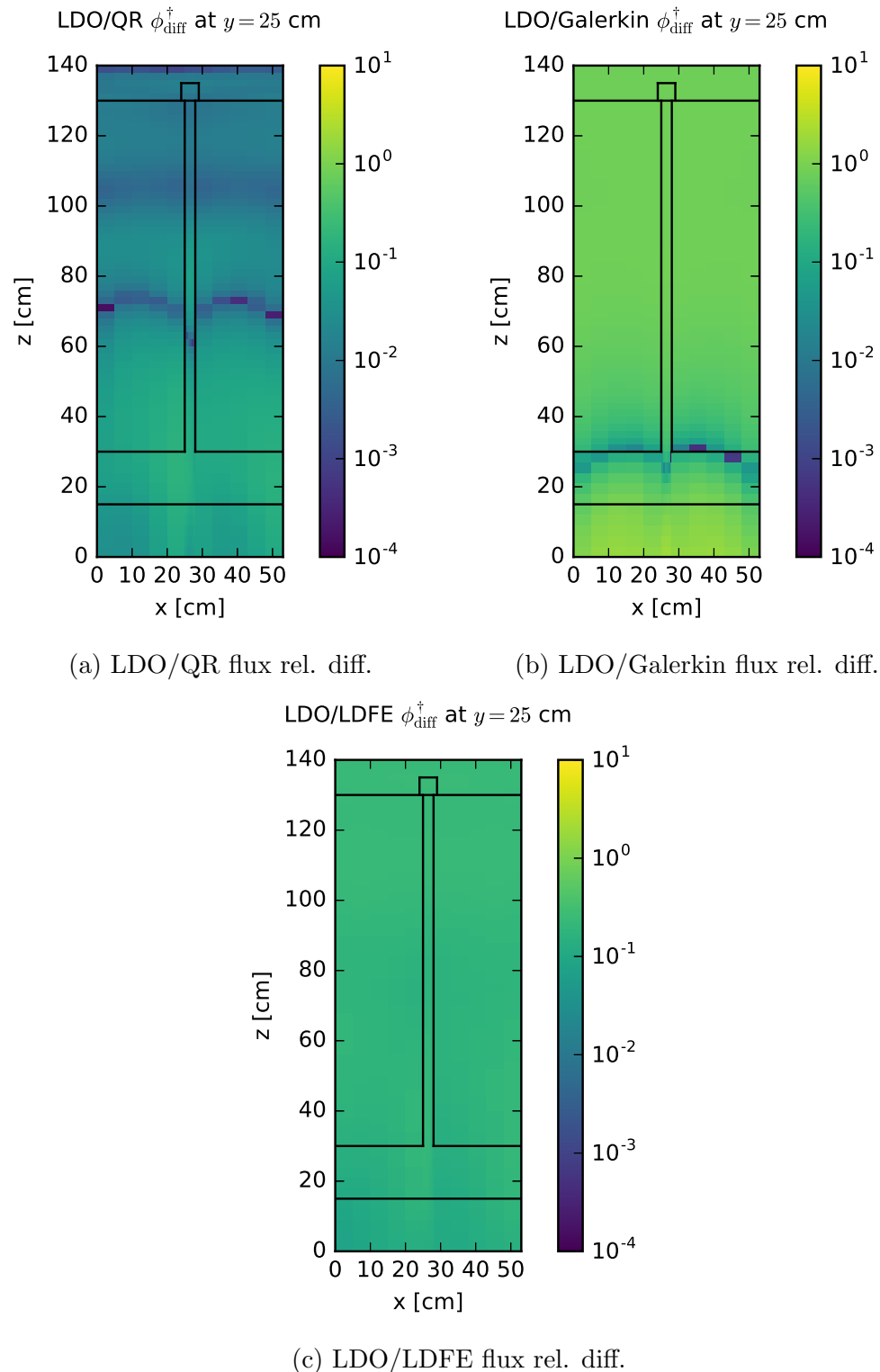


Figure 4.33: Steel plate adjoint flux relative difference slices for the FW-CADIS method.

Next, we will look at the results for the mesh tally in the air region of the scenario. The Monte Carlo run with biasing parameters from the Galerkin quadrature set of order 2 was not able to finish in a timely manner for the hardware configuration used in this work, so Monte Carlo results for this data point are not included here. The calculations for this test case scenario used 1×10^9 neutron histories.

Figure 4.34 shows the total tally summed over all air in the problem for the biased and unbiased calculations. The biased calculations are plotted as a function of angular mesh refinement and the unbiased calculation value is shown as a black horizontal line. Like the CADIS method, the FW-CADIS method generates biasing parameters such that the biased Monte Carlo flux tally results all fall far below that of the unbiased calculation. Similarly, in this case, the angular mesh refinement has little impact on the tally result. So, if using an LDO quadrature set to generate biasing parameters with the FW-CADIS method in a similar scenario, a low-order LDO angular mesh could be used to good effect.

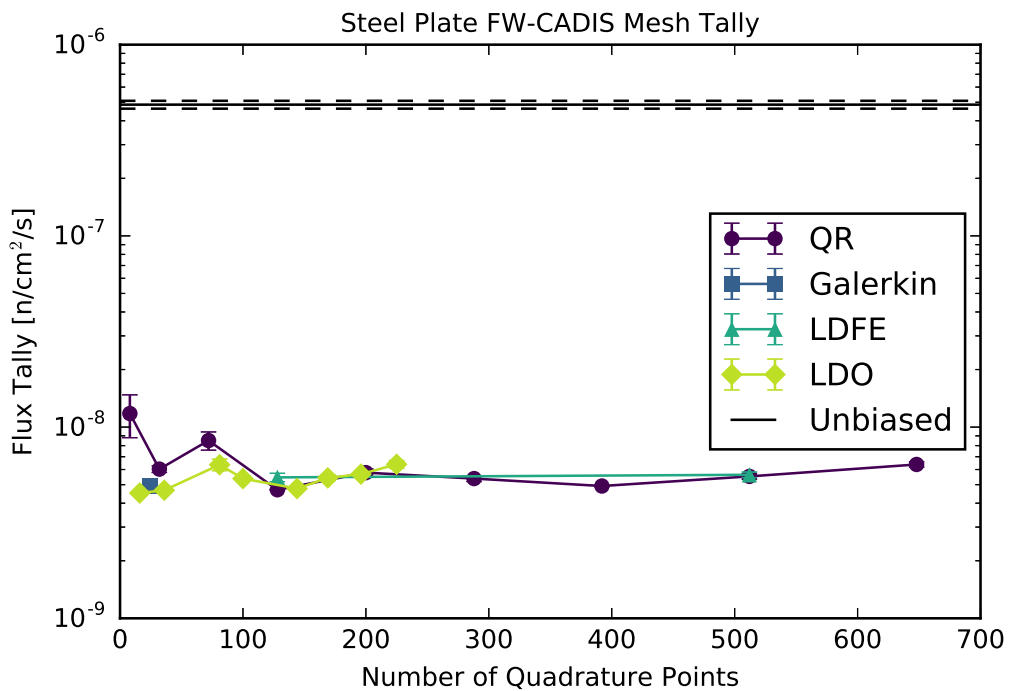


Figure 4.34: Flux tally over the air region in the steel plate test with the FW-CADIS method.

To analyze the performance of the representative quadrature sets' variance reduction parameters for the steel plate in water case using the FW-CADIS method, we will look at the average FOM values over the entire adjoint source mesh tally. The Figures of Merit were calculated by taking the average relative error over all spatial cells in the air block mesh tally and using that mean value in combination with the MCNP-reported computer time and Equation 2.10. Figure 4.35 shows these average Figures of Merit as a function of

the number of angles used in generating the biasing parameters. The average FOM for the unbiased calculation is shown as a horizontal black line.

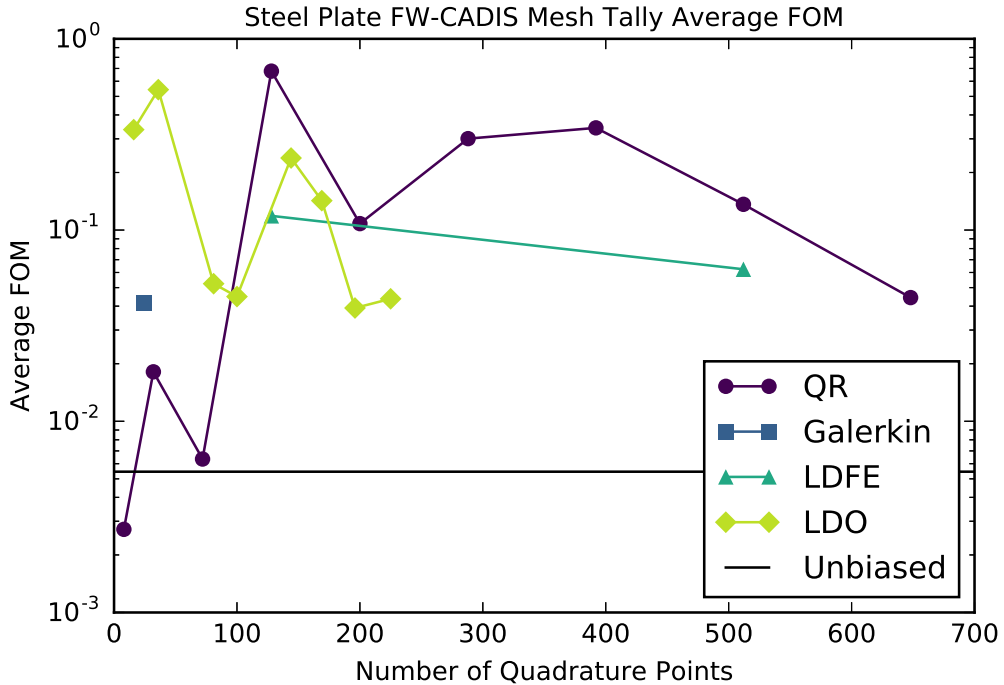


Figure 4.35: Average FOM values for the mesh tally in the FW-CADIS steel plate scenario.

We see a different trend here in that the highest average FOM values tend to come from quadrature sets with mid-range angular mesh refinement; the coarsest and finest angular meshes produce Monte Carlo biasing parameters that result in reduced Figures of Merit. Considering Figures 4.34 and 4.35, we note that one would wish to use a lower-order (e.g., order 5) LDO quadrature set to generate variance reduction parameters for a Monte Carlo mesh tally using the FW-CADIS method.

4.4.2 DLVN

Considering the DLVN case with the FW-CADIS method, the adjoint source was specified to be the combination of all of the detector locations in the problem. In accordance with this, the adjoint scalar flux solutions shown in Figure 4.36 demonstrate the highest source values in the region where four out of the six detector locations are concentrated. Figure 4.37 displays the relative differences between the LDO adjoint scalar flux solution and those of the three standard quadrature types with extremal and average relative difference values listed in Table 4.16. Of the standard quadrature types, the LDO adjoint flux solution differs the least from the QR adjoint flux solution, with an average relative difference of about 11% for this FW-CADIS adjoint source specification for the DLVN problem. Given the

more spatially generalized source specification, it is unsurprising to see uniform differences in Figures 4.37a and 4.37c. The nonuniform differences in Figure 4.37b may be attributed to the relative coarseness of the representative Galerkin quadrature set.

Table 4.16: DLVN FW-CADIS adjoint scalar flux extremal and average relative differences.

Comparison	Min. Diff.	Max. Diff.	Avg. Diff.
LDO/QR	1×10^{-3}	4.32×10^{-1}	1.12×10^{-1}
LDO/Galerkin	2×10^{-5}	1.90×10^0	1.79×10^{-1}
LDO/LDFE	1×10^{-2}	3.97×10^{-1}	1.73×10^{-1}
Galerkin/QR	2×10^{-4}	6.88×10^{-1}	2.68×10^{-1}
LDFE/QR	4×10^{-4}	2.58×10^{-1}	5.42×10^{-2}

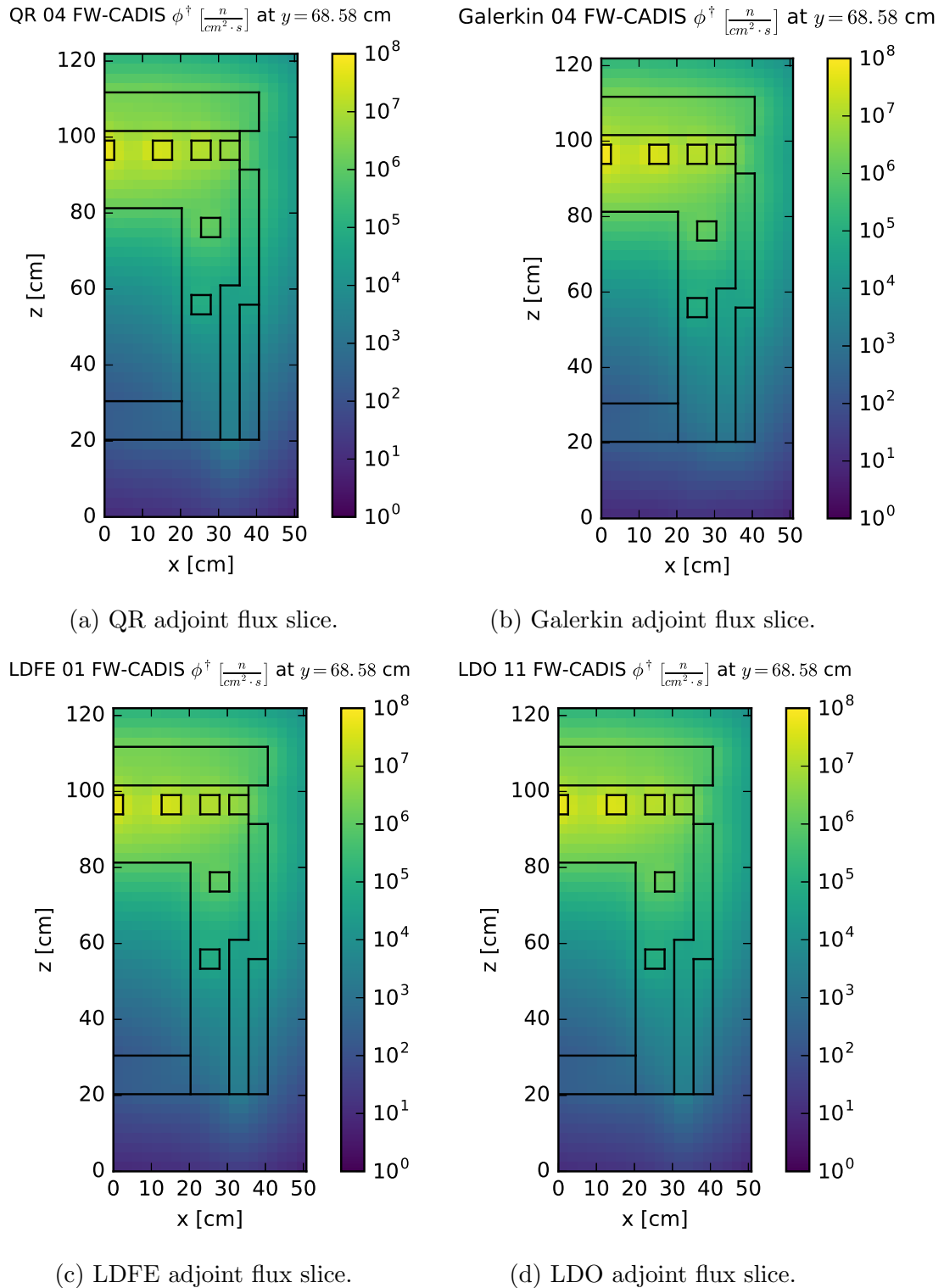


Figure 4.36: DLVN adjoint scalar flux slices for the FW-CADIS method.

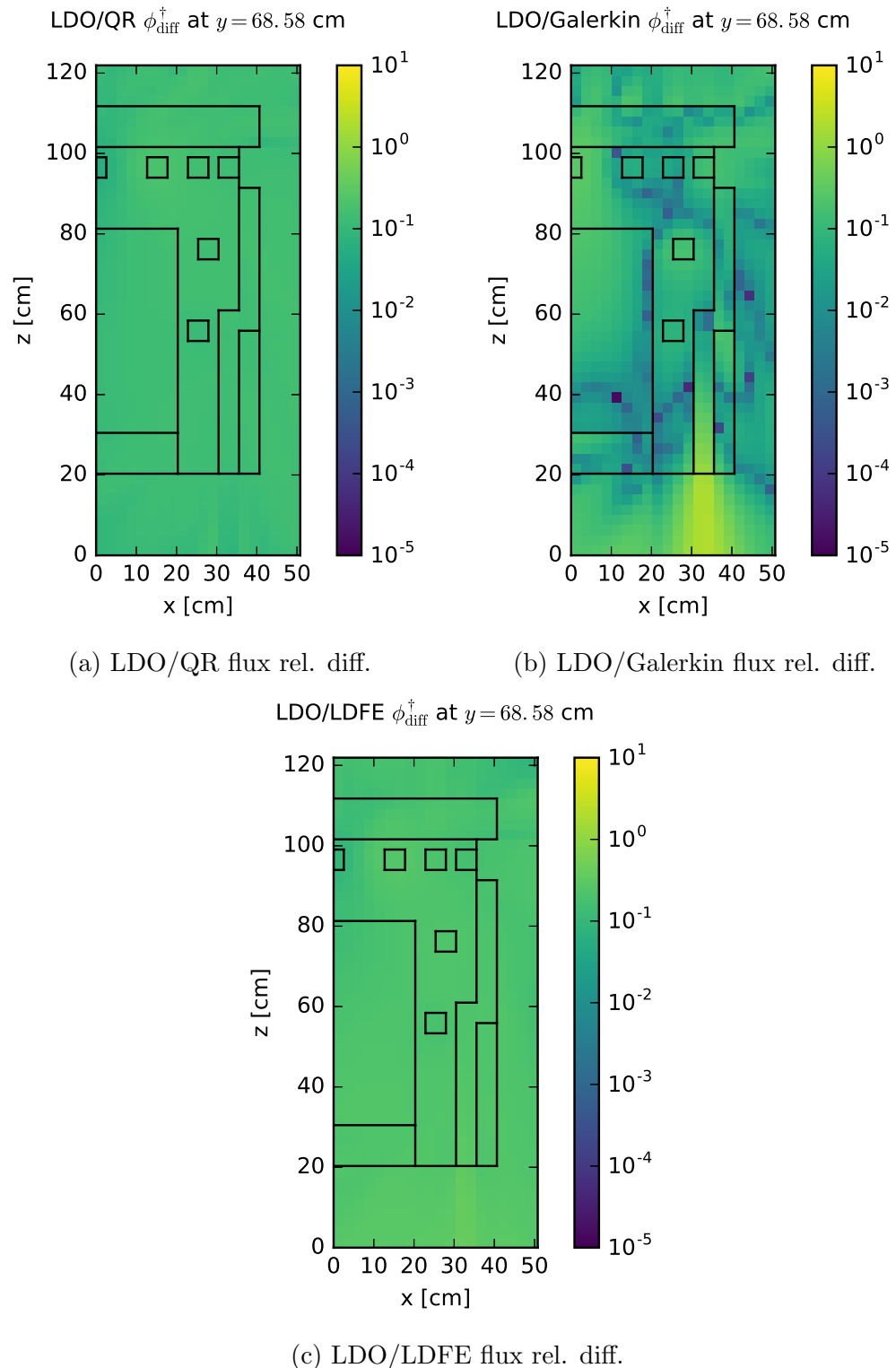


Figure 4.37: DLVN adjoint scalar flux relative difference slices for the FW-CADIS method.

Moving on to the Monte Carlo results and analysis, we look at the flux tallies and Figures of Merit for all of the detector locations in the DLVN experimental benchmark. Recall that 1×10^{10} particle histories were simulated. Figure 4.38 shows all of the detector locations' MCNP-reported forward scalar flux tallies plotted as a function of angular mesh refinement used to generate biasing parameters in addition to the Figures of Merit for the flux tallies. In each plot, the unbiased flux tally result is shown as a horizontal black line.

Figures 4.38a and 4.38b exhibit the same lack of trend in flux tally as a function of angular mesh refinement. That is, in general, for detector locations #5 and #9, using more discrete angles in the FW-CADIS deterministic calculations does not greatly impact the flux tally result from MCNP. Figures 4.38e and 4.38f show similar behavior with the exception of the most coarse angular meshes. For these detector locations, any angular mesh refinement other than the coarsest angular mesh will produce a consistent forward scalar flux tally result. Figures 4.38c and 4.38d show slightly more variation in flux tally result with angular mesh refinement. These two detector locations' tallies have also higher statistical error relative to those at the other detector locations. Overall, though, the flux tallies at detectors #11 and #12 are not heavily impacted by the refinement of the angular mesh used in generating the Monte Carlo biasing parameters, but a mid-range number of quadrature points should be used to avoid the large statistical errors seen at the extreme ends of the angular mesh refinement spectrum.

Like their corresponding flux tally graphs, Figures 4.38a, 4.38b, and 4.38e show almost no variation in FOM with angular mesh refinement for the tallies at detector locations #5, #9, and #13. This is to be expected, considering the uniform statistical error and stable flux tally results at these locations. Figure 4.38c shows variation in FOM with angular mesh refinement that is more varied, which corresponds to the larger statistical uncertainties in the flux tally values for detector #11. Figure 4.38d shows little variation in FOM with angular mesh refinement with the exception of the finest QR set. Lastly, 4.38f shows an upper FOM limit of approximately 200 across all quadrature types, with the Figure of Merit largely consistent across quadrature types with the exception of QR angular meshes.

In Table 4.17 we compare the Monte Carlo forward flux tally results for the representative quadrature sets listed in Section 4.1.5.1. Results from the unbiased Monte Carlo calculation are also included for comparison. All Monte Carlo flux tally values are reported with an uncertainty of one standard deviation. For all detector locations, the Monte Carlo flux tallies do not match the experimentally measured flux values for any of the representative quadrature sets or the unbiased calculation, so we only compare the Monte Carlo calculations in this table. We do note that the Monte Carlo calculations overestimate the flux tally at all detector locations with the exception of detector #13. The flux tallies at detectors 5, 9, 13, and 14 all match within statistical uncertainty for all of the Monte Carlo calculations. At detector #11, the biased Monte Carlo calculations match within standard error, but the calculations using the QR and LDO biasing parameter fall outside of the error bounds of the unbiased calculation. Somewhat similarly, at detector #14, all of the biased calculations match one another within statistical uncertainty, but they are all outside of the error bounds of the unbiased flux tally calculation.

Table 4.17: DLVN benchmark flux tallies [n/cm²/s] calculated with FW-CADIS.

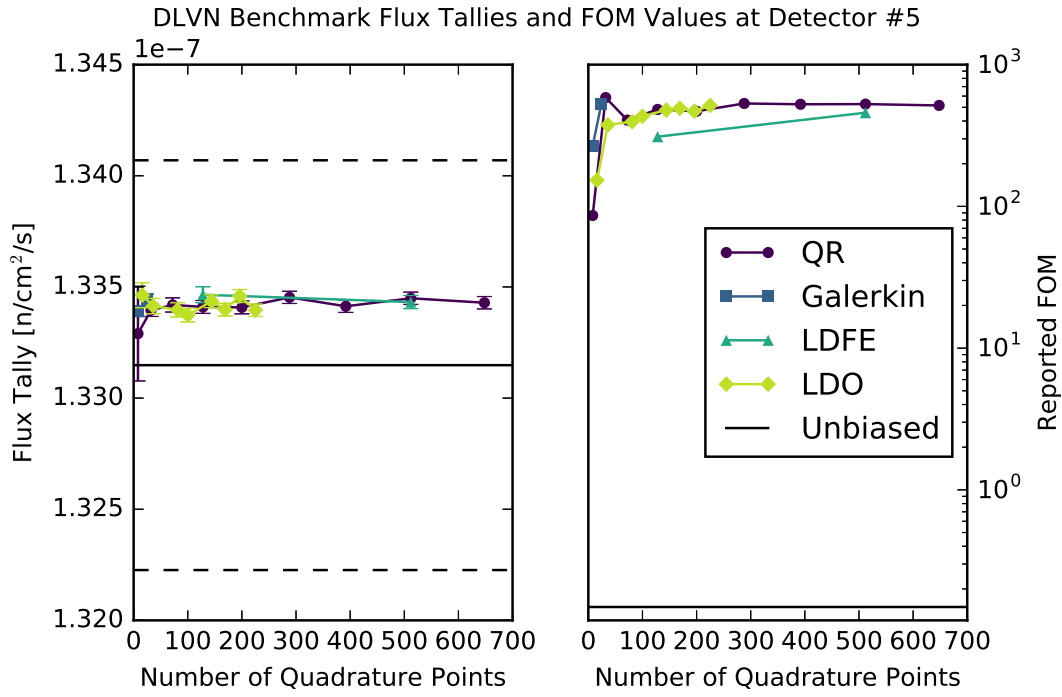
	QR	Galerkin	LDFE	LDO	Unbiased
Det. #5 ($\times 10^{-7}$)	1.3341 \pm 0.0003	1.3344 \pm 0.0003	1.3347 \pm 0.0004	1.3344 \pm 0.0003	1.3315 \pm 0.0092
Det. #9 ($\times 10^{-7}$)	2.5225 \pm 0.0005	2.5224 \pm 0.0005	2.5229 \pm 0.0004	2.2555 \pm 0.0004	2.5104 \pm 0.0127
Det. #11 ($\times 10^{-5}$)	1.4420 \pm 0.0005	1.4451 \pm 0.0027	1.4446 \pm 0.0026	1.4463 \pm 0.0015	1.4463 \pm 0.0010
Det. #12 ($\times 10^{-6}$)	2.4749 \pm 0.0004	2.4743 \pm 0.0004	2.4751 \pm 0.0004	2.4744 \pm 0.0004	2.4684 \pm 0.0042
Det. #13 ($\times 10^{-7}$)	4.3984 \pm 0.0011	4.3997 \pm 0.0011	4.3994 \pm 0.0011	4.3983 \pm 0.0011	4.4170 \pm 0.0175
Det. #14 ($\times 10^{-7}$)	7.0070 \pm 0.0025	7.0829 \pm 0.0045	7.0813 \pm 0.0026	7.0834 \pm 0.0032	7.0694 \pm 0.0216

To examine the FOM values in a more quantifiable way, Table 4.18 lists the FOM values for all detector locations for each of the representative quadrature sets as well as the unbiased calculation. The maximum FOM value at each detector location is emphasized. Of the six detector locations, the LDO quadrature set achieves the highest FOM for two of the locations. The QR quadrature set is the only other type to also deliver the highest FOM for two out of six detectors; the Galerkin and LDFE quadrature set biasing parameters each only achieve the highest FOM at one detector. So, the LDO quadrature set's biasing parameters perform comparably to those from the QR quadrature set with respect to obtaining high FOM values for multiple detector locations using the FW-CADIS method for the DLVN problem.

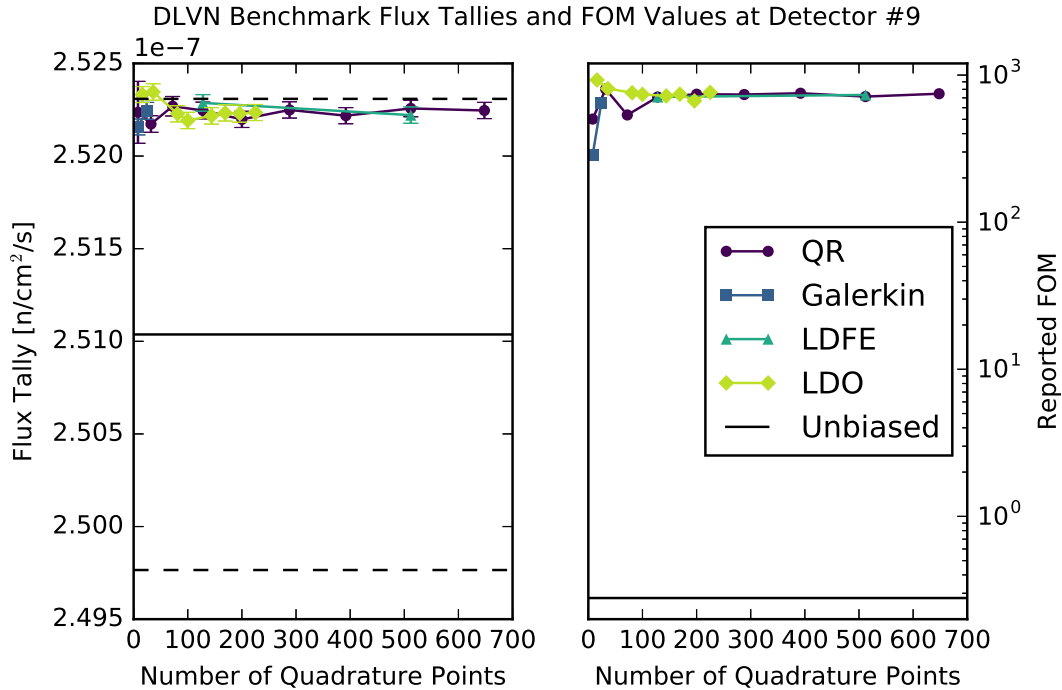
Table 4.18: FW-CADIS FOM values for representative quadratures for the DLVN problem.

Quad.	Type	Det. #5	Det. #9	Det. #11	Det. #12	Det. #13	Det. #14
QR		483.01	709.51	202.66	747.91	380.84	185.40
Galerkin		527.79	649.88	5.9934	798.88	326.11	52.098
LDFE		310.28	710.43	6.6749	926.28	391.62	166.51
LDO		478.24	721.22	19.959	943.96	369.42	110.40
Unbiased		0.14912	0.27845	14.555	2.5256	0.45376	0.76362

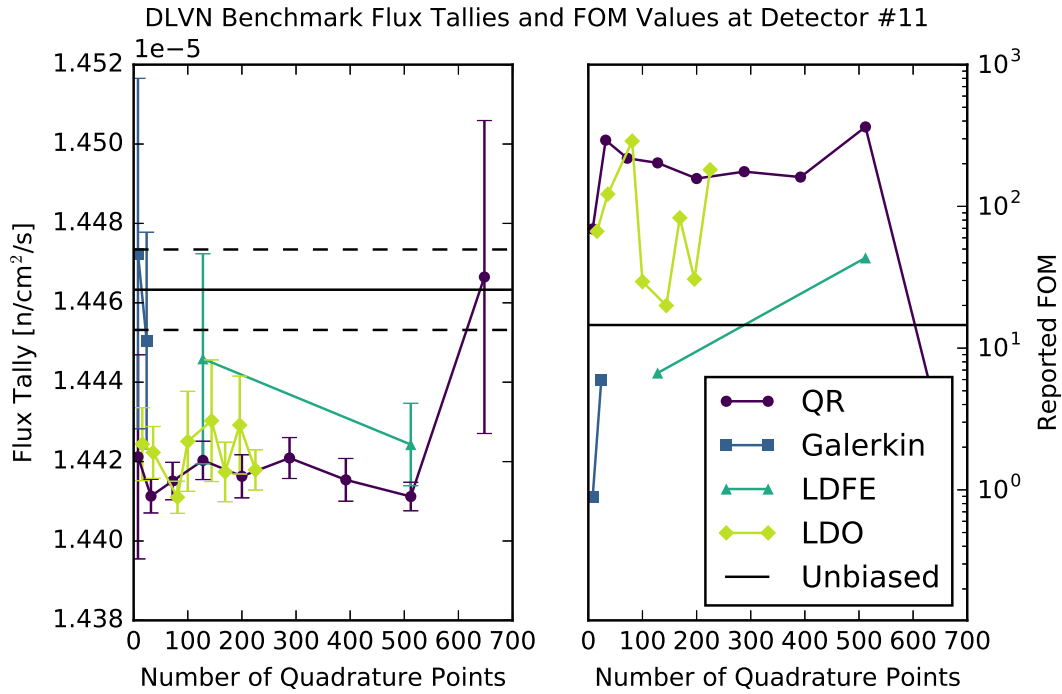
In summary, for test case scenarios such as the DLVN problem in which the FW-CADIS method is used to generate Monte Carlo variance reduction parameters to optimize the response at multiple flux tally detector locations, a relatively coarse quadrature set of any of the types studied here can be used to sufficient effect. However, the coarsest available quadrature sets should be avoided; flux tally results and Figures of Merit for the various detector locations tend to level out as a function of angular mesh refinement beyond the quadrature sets with the fewest number of angles. In particular, if using an LDO quadrature set in another similar scenario, we would suggest using a point set of order 5 or 8.



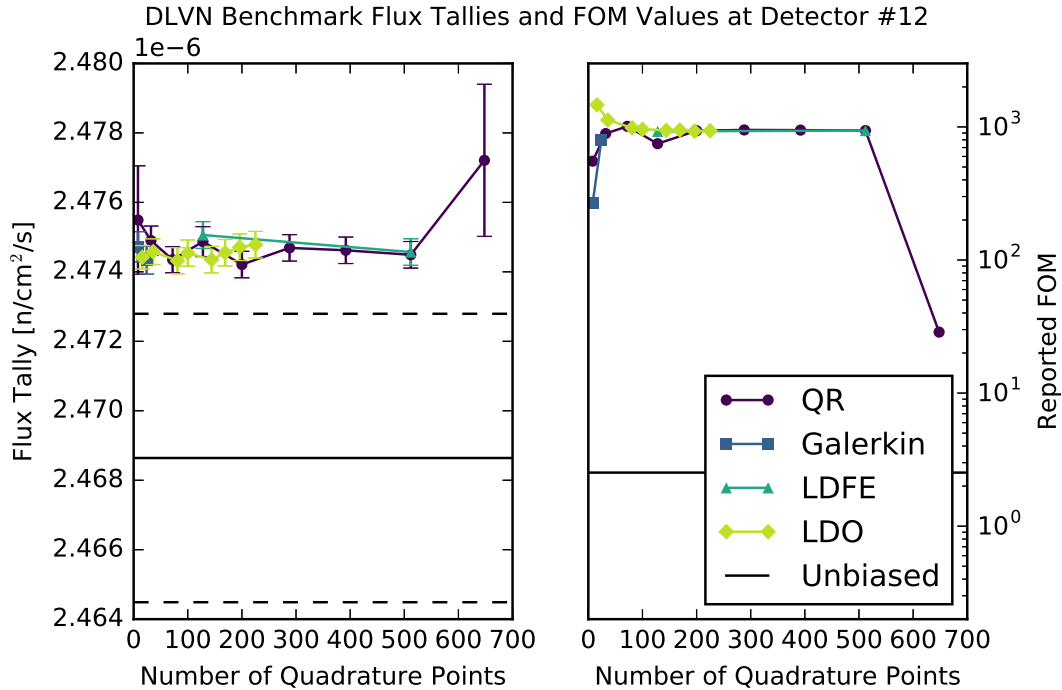
(a) MCNP-reported forward flux tally and FOM values at detector #5.



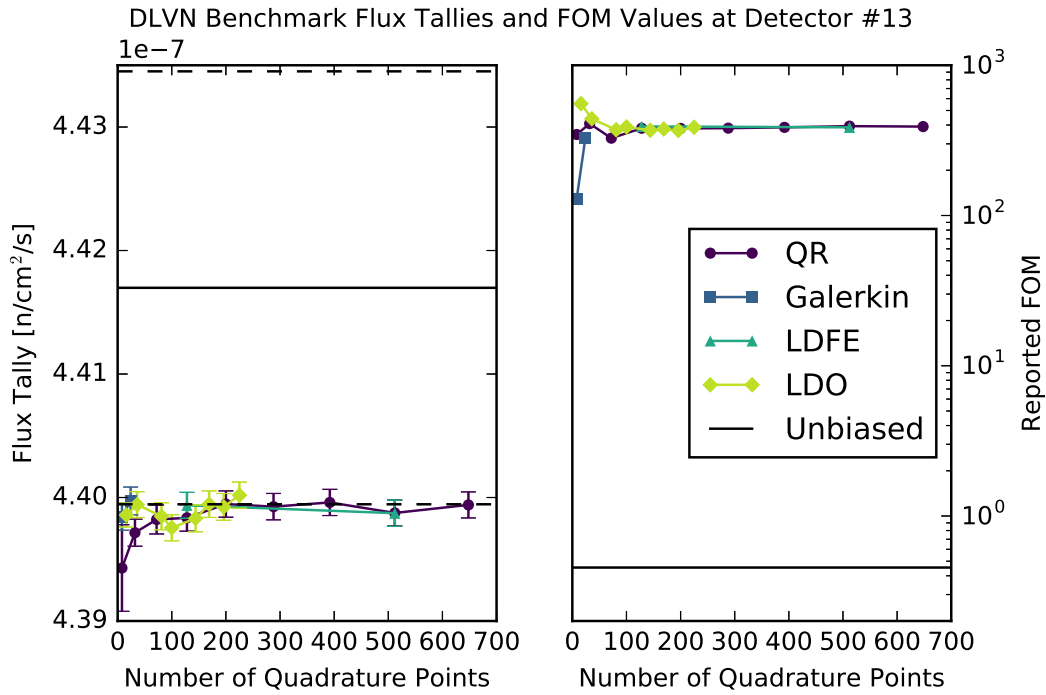
(b) MCNP-reported forward flux tally and FOM values at detector #9.



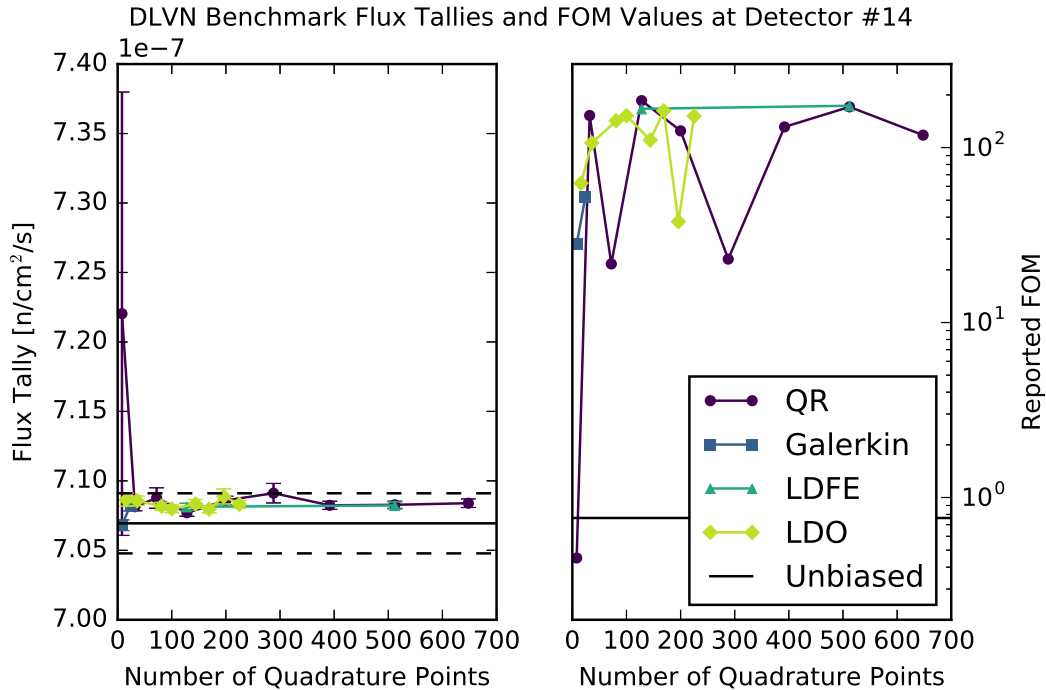
(c) MCNP-reported forward flux tally and FOM values at detector #11.



(d) MCNP-reported forward flux tally and FOM values at detector #12.



(e) MCNP-reported forward flux tally and FOM values at detector #13.



(f) MCNP-reported forward flux tally and FOM values at detector #14.

Figure 4.38: FW-CADIS flux tallies and FOM values for the DLVN problem.

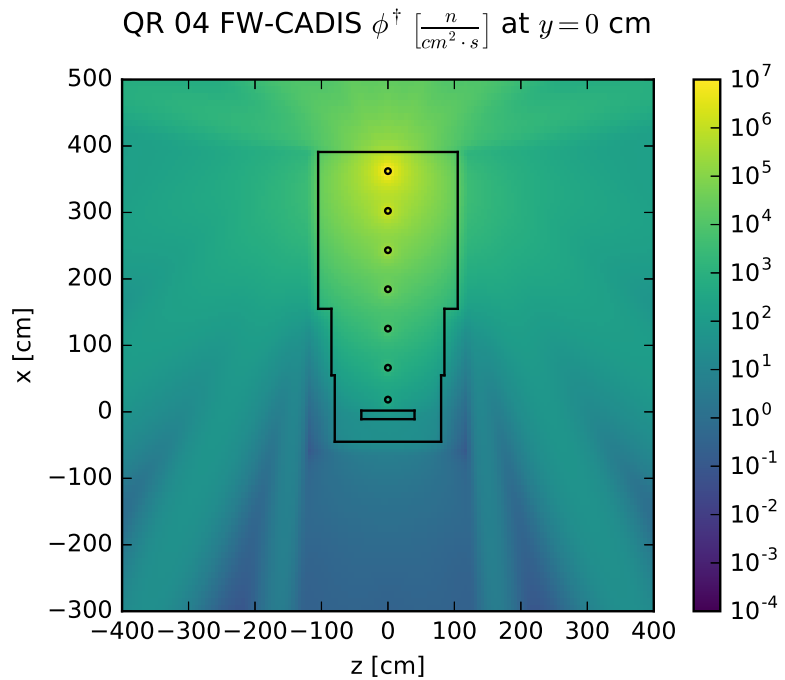
4.4.3 Ispra Sodium Benchmark

As in the previous case, the adjoint source for the Ispra sodium benchmark problem in the context of the FW-CADIS method was specified to be the combination of all of the detector locations in the problem. Figure 4.39 shows the adjoint scalar flux solutions for the representative quadrature sets based on this specification. Relative differences between the representative LDO adjoint scalar flux and the standard quadratures' adjoint scalar fluxes are shown in Figure 4.40 with minimum, maximum, and average relative differences listed in Table 4.19. Again, comparisons of the QR flux solution against the Galerkin and LDDE flux solutions are tabulated for reference as well.

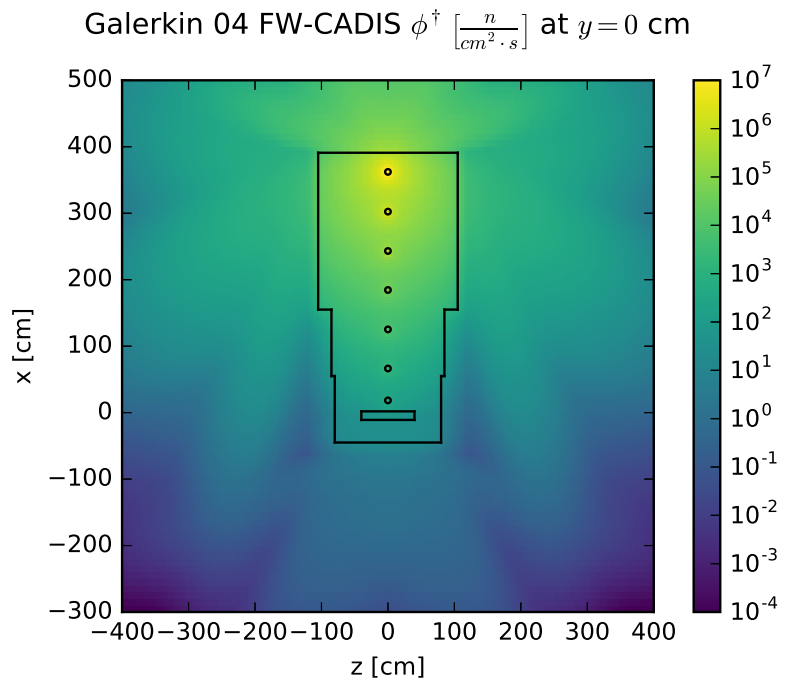
Table 4.19: Ispra sodium FW-CADIS adjoint flux extremal and average relative differences.

Comparison	Min. Diff.	Max. Diff.	Avg. Diff.
LDO/QR	2×10^{-6}	4.40×10^1	5.93×10^{-1}
LDO/Galerkin	6×10^{-7}	4.45×10^4	1.63×10^2
LDO/LDDE	1×10^{-6}	1.30×10^2	7.42×10^{-1}
Galerkin/QR	2×10^{-6}	1.00×10^0	4.42×10^{-1}
LDDE/QR	3×10^{-6}	5.05×10^1	8.00×10^{-1}

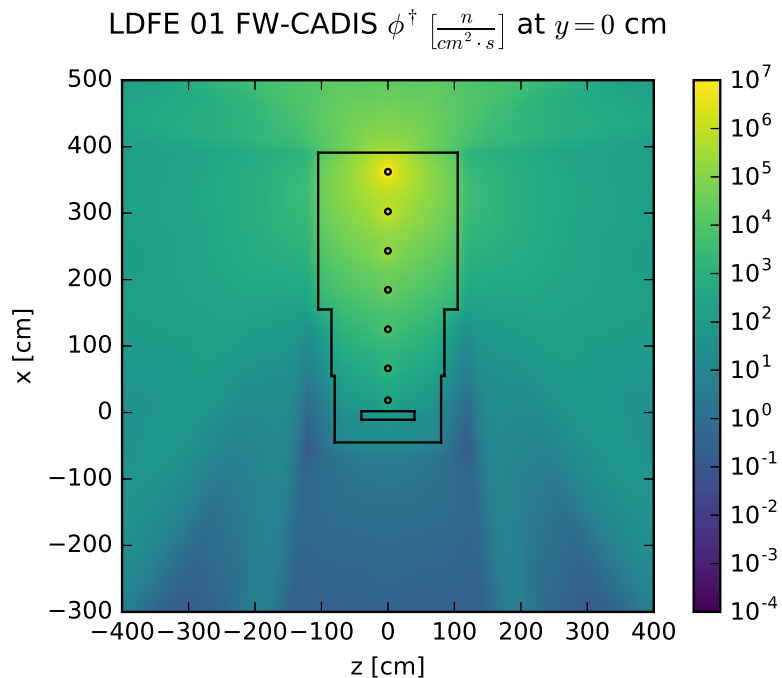
Comparing these differences to the values listed in Table 4.13, we see that the LDO adjoint flux matches those of the standard quadratures more closely on average in the FW-CADIS method than the CADIS method. This is to be expected, as the adjoint source in the FW-CADIS method is much less localized than in the CADIS method for this scenario. As with the forward and CADIS adjoint flux comparisons for the Ispra sodium benchmark, the differences between the representative LDO flux solution and the representative standard quadratures' flux solutions are exacerbated by the relatively coarse LDO angular mesh.



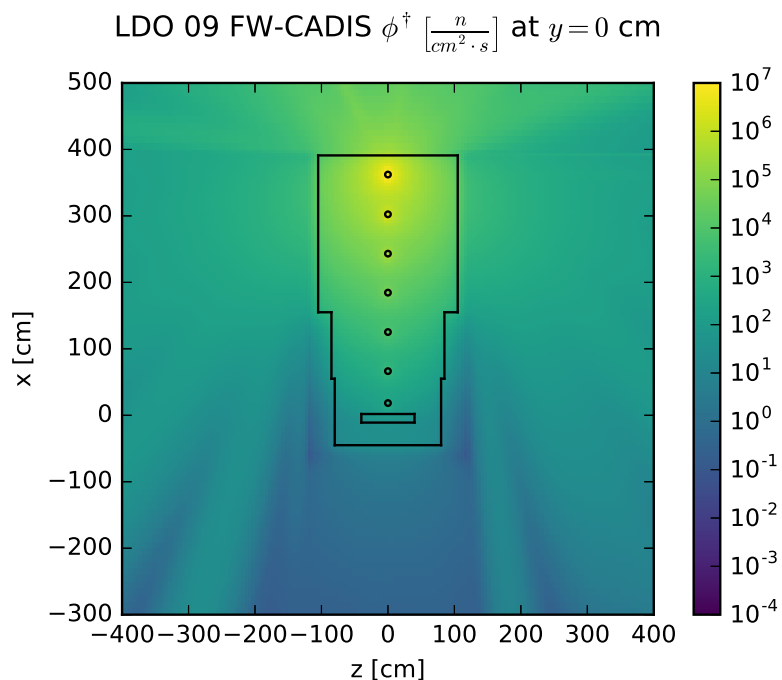
(a) QR adjoint flux slice.



(b) Galerkin adjoint flux slice.

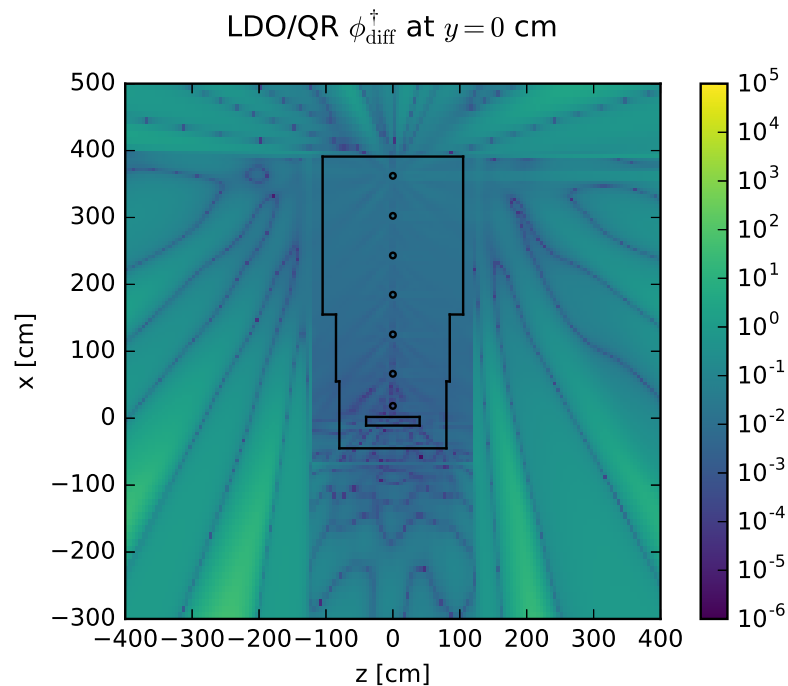


(c) LDFE adjoint flux slice.

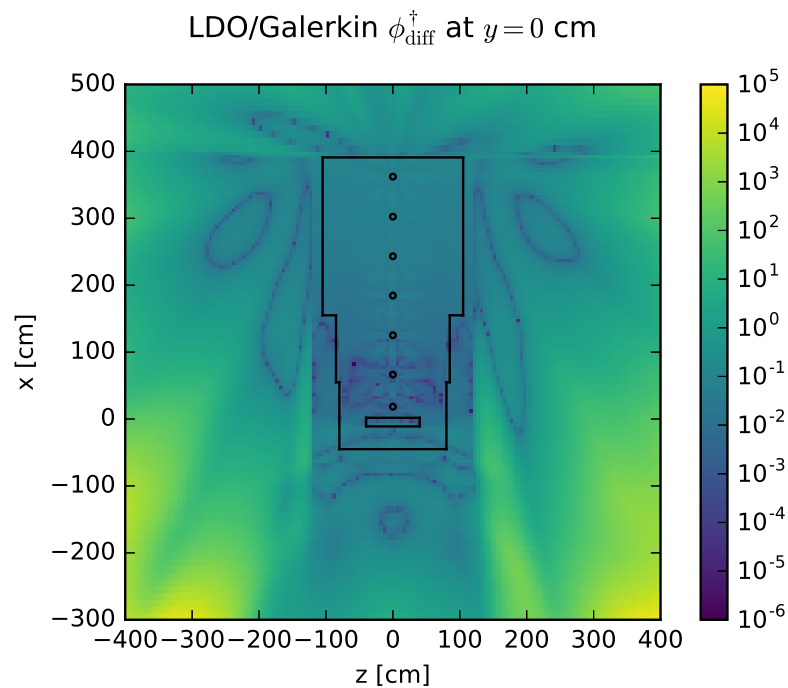


(d) LDO adjoint flux slice.

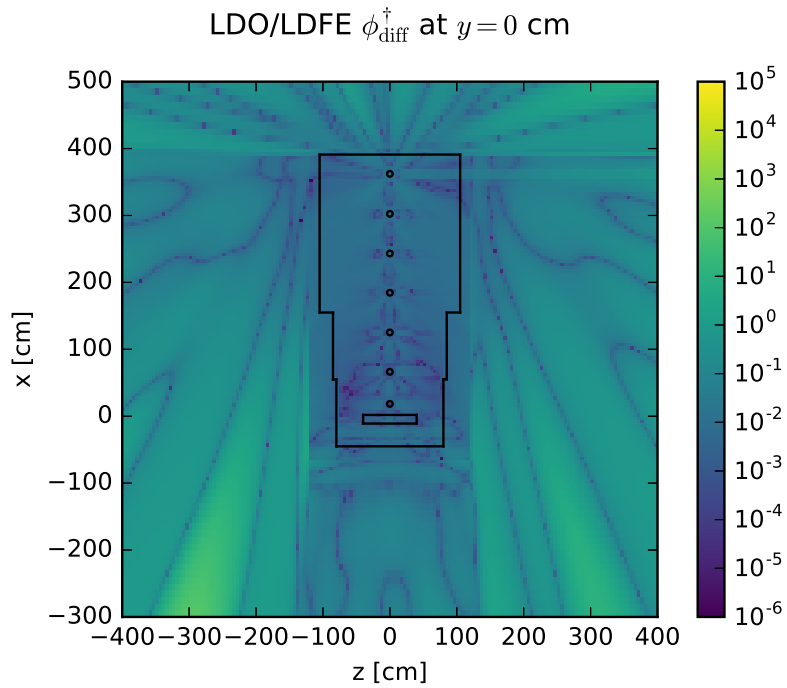
Figure 4.39: Ispra sodium benchmark adjoint scalar flux slices for the FW-CADIS method.



(a) LDO/QR flux relative difference.



(b) LDO/Galerkin flux relative difference.

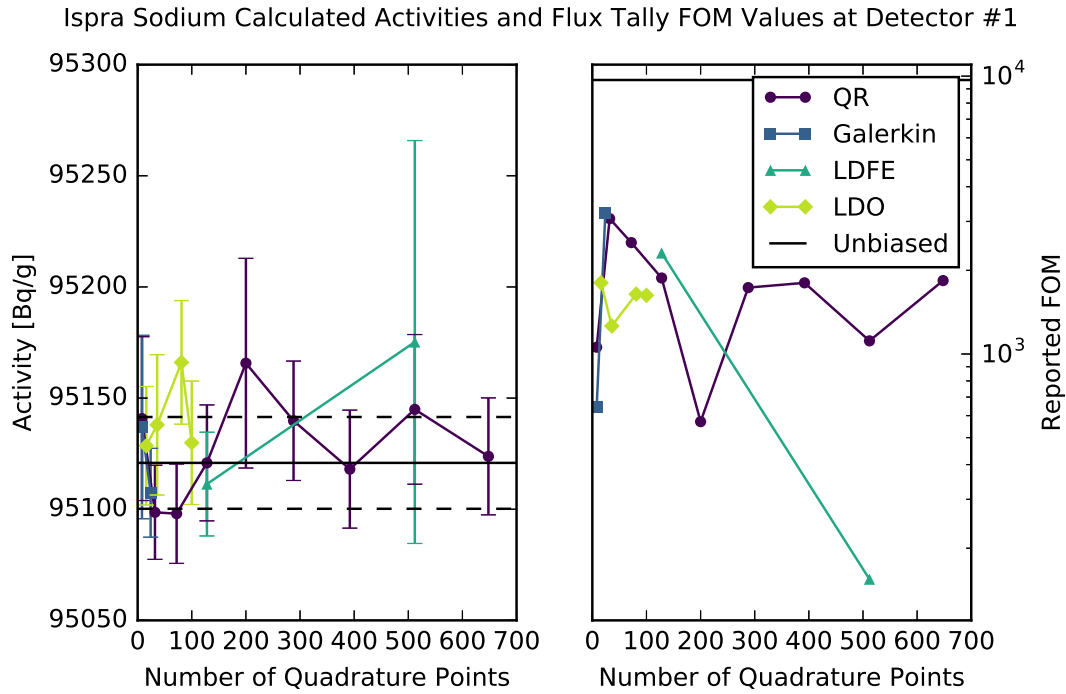


(c) LDO/LDFE flux relative difference.

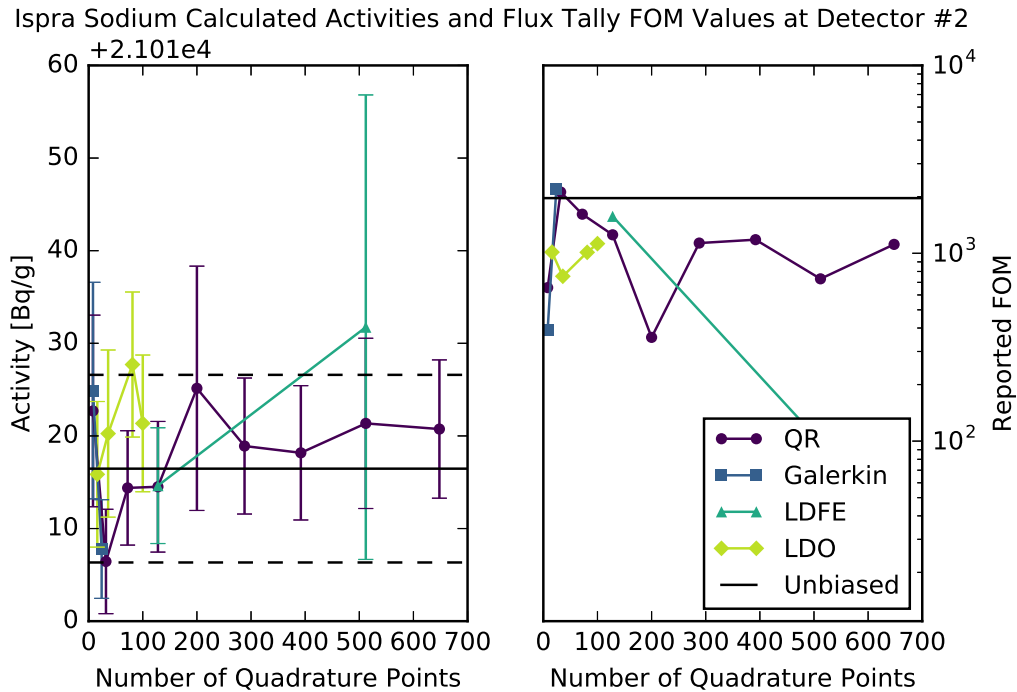
Figure 4.40: Ispra sodium adjoint scalar flux relative difference slices for the FW-CADIS method.

Having looked at the deterministically calculated adjoint flux solutions for the FW-CADIS method, we move on to examine the results of the Monte Carlo calculations run using the corresponding biasing parameters. All calculations here used 1×10^9 neutron histories. Figure 4.41 shows the saturation activities calculated for the various detector locations using Equation 4.2 and the parameters listed in Section 4.2.4. Figures of Merit for the forward flux tallies are also shown. The detectors are numbered such that detector #1 is the closest to the experimental neutron source location with increasing detector number as the distance between the neutron source and the detector location increases.

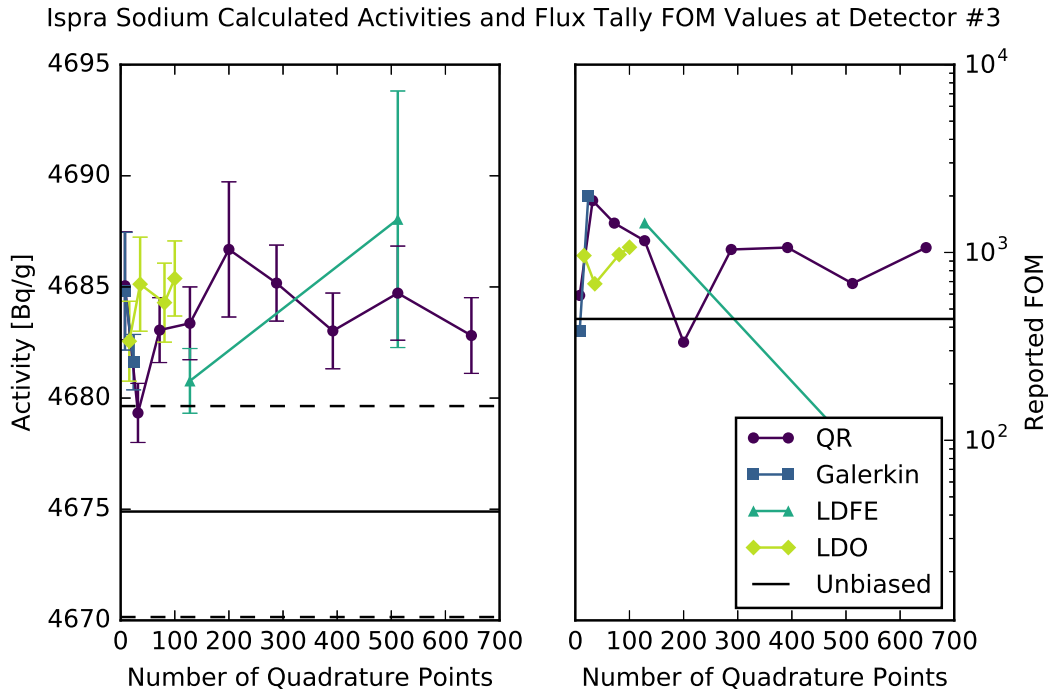
Comparing Figures 4.39 and 4.41, it is clear to see that the statistical uncertainty associated with the calculated activity (propagated from that of the forward flux tally) is heavily correlated to the adjoint source strength at the detector location. That is, detector #7, which has the highest adjoint source strength, sees the lowest uncertainty in the activity values calculated there. Even with the variation in statistical uncertainty, the behaviors of the FOM values for all detectors are fairly consistent between the locations for the biased calculations. For all detector locations, the biasing parameters from the coarser angular meshes produce higher FOM values than the mid-range and fine angular meshes for the quadrature types studied here.



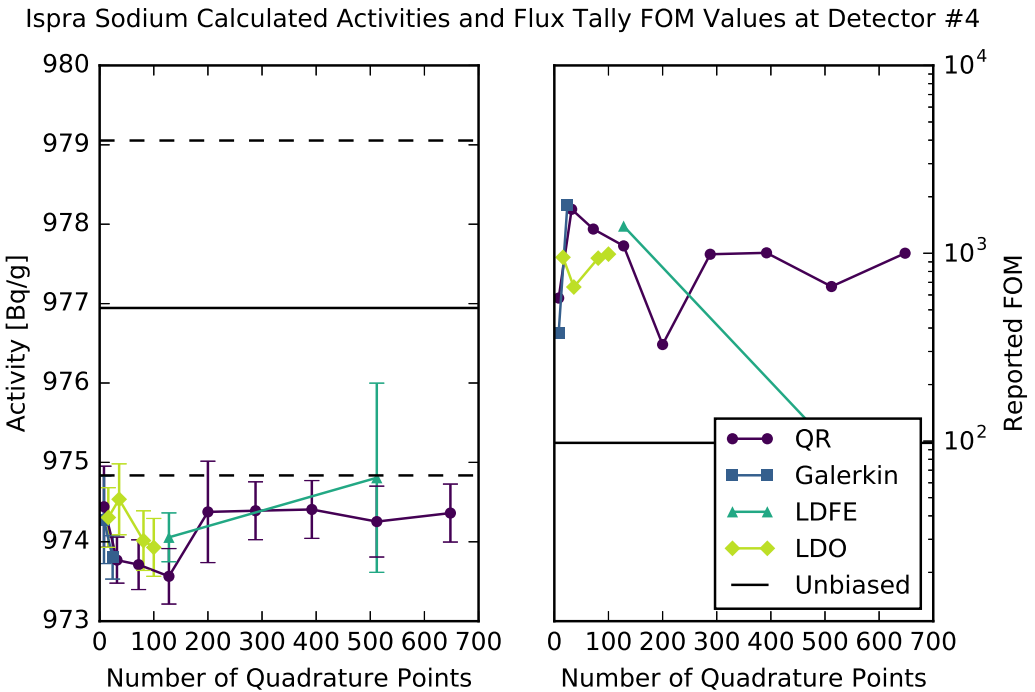
(a) Calculated activities and flux tally FOM values at detector #1.



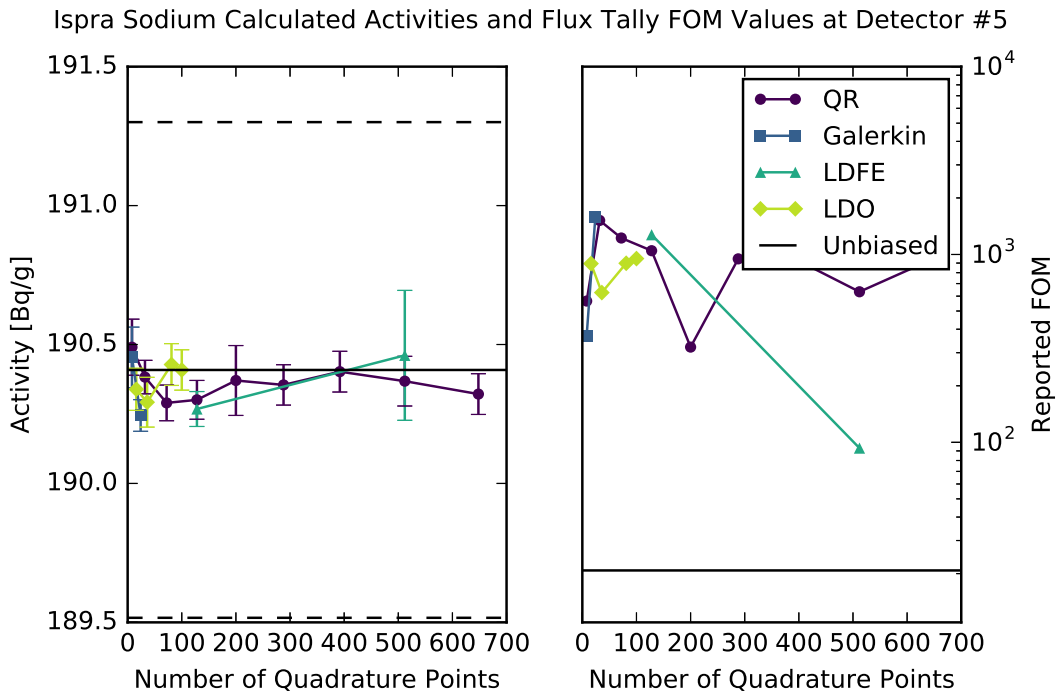
(b) Calculated activities and flux tally FOM values at detector #2.



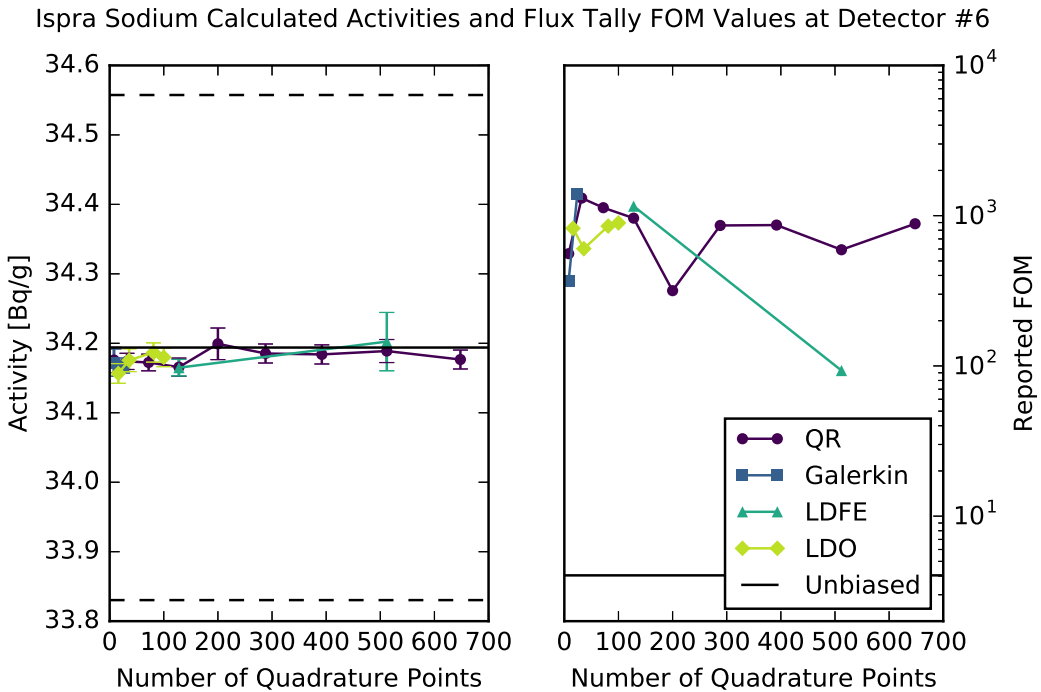
(c) Calculated activities and flux tally FOM values at detector #3.



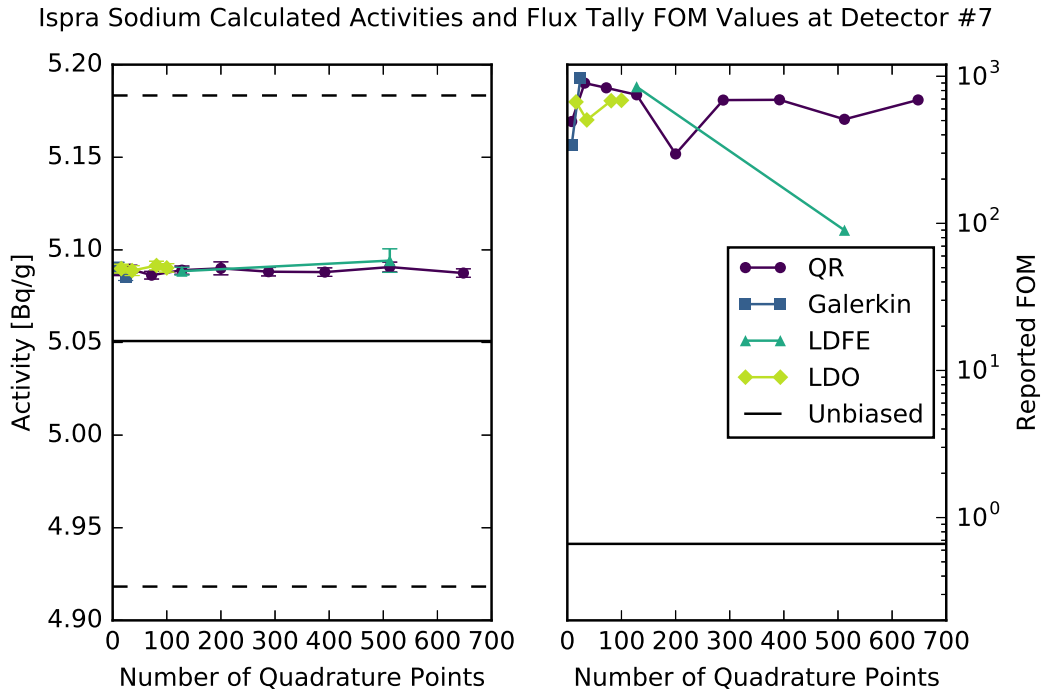
(d) Calculated activities and flux tally FOM values at detector #4.



(e) Calculated activities and flux tally FOM values at detector #5.



(f) Calculated activities and flux tally FOM values at detector #6.



(g) Calculated activities and flux tally FOM values at detector #7.

Figure 4.41: Ispra sodium benchmark FW-CADIS calculated activity and FOM values.

Table 4.20 lists the Figures of Merit for all detector locations for the representative quadrature sets. The FOM values from the unbiased Monte Carlo calculation are also included for reference. For all detector locations except that closest to the experimental neutron source, the representative Galerkin quadrature set generates biasing parameters that produce the highest FOM. The unbiased calculation results in the highest overall FOM for the detector closest to the neutron source, which is unsurprising given the relative proximity of the neutron source and closest detector and the relatively low adjoint source strength for that detector location in the FW-CADIS adjoint scalar flux solutions.

Table 4.20: Representative quadratures' FW-CADIS FOM values for the Ispra sodium test.

Quad. Type	Det. #1	Det. #2	Det. #3	Det. #4	Det. #5	Det. #6	Det. #7
QR	1877.6	1254.2	1155.3	1094.7	1047.4	962.76	748.32
Galerkin	3211.0	2205.2	1999.1	1797.5	1578.1	1398.1	969.99
LDFE	2309.4	1573.0	1436.7	1394.9	1273.9	1157.4	848.77
LDO	1626.0	1125.3	1066.2	989.45	950.75	895.03	686.34
Unbiased	9685.4	1966.4	442.76	97.875	20.791	4.0357	0.66237

Lastly, in Table 4.21, we compare the activities calculated from the biased and unbiased Monte Carlo forward flux tallies. At all detector locations, the calculations from the biased

and unbiased Monte Carlo runs severely overestimate the experimentally measured saturation activity (see Section 4.3.3), so we examine the Monte Carlo results amongst themselves. All of the calculations match within statistical uncertainty at detector locations 1, 2, 5, 6, and 7. At detector #4, the biased calculations match within their respective statistical errors but are all outside of the error bounds of the unbiased calculation. Detector #3 sees calculated activities all on the same order of magnitude; not all of the biased calculations match within statistical uncertainty and only the calculated activity using the LDFE biasing parameters matches the unbiased calculation within error bounds.

Table 4.21: Ispra sodium benchmark activities [Bq/g] calculated with FW-CADIS.

	QR	Galerkin	LDFE	LDO	Unbiased
Det. #1 ($\times 10^4$)	9.5121 ± 0.0026	9.5107 ± 0.0020	9.5111 ± 0.0023	9.5130 ± 0.0028	9.5121 ± 0.0021
Det. #2 ($\times 10^4$)	2.1024 ± 0.0007	2.1018 ± 0.0005	2.1024 ± 0.0006	2.1031 ± 0.0007	2.1026 ± 0.0010
Det. #3 ($\times 10^3$)	4.6834 ± 0.0016	4.6816 ± 0.0012	4.6808 ± 0.0015	4.6854 ± 0.0017	4.6749 ± 0.0047
Det. #4 ($\times 10^2$)	9.7356 ± 0.0035	9.7380 ± 0.0027	9.7406 ± 0.0031	9.7393 ± 0.0036	9.7695 ± 0.0211
Det. #5 ($\times 10^2$)	1.9030 ± 0.0007	1.9024 ± 0.0006	1.9027 ± 0.0006	1.9041 ± 0.0007	1.0941 ± 0.0089
Det. #6 ($\times 10^1$)	3.4166 ± 0.0013	3.4168 ± 0.0011	3.4165 ± 0.0012	3.4180 ± 0.0013	3.4194 ± 0.0363
Det. #7 ($\times 10^0$)	5.0891 ± 0.0022	5.0854 ± 0.0019	5.0885 ± 0.0021	5.0903 ± 0.0023	5.0508 ± 0.1326

To summarize the results in this section, we note that the detector activity calculations from the LDO biasing parameters are comparable within statistical uncertainty to those from the standard quadrature types, but the LDO biasing parameters do not generate the highest Figure of Merit for any detector location for the representative quadrature set. So, we would not suggest using an LDO quadrature set in the FW-CADIS method for a situation such as this scenario with fast reactor materials and detectors (adjoint source locations) all along one line. Of the LDO quadrature sets tested in this scenario, the coarsest and finest angular meshes produce comparable FOM values for all of the detector locations.

4.4.4 Simplified Portal Monitor

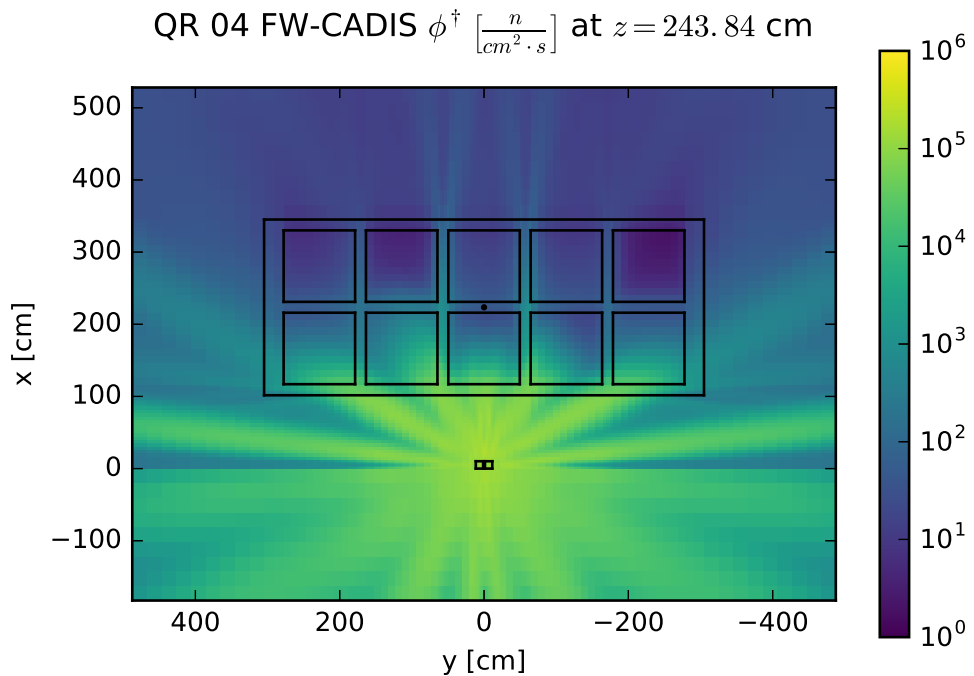
To generate Monte Carlo variance reduction parameters for the simplified portal monitor using the FW-CADIS method, the adjoint source was set to be all four detector locations in the problem's detector array. Figure 4.42 shows the adjoint scalar flux solutions from the representative quadrature sets for this case. Ray effects are seen in the $x - y$ plane for all quadrature sets; this is unsurprising given the relatively localized adjoint source with respect

to this plane. Differences between the representative LDO adjoint flux solution and the other adjoint flux solutions are shown in Figure 4.43 and listed in Table 4.22.

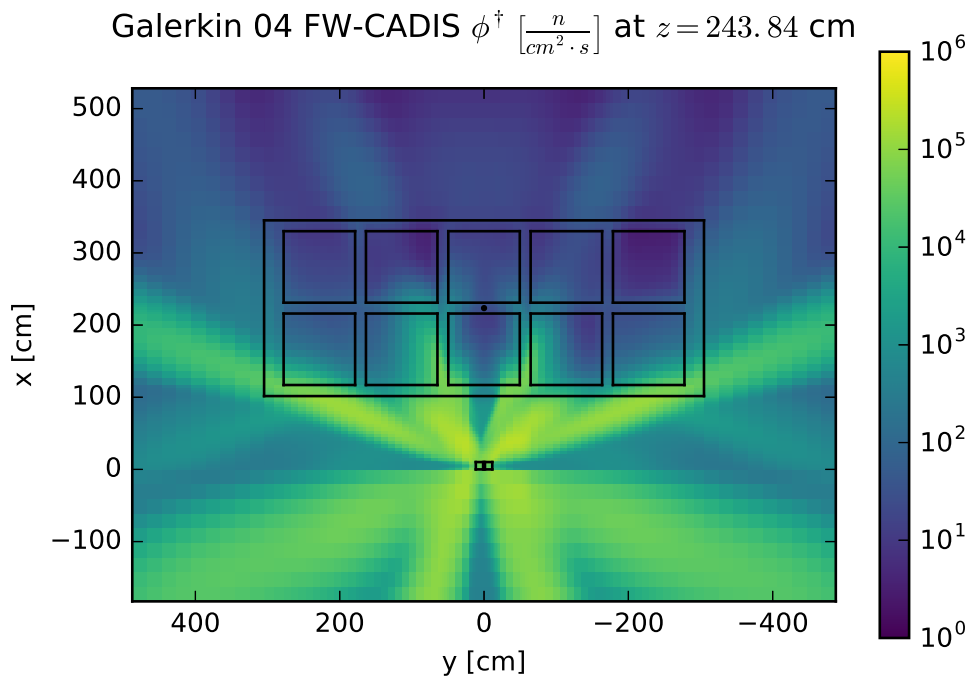
Table 4.22: Portal monitor FW-CADIS adjoint flux extremal and average relative differences.

Comparison	Min. Diff.	Max. Diff.	Avg. Diff.
LDO/QR	8×10^{-5}	8.59×10^1	2.95×10^0
LDO/Galerkin	3×10^{-4}	2.53×10^2	1.02×10^1
LDO/LDFE	3×10^{-5}	3.46×10^1	8.54×10^{-1}
Galerkin/QR	4×10^{-4}	1.19×10^2	3.23×10^0
LDFE/QR	1×10^{-4}	8.67×10^1	2.88×10^0

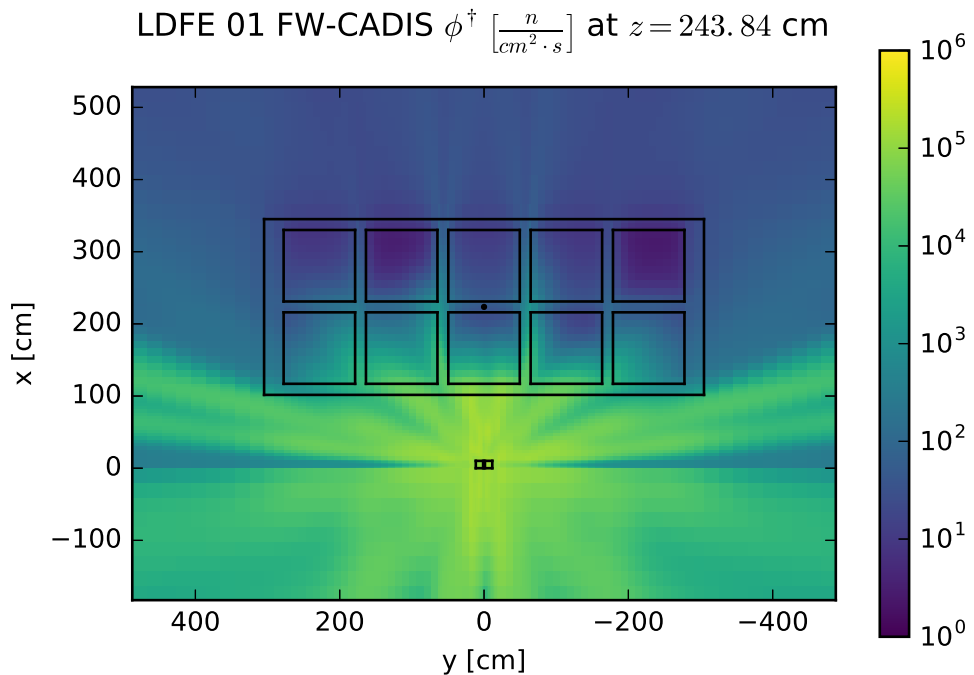
As with all other test cases, the listed differences are relative and comparisons between the standard representative quadrature sets are included for reference. Unlike other scenarios, the LDO adjoint flux best matches the LDFE adjoint flux for the simplified portal monitor scenario and this FW-CADIS adjoint source specification. However, this best agreement is an average relative difference of 85%; none of the flux solutions agree particularly well here. The relative difference flux plots show ray effects similar to those seen for the forward and CADIS adjoint scalar fluxes for all quadrature types in the simplified portal monitor scenario.



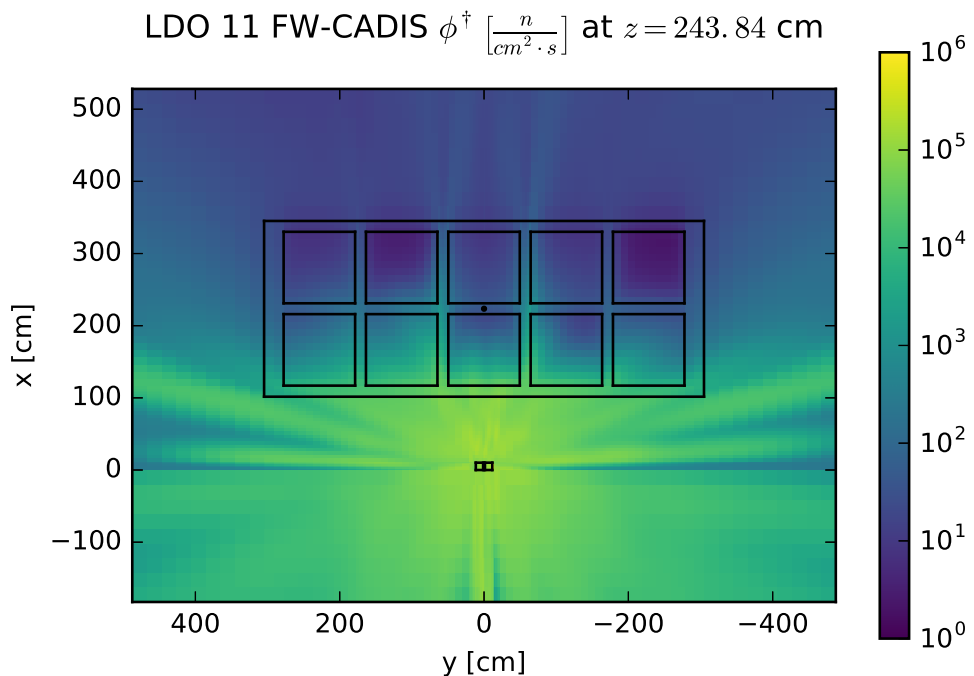
(a) QR adjoint flux slice.



(b) Galerkin adjoint flux slice.

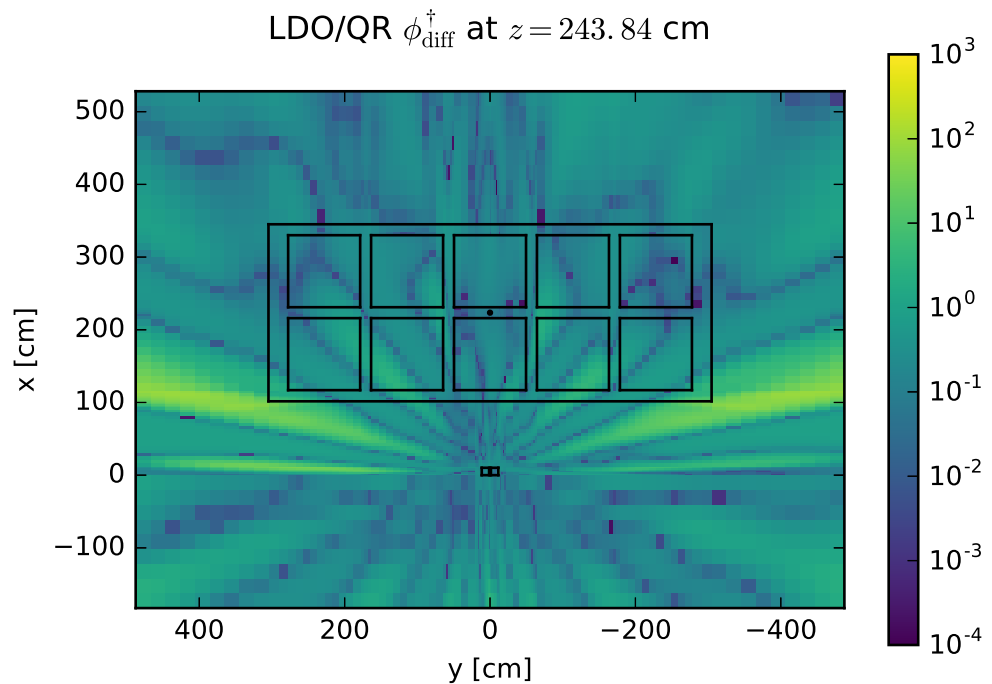


(c) LDDE adjoint flux slice.

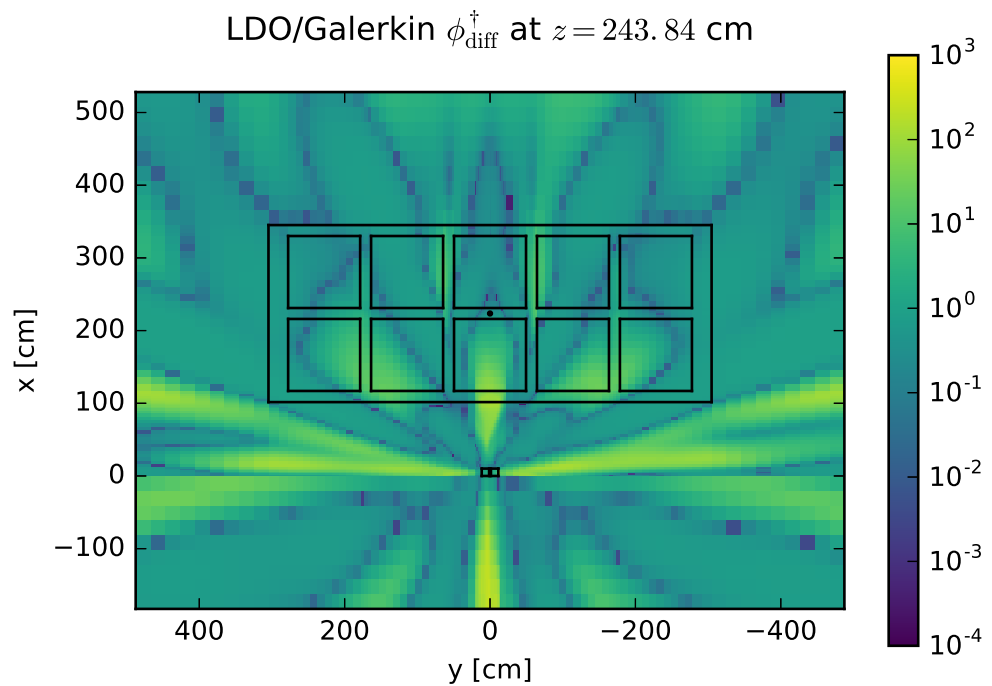


(d) LDO adjoint flux slice.

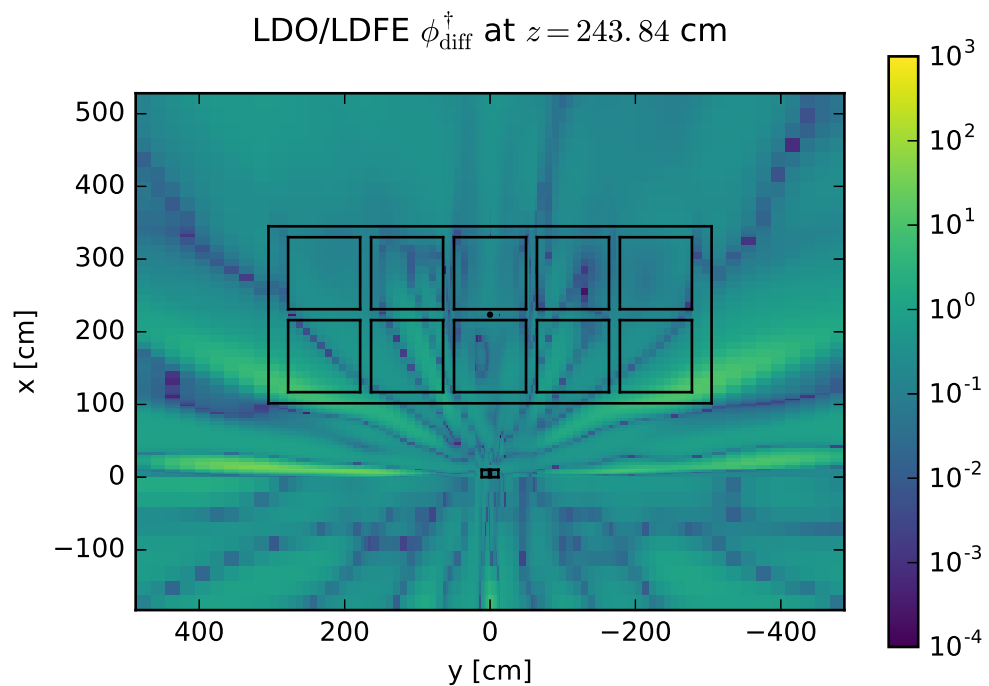
Figure 4.42: Simplified portal monitor adjoint flux slices for the FW-CADIS method.



(a) LDO/QR flux relative difference.



(b) LDO/Galerkin flux relative difference.



(c) LDO/LDFE flux relative difference.

Figure 4.43: Portal monitor adjoint flux relative difference slices for the FW-CADIS method.

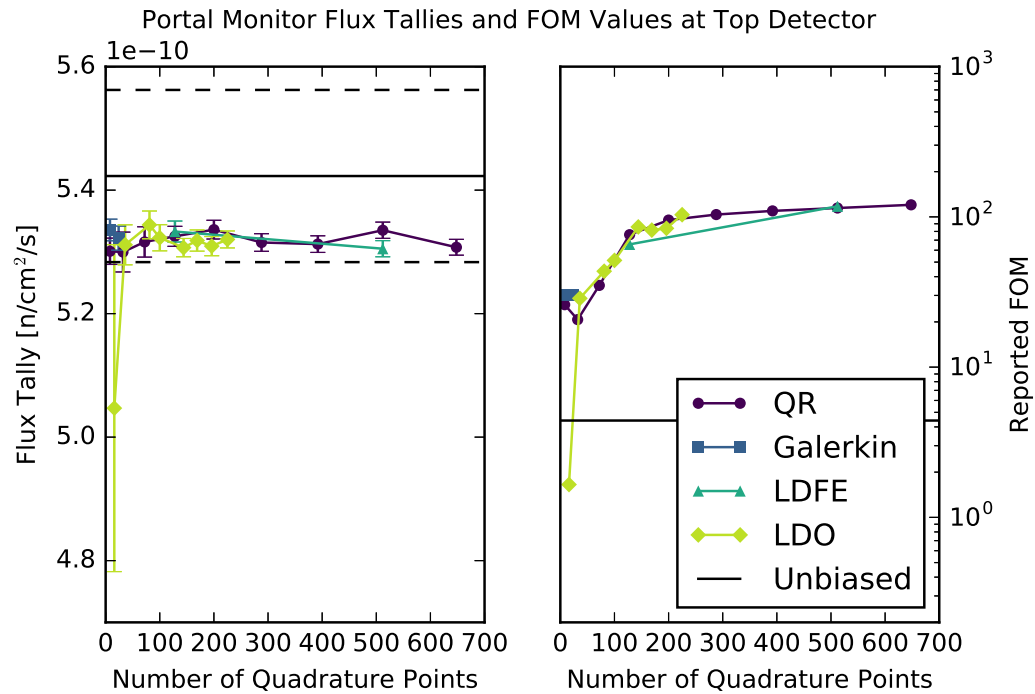
Figure 4.44 shows MCNP-reported forward scalar flux tallies and Figures of Merit for all four detectors in the array. The flux tallies and FOM values are each plotted as a function of the number of discrete angles used in the quadrature sets that were used to generate biasing parameters. In all plots, the unbiased calculation result is shown as a horizontal black line. At all detector locations, the forward flux tallies and FOM values show the same trend of leveling off to a stable value once the angular mesh used for the FW-CADIS biasing parameters has been refined past the few coarsest numbers of discrete angles. At all detector locations except for the 2nd in the array, the unbiased calculation and the calculations with biasing parameters resultant from the representative quadrature sets all match within statistical uncertainty. The 2nd detector sees all representative biased flux tallies matching one another but outside the error bounds of the unbiased flux tally calculation.

Table 4.23 lists the Figures of Merit for the various detector locations for the representative quadrature sets. The unbiased calculation FOM values are also tabulated for reference. We see that the biasing parameters from the representative LDO quadrature set produce the highest Figures of Merit for three out of four detector locations, with the representative QR quadrature set's biasing parameters achieving the highest FOM for the bottom detector in the array.

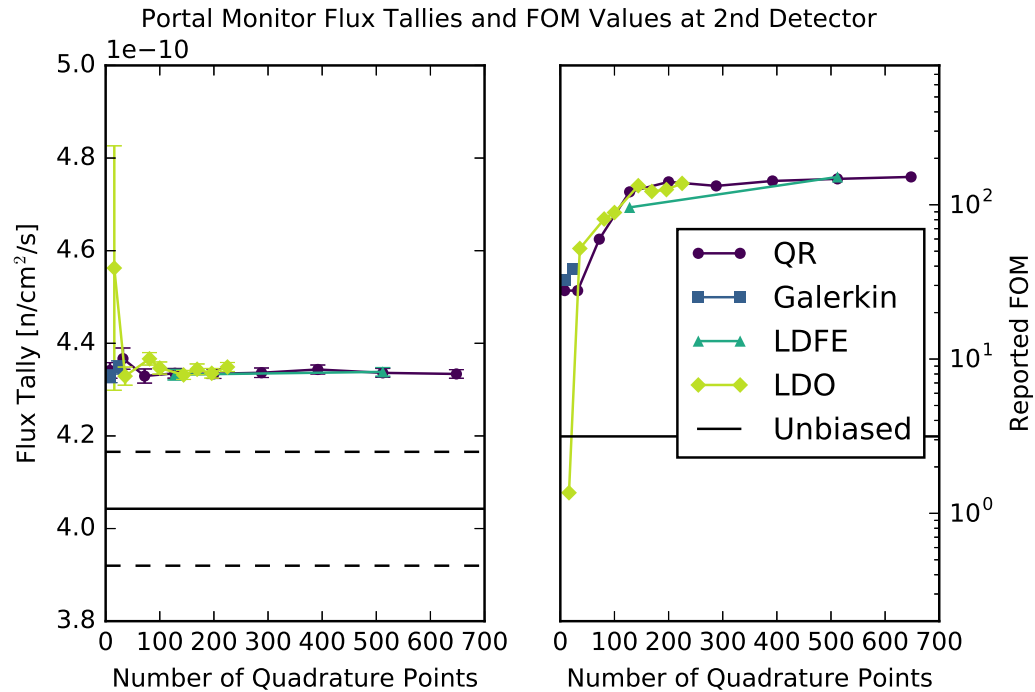
Table 4.23: FW-CADIS FOM values for representative quadratures for the portal monitor.

Quad. Type	Top Detector	2 nd Detector	3 rd Detector	Bottom Detector
QR	76.115	121.24	128.9	81.125
Galerkin	30.249	38.139	34.01	29.016
LDFE	65.613	96.156	115.5	61.655
LDO	85.707	132.96	140.3	75.135
Unbiased	4.4096	3.1520	2.096	2.8313

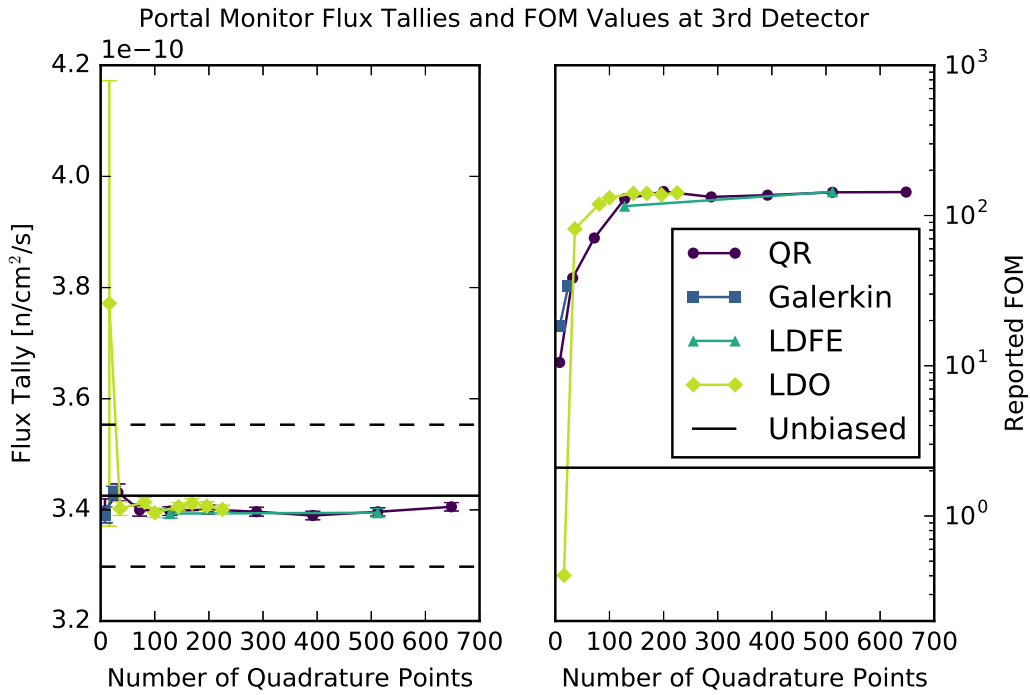
To conclude, using LDO quadrature sets to generate Monte Carlo biasing parameters in the FW-CADIS method is particularly promising for cases such as the simplified portal monitor scenario. When selecting an LDO quadrature set to generate variance reduction parameters for similar photon transport problems, a relatively coarse angular mesh of order 5 or 8 may be used to good effect.



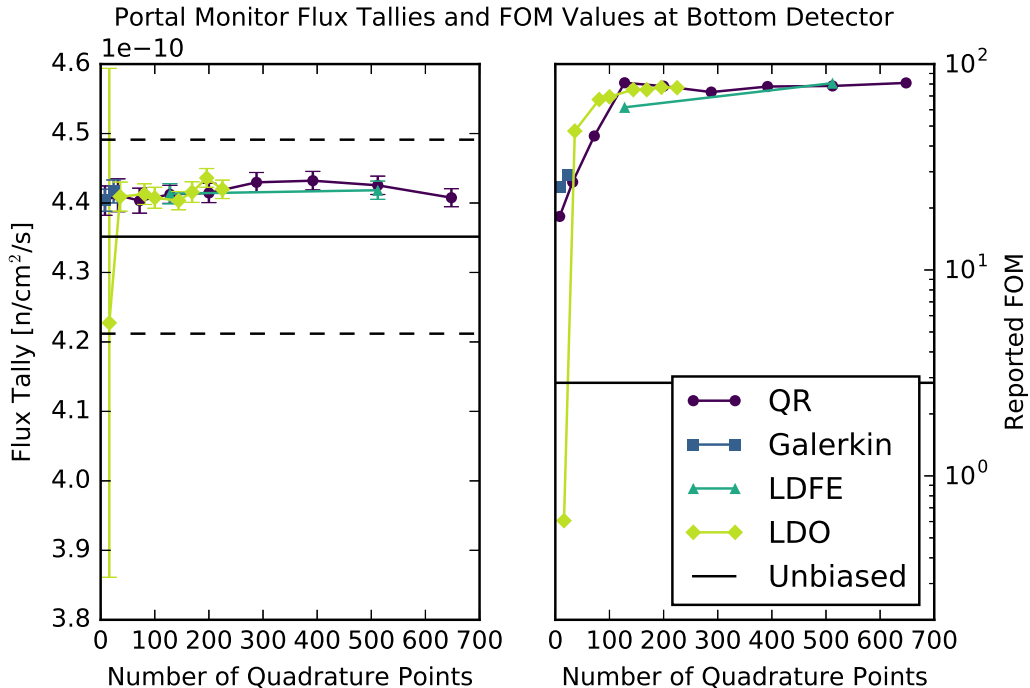
(a) MCNP-reported forward flux tally and FOM values at the top detector.



(b) MCNP-reported forward flux tally and FOM values at the second detector.



(c) MCNP-reported forward flux tally and FOM values at the third detector.



(d) MCNP-reported forward flux tally and FOM values at the bottom detector.

Figure 4.44: FW-CADIS flux tallies and FOM values for the portal monitor scenario.

4.4.5 Summary

We conclude the FW-CADIS method section by summarizing the results presented here. As in Section 4.3, the representative LDO adjoint scalar flux solutions were compared with those of representative standard quadrature types for each test case scenario. Compared to the CADIS calculations, the steel plate in water and DLVN experimental benchmark cases showed much more uniform relative differences for the adjoint scalar flux solutions in the context of the FW-CADIS method. Differences in the Ispra sodium benchmark and simplified portal monitor scenarios still appeared as ray effects due to the small scale of the FW-CADIS adjoint sources in the large problem geometries.

For the Monte Carlo results using the biasing parameters of the various quadrature sets from the FW-CADIS method, the forward flux tally results using the LDO biasing parameters were comparable to those of standard quadrature types across all of the test case scenarios. We generally recommend using a coarse LDO angular mesh of order 5 or 8 to generate biasing parameters for Monte Carlo neutral particle transport problems in the context of the FW-CADIS method. Highlights of the LDO quadratures' performance in this section include the representative LDO quadrature set producing the highest FOM values for two out of the six detector locations in the DLVN benchmark and three out of four detector locations in the simplified portal monitor scenario. To this end, further exploration of using LDO solutions for Monte Carlo variance reduction parameter generation for photon transport using the FW-CADIS method is an area of future work and interest.

4.5 Chapter Summary

Finally, we end the chapter with an overall summary of the results and discussion presented, with a specific focus on outcomes from LDO quadrature sets. Before exploring the LDO equations' solutions as input for Monte Carlo variance reduction parameter generation, we first performed comparative studies for the LDO equations' forward scalar flux solutions versus those of QR, Galerkin, and LDDE quadrature sets for four test case scenarios. Because QR quadrature sets are commonly used in Monte Carlo variance reduction parameter generation, particular attention was paid to the comparisons between the LDO and QR forward flux results. At best, the average relative difference between the representative LDO and QR forward flux solutions was 2.2% for the steel plate in water test case. The Ispra sodium benchmark case saw the greatest LDO/QR forward flux difference at an average of 50%. Based on this general agreement and all quadrature types capturing the same physical phenomena in each test case, we moved forward to explore the LDO equations' solutions in Monte Carlo variance reduction parameter generation.

Before looking at the results of the Monte Carlo calculations using biasing parameters from the CADIS method, the deterministic adjoint scalar flux solutions were explored for the different quadrature types. In this context, the LDO/QR adjoint flux solution comparison had the smallest relative difference (3.8%) for the DLVN experimental benchmark. The

responses of interest for the Monte Carlo calculations were studied as a function of angular mesh refinement used in the generation of biasing parameters. On the whole, little correlation was seen between angular mesh refinement and the MCNP-reported forward flux tally values in the CADIS context. If using an LDO quadrature set to generate biasing parameters in this context for any of the neutron transport scenarios, a low-order (3 - 8) quadrature set may be used to sufficient effect for flux tally value and FOM achievement. For generating biasing parameters in the CADIS context for a photon problem with an LDO quadrature set, the finest available angular mesh should be used. This is consistent with what is expected based on the difference between neutron and photon scattering in the materials in these test case scenarios.

Finally, studies of deterministic adjoint scalar flux solutions and their efficacy as input for Monte Carlo variance reduction parameter generation were performed in the context of the FW-CADIS method. Here the LDO adjoint flux solution best matched the QR adjoint flux solution in the steel plate scenario with an average relative difference of 4.6% between the representative quadrature sets' solutions. Again in this context we found that low-order (5 or 8) angular meshes are sufficient to produce forward flux tally and Figure of Merit values comparable to those of more refined angular meshes when using LDO quadrature sets. The superior FOM values resultant from the representative LDO quadrature set for three of four detectors in the simplified portal monitor scenario begets interest in further exploration of LDO equations' solutions as input for Monte Carlo biasing parameters for photon transport in the FW-CADIS context.

Bibliography

- [1] S.C. Wilson and R.N. Slaybaugh. “Improved Monte Carlo Variance Reduction for Space and Energy Self-Shielding”. In: *Nuclear Science and Engineering* 179.1 (2015), pp. 22–41. URL: <https://doi.org/10.13182/NSE13-109>.
- [2] Andrej Trkov. “Analysis of the Rowlands Uranium Oxide Pin-Cell Benchmark with an Updated WIMS-D Library”. In: *Annals of Nuclear Energy* 25.10 (1998), pp. 747–752.
- [3] Ronald J. McConn et al. *Compendium of Material Composition Data for Radiation Transport Modeling*. Tech. rep. PIET-43741-TM-963, PNNL-15870 Rev. 1. Pacific Northwest National Laboratory (PNNL), Richland, WA (US), 2011. URL: <https://doi.org/10.2172/1023125>.
- [4] R. N. Slaybaugh and S. C. Wilson. “Deterministic Parameter Study for Fixed-Source Calculations Using FW-CADIS”. In: *Trans. Am. Nucl. Soc* 108 (2013), p. 441.
- [5] Joshua J. Jarrell, Marvin L. Adams, and Joel M. Risner. “Application of Quadruple Range Quadratures to Three-Dimensional Model Shielding Problems”. In: *Nuclear Technology* 168.2 (2009), pp. 424–430.
- [6] Douglas Allen Barnett Jr. “Benchmark measurements and Calculations of a Three-Dimensional Neutron Streaming Experiment”. In: *International Topical Meeting on Advances in Mathematics, Computations, and Reactor Physics, Pittsburgh, PA, USA*. 1991.
- [7] I. Kodeli, E. Sartori, and B. Kirk. “SINBAD Shielding Benchmark Experiments Status and Planned Activities”. In: *The American Nuclear Society’s 14th Biennial Topical Meeting of the Radiation Protection and Shielding Division, Carlsbad, New Mexico, USA*. Citeseer. 2006.
- [8] S.W. Mosher et al. *ADVANTG – An Automated Variance Reduction Parameter Generator*. Tech. rep. ORNL/TM-2013/416, Rev. 1. Oak Ridge National Laboratory, Aug. 2015.
- [9] Advanced Micro Devices Inc. *AMD Opteron™ 6300 Series Processors*. <http://www.amd.com/en-us/products/server/opteron/6000/6300>. 2017.
- [10] Thomas M. Evans et al. “Denovo: A new three-dimensional parallel discrete ordinates code in SCALE”. In: *Nuclear Technology* 171.2 (2010), pp. 171–200. URL: <https://doi.org/10.13182/NT171-171>.

BIBLIOGRAPHY

- [11] Thomas Evans et al. *Exnihilo Documentation: Release 6.2.0 (Dev)*. Tech. rep. Oak Ridge National Laboratory, 2017.
- [12] Berkeley Research Computing. *System Overview*. <http://research-it.berkeley.edu/services/high-performance-computing/system-overview>. 2018.
- [13] X-5 Monte Carlo Team. *MCNP – A General Monte Carlo N-Particle Transport Code, Version 5*. Volume I: Overview and Theory. LA-UR-03-1987. Revised 2/1/2008. Los Alamos National Laboratory, Los Alamos, NM, Apr. 2003. URL: https://laws.lanl.gov/vhosts/mcnp.lanl.gov/pdf_files/la-ur-03-1987.pdf.
- [14] Joshua J. Jarrell and Marvin L. Adams. “Discrete-Ordinates Quadrature Sets Based on Linear Discontinuous Finite Elements”. In: *International Conference on Mathematics and Computational Methods Applied to Nuclear Science and Engineering (M&C 2011), Rio de Janeiro, RJ, Brazil*. 2011.
- [15] J. E. Morel. “A Hybrid Collocation-Galerkin-S_N Method for Solving the Boltzmann Transport Equation”. In: *Nuclear Science and Engineering* 101.1 (1989), pp. 72–87.
- [16] R. Nicks, G. Perlini, and H. Rief. “Fission Neutron Penetration in Iron and Sodium – I. Activation Measurements”. In: *Annals of Nuclear Energy* 15.9 (1988), pp. 457–469.
- [17] James J. Duderstadt and Louis J. Hamilton. *Nuclear Reactor Analysis*. New York, NY: John Wiley & Sons, Inc., 1976.
- [18] H. Depuydt and M. Neve de Mevergnies. “Average Cross Section of the $^{32}\text{S}(\text{n},\text{p})^{32}\text{P}$ and $^{27}\text{Al}(\text{n}, \alpha)^{24}\text{Na}$ Reactions for Fission Neutrons”. In: *Journal of Nuclear Energy. Parts A/B. Reactor Science and Technology* 16.9 (1962), pp. 447–453.
- [19] International Atomic Energy Agency. *Evaluated Nuclear Data File (ENDF)*. <https://www-nds.iaea.org/exfor/endf.htm>. 2018.